NTNU – Trondheim
Norwegian University of
Science and Technology

Scenario Development for Industrial Robot Manipulator: Case Study in Processing Casted Metal Components

Randi Anette Rønnestad
Fikkan

Master of Science in Engineering Cybernetics
Submission date: June 2013
Supervisor: Anton Shiriaev, ITK
Co-supervisor: Morten A. Langøy, BMS Steel AS

Norwegian University of Science and Technology
Department of Engineering Cybernetics

Problem Description

Project title: Scenario Development for Industrial Robot Manipulator: Case Study in Processing Casted Metal Components.

Summary: The project is aimed at developing scenarios of work of industrial robot manipulators ABB IRB 140, ABB IRB 1600 and ABB IRB 4600 for pick-and-place and processing operations of different complexities. At first, it includes the task of stable grasping and manipulation of the casted component of known geometry and stiffness. Then, it assumes the task of grasping and manipulation for the case when the CAD model could only approximately describe the geometry of the cast. At third level of complexity, the project requires steps for polishing or grinding the component for removing imperfections followed by inspection task. All the scenarios are expected to be validated on industrial robot manipulators in the Industrial Robotics Lab, and the experimental results will be analyzed for time, accuracy and repeatability. The work will be done in collaboration with BMS Steel AS.

Assignment given: 14. January 2013

Supervisor: Anton Shiriaev, ITK

Preface

This master's thesis presents the work done during the spring of 2013 as a part of my Master of Science degree at the department of Engineering Cybernetics at the Norwegian University of Science and Technology (NTNU). This thesis is a perpetuation of the specialization project I carried out during the fall of 2012. The focus of this thesis is to identify the parameters for the 6th joint of IRB 140, and then a passivity-based robust controller for the same joint was designed.

First and foremost I would like to thank my supervisor at the Department of Engineering Cybernetics, professor Anton Shiriaev, for his patience and collaboration. His knowledge has been invaluable.

I would also give a huge thanks to Anton Pyrkin, Sergey Kolyubin and Stepan Pchelkin for their help and cooperation. Their assistance has been of great importance to me.

Lastly I would like to thank my husband Kristoffer Fikkan and my kind friend Ragnhild Øvland for proof reading. Their thoughts and ideas have been appreciated.

Thank you for your confidence in me.

Randi Anette Fikkan

Trondheim, June 10, 2013

Samandrag

Hovudformålet med denne masteroppgava var å identifisere dei ukjende parametrane for det 6. leddet av robotmanipulatoren IRB 140, for deretter å lage ein passivitetsbasert robust kontrollar for å kontrollere dette leddet.

Denne rapporten inneheld ein kort introduksjon til modellering av robotmanipulatorar, systemidentifikasjon, digital signalbehandling og design av passivitetsbaserte robuste kontrollarar.

Ei simulering av minste kvadraters metode for systemidentifikasjonsmodellen vert presentert før den same metoden vert brukt for å estimere dei ukjende parametrane for IRB 140. Deretter vert ein passivitetsbasert robust kontrollar designa og testa for det 6. leddet av IRB 140.

I dei eksperimentelle resultata vart det oppdaga at dei estimerte parametrane var feil. Det vart òg oppdaga at estimata for dei ukjente parametrane har stor innverknad på den passivitetsbaserte robuste kontrollaren. Dersom estimata er feil vert nøyaktigheita for kontrollaren dårleg. Det vart oppdaga at dette gjer at den designa kontrollaren er mindre presis enn ABB sin kontrollar i RobotStudio.

For plukk- og plasséroppgåver med støypte komponentar og anna tilverking av slike komponentar er det viktig å ha kraft- og hastigheitsavgrensing for roboten, slik at den ikkje knuser komponentane eller misser taket på dei.

Summary

The main objective of this master's thesis was to identify the unknown parameters for the 6th joint of robot manipulator IRB 140 and then create a passivity-based robust controller for controlling this joint.

This report includes a brief introduction to modeling of robot manipulators, system identification, digital signal processing and passivity-based robust controllers.

A simulation of the least squares method for the system identification model is presented before the same method is used to estimate the unknown parameters for IRB 140. Then a passivity-based robust controller is designed and tested for the 6th joint of IRB 140.

From the experimental results it was discovered that the estimated parameters were incorrect. It was revealed that the estimates of the unknown parameters have great influence on the passivity-based robust controller. If the estimates are incorrect the accuracy of controller is poor. The controller designed in this thesis was less precise than the ABB RobotStudio controller.

To pick-and-place and process casted components it is important to have force and velocity limitations for the robot, so that it does not crush the components or lose hold of them.

Contents

List of Figures

List of Tables

List of Abbreviations

CAD	Computer Aided Design
DFT	Discrete Fourier Transform
DH Convention	Denavit-Hartenberg Convention
DOF	Degrees of Freedom
FFT	Fast Fourier Transform
IRB	Industrial RoBot, used in names for ABB robots
LS	Least Squares
PE	Persistent Excitation
RIA	Robot Institute of America
TCP	Tool Center Point

Chapter 1

Introduction

1.1 Motivation

In 1920 Karel Čapek, a Czech playwright, was the first to introduce the term *robot* in his play *Rossum's Universal Robots*. The English term *robot* comes from the Czech word for work, which is *robota*. After this the term *robot* has been applied for many different mechanical devices with some sort of autonomy to be controlled by a computer [10]. In this master thesis the robot manipulator concerned is ABB's IRB 140, an industrial robot manipulator with 6 revolute joints.

The term *robot* which reflects todays use of robot technology is defined by the Robot Institute of America (RIA) as

"*A robot is a reprogrammable, multifunctional manipulator designed to move material, parts, tools, or specialized devices through variable programmed motions for the performance of a variety of tasks*" [10, p. 2].

This definition correspond well with the common understanding that commercial and industrial robots can be employed for jobs which are too tiresome or dangerous to be suitable for humans. E.g. robots working with manufacturing in combination with a conveyor belt; palletizing, assembling or pick-and-place operations.

Today the field of robotics is "seen as part of the field of mechatronics, which is defined as the synergistic integration of mechanics, electronics, controls and computer science" [10, p. iv]. The development of the robotics is therefore included in a field which strive to develop more efficient and cost effective tools.

1.2 The Problem

In this master thesis the parameters for the 6th joint of IRB 140 is to be identified and a passivity-based robust controller is to be developed for the same joint. The controller is then to be tested and analyzed. From the specialization project "*Using ABB MultiMove Functionality for Cooperative Manipulation Tasks*" [6] by Fikkan it was discovered that the offline programming with ABB RobotStudio was difficult since the reference for the robot changed from offline state to online state. Therefore it is valuable to identify the unknown parameters so that a controller which is easier to design trajectories for can be created.

1.3 Outline

Chapter 2 begins with an introduction to the Euler-Lagrange dynamic model for robot manipulators, followed by a short part on system identification using the Least Squares (LS) estimation method, and the statistical properties of this method. Then the measurement filtering and Fast Fourier Transform (FFT) are explained. In the end the passivity-based robust controller is introduced.

In Chapter 3 a simulation of the LS method is presented, where the unknown parameters for the 6th joint of IRB 140 are estimated. Then three different measurements are used to estimate the same parameters. To achieve better results when estimating these parameters, high frequency noise is removed from the measurements with low pass filters. First all of the filtered measurements are used for system identification, then a subset of the filtered measurements are used. Subsequently the estimated parameters are used in simulations to check whether or not it is possible to achieve the same results as the measurements given by Stepan Pchelkin. In the end the best results for the different estimation experiments are presented.

Next the passivity-based robust controller for the 6th joint of IRB 140 is presented in Chapter 4. The experimental results for the controller are then introduced and analyzed.

In the end the conclusions and possible further work are presented in Chapter 5.

In Appendix A it is described where to find the attached files including the Maple and MATLAB code.

Chapter 2

Preliminaries

There are many interesting technical and scientific subjects in the discipline of robotics. Sensor and vision technologies, real time systems, nonlinear and linear system theories, man-machine interaction, system identification and computer languages are some of the many topics one can come across when working with robotics. This chapter gives a brief introduction to the parts of robotics relevant for this master thesis, i.e. modeling of robot manipulators, system identification, digital signal processing and passivity-based robust controllers. This thesis will only give a brief introduction to these topics; for a deeper and more thorough description see "*Robust Adaptive Control*" [8] by Ioannou and Sun, "*System Identification; Theory for the User*" [9] by Ljung, "*Robot Modeling and Control*" [10] by Spong et al., "*Digital Signal Processing*" [12] by Proakis and Manolakis and "*System Identification*" [13] by Söderström and Stoica.

2.1 The Robot Manipulator

Models of robot manipulators are usually expressed in joint angles $\boldsymbol{q}$ and their derivatives $\dot{\boldsymbol{q}}$, $\ddot{\boldsymbol{q}}$, where $\boldsymbol{q} \in \mathbb{R}^n$. The matrix representation for the Euler-Lagrange equations for motions is given as

$$\mathbf{M}(\boldsymbol{q})\ddot{\boldsymbol{q}} + \mathbf{C}(\boldsymbol{q}, \dot{\boldsymbol{q}})\dot{\boldsymbol{q}} + \boldsymbol{g}(\boldsymbol{q}) = \boldsymbol{\tau} \tag{2.1}$$

For an n link manipulator $\mathbf{M}(\boldsymbol{q}) \in \mathbb{R}^{n \times n}$ is the inertia matrix, which is symmetrical and positive definite,

$\mathbf{C}(\boldsymbol{q}, \dot{\boldsymbol{q}}) \in \mathbb{R}^{n \times n}$ is the matrix representing centrifugal, Coriolis and friction forces, $\boldsymbol{g}(\boldsymbol{q}) \in \mathbb{R}^n$ is the gravity force vector and $\boldsymbol{\tau} \in \mathbb{R}^n$ is the joint torque vector.

The calculation of the Euler-Lagrange equations include the Jacobian, $\mathbf{J} \in \mathbb{R}^{m \times n}$, which depends on the calculation of the forward kinematics for the robot. To derive the forward kinematics for a robot the Denavit-Hartenberg Convention (DH Convention) is a useful methodology.

2.2 Denavit-Hartenberg Convention

This representation of robot manipulators will be restricted to the "most common type of industrial robot which is the six-axes articulated robot of elbow type" [11, p. 13]. For the articulated robot of elbow type there are no prismatic joints present, hence the parameter q_i for each joint i represent a variable angle given in radians. The joints of the robot manipulator are assumed to be of one degree of freedom (DOF). To get the correct degree of freedom for the spherical wrist this is usually modeled as three joints with zero distance, where each of these three joint is of one DOF.

For an n-DOF robot manipulator the base frame is found at link 0, indicated by the coordinate system $x_0y_0z_0$. The tool frame is found at the nth link and the coordinate system $x_ny_nz_n$ indicate its orientation. A general rule is that joint i is found between link $i-1$ and link i. This implies that the first joint combines link 0, the base frame, with link 1. To find and identify coordinate system 0 to n, the two rules for the DH Convention can be used.

The two rules introduced in "*Robot Modeling and Control*" [10] by Spong are:

- "(DH1) The axis x_1 is perpendicular to the axis z_0" [10, p. 78].
- "(DH2) The axis x_1 intersects the axis z_0" [10, p. 78].

When the coordinate systems are identified, one have to determine the four variables a_i, α_i, d_i and θ_i for each link i of the robot manipulator. The link length is given by a_i, the link twist by α_i, the link offset by d_i and the joint angle by θ_i [10]. For robots only consisting of revolute joints the variables d, α and a are constant, while the fourth variable θ is the joint variable. This is indicated with the variable name $q_i, i = 1, \ldots, n$ and an asterisk. These parameters are often presented in a DH parameter table.

From the parameters in the DH table one can calculate the homogeneous transformation matrices $\mathbf{A}_i^{i-1}$. This can be seen in Equation (2.2). Here $\cos\phi_i$ is written as c_{ϕ_i} and $\sin\phi_i$ is written as s_{ϕ_i}. After this calculation the matrix $\mathbf{A}_i^{i-1}$ will take the form shown in Equation (2.3). The combined homogeneous transformation matrices $\mathbf{T}_i^0$ for the different links can be calculated using the different matrices $\mathbf{A}_i^{i-1} \in i = 1, 2, \ldots, n$ by multiplying them as shown in Equation (2.4). See Equation (2.5) to identify where the different vectors $\boldsymbol{x}_i^0$, $\boldsymbol{y}_i^0$, $\boldsymbol{z}_i^0$ and $\boldsymbol{o}_i^0$ can be found in $\mathbf{T}_i^0$.

In Figure 2.1 the different parameters and coordinate axes for a 6 DOF articulated elbow manipulator can be found. For IRB 140 and IRB 1600 the DH parameters can be found in Table 2.1, where the known d and a parameters, found in *Product Specification, Articulated robot IRB 140* [1] and *Product Specification, Articulated robot IRB 1600* [2], can be seen in Tables 2.2 and 2.3. The kinematic model and the DH parameters presented in Figure 2.1 and Tables 2.1 - 2.3 were obtained from Stepan Pchelkin.

$$\mathbf{A}_i^{i-1} = \mathbf{Rot}_{z,\theta_i}\mathbf{Trans}_{z,d_i}\mathbf{Trans}_{x,a_i}\mathbf{Rot}_{x,\alpha_i} \tag{2.2}$$

$$= \begin{bmatrix} c_{\theta_i} & -s_{\theta_i} & 0 & 0 \\ s_{\theta_i} & c_{\theta_i} & 0 & 0 \\ 0 & 0 & 1 & 0 \\ 0 & 0 & 0 & 1 \end{bmatrix} \begin{bmatrix} 1 & 0 & 0 & 0 \\ 0 & 1 & 0 & 0 \\ 0 & 0 & 1 & d_i \\ 0 & 0 & 0 & 1 \end{bmatrix}$$

$$\times \begin{bmatrix} 1 & 0 & 0 & a_i \\ 0 & 1 & 0 & 0 \\ 0 & 0 & 1 & 0 \\ 0 & 0 & 0 & 1 \end{bmatrix} \begin{bmatrix} 1 & 0 & 0 & 0 \\ 0 & c_{\alpha_i} & -s_{\alpha_i} & 0 \\ 0 & s_{\alpha_i} & c_{\alpha_i} & 0 \\ 0 & 0 & 0 & 1 \end{bmatrix}$$

$$\mathbf{A}_i^{i-1} = \begin{bmatrix} \mathbf{R}_i^{i-1} & \boldsymbol{o}_i^{i-1} \\ \mathbf{0} & 1 \end{bmatrix} \tag{2.3}$$

$$\mathbf{T}_i^0 = \mathbf{A}_1^0 \cdot \quad \cdot \quad \cdot \mathbf{A}_i^{i-1} \tag{2.4}$$

$$\mathbf{T}_i^0 = \begin{bmatrix} \mathbf{R}_i^0 & \boldsymbol{o}_i^0 \\ \mathbf{0} & 1 \end{bmatrix} = \begin{bmatrix} \boldsymbol{x}_i^0 & \boldsymbol{y}_i^0 & \boldsymbol{z}_i^0 & \boldsymbol{o}_i^0 \\ 0 & 0 & 0 & 1 \end{bmatrix} \tag{2.5}$$

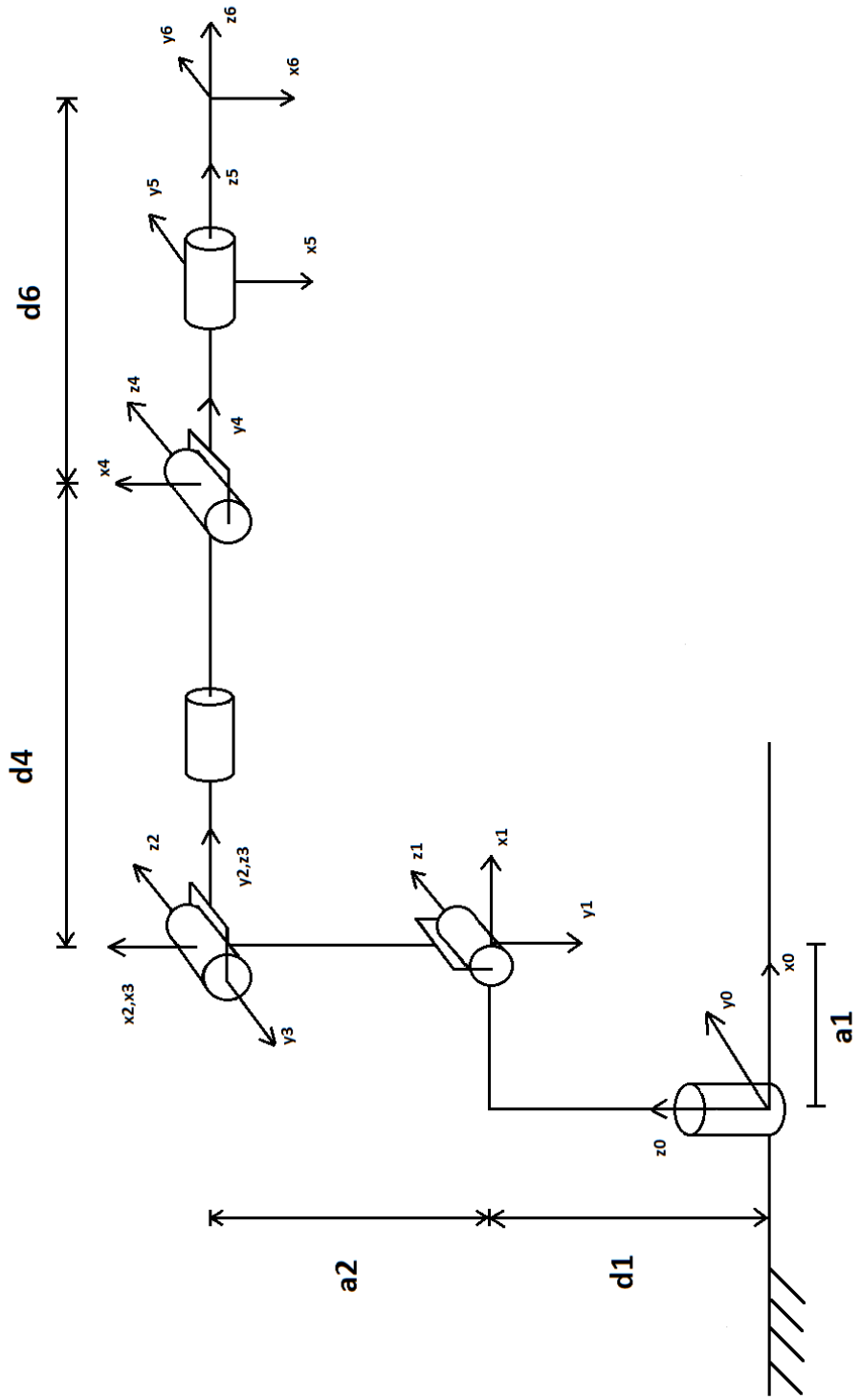

Figure 2.1: Kinematic structure of an articulated robot of elbow type.

	θ	d	a	α
1	q_1^*	d_1	a_1	$-\frac{\pi}{2}$
2	$q_2^* - \frac{\pi}{2}$	0	a_2	0
3	q_3^*	0	0	$-\frac{\pi}{2}$
4	q_4^*	d_4	0	$\frac{\pi}{2}$
5	$q_5^* + \pi$	0	0	$\frac{\pi}{2}$
6	q_6^*	d_6	0	0

Table 2.1: DH parameters for IRB 140 and IRB 1600.

Table 2.2: Known parameters for IRB 140.

$d_1 = 0.352$ m
$d_2 = 0.380$ m
$d_3 = 0.065$ m
$a_1 = 0.070$ m
$a_2 = 0.360$ m

Table 2.3: Known parameters for IRB 1600.

$d_1 = 0.4865$ m
$d_2 = 0.600$ m
$d_3 = 0.065$ m
$a_1 = 0.150$ m
$a_2 = 0.475$ m

2.3 Jacobian

After deriving the forward kinematics for a robot the next step would be to derive the velocity relationship of the end effector[1] and the joint velocities. "Mathematically, the forward kinematic equations define a function between the space of Cartesian positions and orientations and the space of joint positions. The velocity relationships are then determined by the Jacobian of this function" [10, p. 119]. It is also said that "[t]he Jacobian is a matrix that generalizes the notion of the Jacobian of the ordinary derivative of a scalar function" [10, p. 119].

For each joint i in a manipulator there exists a Jacobian matrix. When calculating the Jacobian for the nth joint one get the Jacobian for the end effector. The size of the Jacobian matrix is $6 \times n$; each joint has its own vertical vector with 3 elements for the linear velocities, and 3 elements for the angular velocities.

The notation $\boldsymbol{J}_{v_i}$ indicates the vector elements inside the Jacobian matrix. The subscript in the notation $\mathbf{J}_i^0$ and the sub subscript in the notations $\mathbf{J}_{v_i}^0$ and $\mathbf{J}_{\omega_i}^0$ indicate which joint the Jacobian are calculated for, in this case i. For a manipulator with n links the angular velocity for the end effector is given by $\boldsymbol{\omega}_n^0$ and the linear velocity is given by $\boldsymbol{v}_n^0 = \dot{\boldsymbol{o}}_n^0$. The n link manipulator has joint variables $q_1, ..., q_n$ stacked in a vector $\boldsymbol{q}$. The relation between joint velocity and end effector velocity is given by

$$\boldsymbol{v}_n^0 = \mathbf{J}_{v_n}^0 \dot{\boldsymbol{q}} \tag{2.6}$$
$$\boldsymbol{\omega}_n^0 = \mathbf{J}_{\omega_n}^0 \dot{\boldsymbol{q}} \tag{2.7}$$

The Jacobian is given by $\mathbf{J}_{v_n}^0$ and $\mathbf{J}_{\omega_n}^0$ placed on top of each other. Then the Jacobian becomes

$$\mathbf{J}_n^0 = \begin{bmatrix} \mathbf{J}_{v_n}^0 \\ \mathbf{J}_{\omega_n}^0 \end{bmatrix} \tag{2.8}$$

where

$$\mathbf{J}_{v_n}^0 = [\boldsymbol{J}_{v_1} \cdots \boldsymbol{J}_{v_n}] \tag{2.9}$$
$$\mathbf{J}_{\omega_n}^0 = [\boldsymbol{J}_{\omega_1} \cdots \boldsymbol{J}_{\omega_n}] \tag{2.10}$$

[1] An end effector is a tool attached to the end of a robotic arm, e.g. a gripper.

For revolute joints the calculation of each column i in Equation (2.9) is

$$\boldsymbol{J}_{v_i} = \boldsymbol{z}_{i-1} \times (\boldsymbol{o}_n - \boldsymbol{o}_{i-1}) \tag{2.11}$$

and the calculation for revolute joints of each column i in Equation (2.10) is

$$\boldsymbol{J}_{\omega_i} = \boldsymbol{z}_{i-1} \tag{2.12}$$

where the vectors $\boldsymbol{z}_{i-1}$ and $\boldsymbol{o}_{i-1}$ are found in the $\mathbf{T}_{i-1}^0$ matrices and the vector $\boldsymbol{o}_n$ is found in the $\mathbf{T}_n^0$ matrix, calculated for the forward kinematics using the DH-convention. See Equation (2.5) to identify where the different vectors can be found in $\mathbf{T}_{i-1}^0$ and $\mathbf{T}_n^0$.

2.4 Euler-Lagrange

By using Newton's second law for a one DOF system the Lagrangian can be found as the difference between the kinetic and potential energy [10]. The Lagrangian is given as

$$\mathcal{L} = \mathcal{K} - \mathcal{P} \tag{2.13}$$

where the kinetic energy for a rigid body is given as

$$\mathcal{K} = \frac{1}{2} m \boldsymbol{v}^\mathsf{T} \boldsymbol{v} + \frac{1}{2} \boldsymbol{\omega}^\mathsf{T} \mathcal{I} \boldsymbol{\omega} \tag{2.14}$$

and the potential energy for a rigid body is given as

$$\mathcal{P} = m \boldsymbol{g}^\mathsf{T} \boldsymbol{r}_c \tag{2.15}$$

where $\mathcal{I}$ is the inertia tensor relative the inertial frame given as

$$\mathcal{I} = \mathbf{R}\mathbf{I}\mathbf{R}^\mathsf{T} \tag{2.16}$$

where $\mathbf{I}$ is the inertia tensor expressed in the body attached frame [10].

$\mathbf{I}$ is a 3×3 matrix with the principal moments of inertia about x-, y- and z-axis placed on the diagonal and the cross products of inertia place on the off-diagonal. This is depicted in Equation (2.17)

$$\mathbf{I} = \begin{bmatrix} I_{xx} & I_{xy} & I_{xz} \\ I_{yx} & I_{yy} & I_{yz} \\ I_{zx} & I_{zy} & I_{zz} \end{bmatrix} \tag{2.17}$$

where the principal moments of inertia are

$$I_{xx} = \int\int\int (y^2 + z^2)\rho(x, y, z)\ dx\ dy\ dz \tag{2.18}$$

$$I_{yy} = \int\int\int (x^2 + z^2)\rho(x, y, z)\ dx\ dy\ dz \tag{2.19}$$

$$I_{zz} = \int\int\int (x^2 + y^2)\rho(x, y, z)\ dx\ dy\ dz \tag{2.20}$$

and the cross products of inertia are

$$I_{xy} = I_{yx} = -\int\int\int xy\rho(x, y, z)\ dx\ dy\ dz \tag{2.21}$$

$$I_{xz} = I_{zx} = -\int\int\int xz\rho(x, y, z)\ dx\ dy\ dz \tag{2.22}$$

$$I_{yz} = I_{zy} = -\int\int\int yz\rho(x, y, z)\ dx\ dy\ dz \tag{2.23}$$

"If the mass distribution of the body is symmetric with respect to the body attached frame, then the cross products of inertia are identically zero" [10, p. 253].

2.4.1 Kinetic Energy

For an n link robot the kinetic energy can be expressed in terms of the Jacobian. By assuming that the mass of each link i is m_i and that the inertia matrix for each link i relative to the body frame of link i is $\mathbf{I}_i$, the equation for kinetic energy becomes

$$K_i = \frac{1}{2} m_i v_i^\mathsf{T} v_i + \frac{1}{2} \omega_i^\mathsf{T} \mathcal{I}_i \omega_i \tag{2.24}$$

$$K = \sum_{i=1}^{n} K_i \tag{2.25}$$

$$= \frac{1}{2} \dot{\boldsymbol{q}}^\mathsf{T} \left[\sum_{i=1}^{n} \{ m_i \boldsymbol{J}_{v_i}(\boldsymbol{q})^\mathsf{T} \boldsymbol{J}_{v_i}(\boldsymbol{q}) + \boldsymbol{J}_{\omega_i}(\boldsymbol{q})^\mathsf{T} \mathbf{R}_i(\boldsymbol{q}) \mathbf{I}_i \mathbf{R}_i(\boldsymbol{q})^\mathsf{T} \boldsymbol{J}_{\omega_i}(\boldsymbol{q}) \} \right] \dot{\boldsymbol{q}} \tag{2.26}$$

$$= \frac{1}{2} \dot{\boldsymbol{q}}^\mathsf{T} \mathbf{M}(\boldsymbol{q}) \dot{\boldsymbol{q}} \tag{2.27}$$

2.4.2 Potential Energy

For an n link robot the potential energy for the ith link of the robot can be expressed as

$$\mathbf{P}_i = m_i \boldsymbol{g}^\mathsf{T} \boldsymbol{r}_{ci} \tag{2.28}$$

where $\boldsymbol{g}$ is the gravity in the inertial frame and $\boldsymbol{r}_{ci}$ gives the coordinates for the center of mass for link i [10]. Then the total potential energy, which is independent of the joint velocity, $\dot{\boldsymbol{q}}$, becomes

$$\mathbf{P} = \sum_{i=1}^{n} \mathbf{P}_i \tag{2.29}$$

2.4.3 Euler-Lagrange Equations

The following calculations are from Chapter 7.3 "*Equations of Motion*" in "*Robot Modeling and Control*" [10] by Spong. Based on the kinetic and potential energy the Euler-Lagrange equations can be calculated as

$$\frac{d}{dt}\frac{\partial \mathcal{L}}{\partial \dot{q}_k} - \frac{\partial \mathcal{L}}{\partial q_k} = \tau_k, \qquad k = 1, \ldots, n \tag{2.30}$$

where

$$\mathcal{L} = \mathcal{K} - \mathcal{P} = \frac{1}{2}\sum_{k,j} m_{kj}(q)\dot{q}_k\dot{q}_j - P(q) \tag{2.31}$$

The partial derivative with respect to the kth joint velocity is

$$\frac{\partial \mathcal{L}}{\partial \dot{q}_k} = \sum_j m_{kj}(q)\dot{q}_j \tag{2.32}$$

and the derivative is

$$\frac{d}{dt}\frac{\partial \mathcal{L}}{\partial \dot{q}_k} = \sum_j m_{kj}(q)\ddot{q}_j + \sum_{i,j}\frac{\partial m_{kj}}{\partial \dot{q}_i}(q)\dot{q}_i\dot{q}_j \tag{2.33}$$

The partial derivative with respect to the kth joint position is

$$\frac{\partial \mathcal{L}}{\partial q_k} = \frac{1}{2}\sum_{i,j}\frac{\partial m_{ij}}{\partial q_k}\dot{q}_i\dot{q}_j - \frac{\partial P}{\partial q_k} \tag{2.34}$$

By putting Equations (2.33) and (2.34) into Equation (2.31) the Euler-Lagrange equations for each $k = 1, \ldots, n$ becomes

$$\sum_j m_{kj}(q)\ddot{q}_j + \sum_{i,j}\frac{\partial m_{kj}}{\partial \dot{q}_i}(q)\dot{q}_i\dot{q}_j - \frac{1}{2}\sum_{i,j}\frac{\partial m_{ij}}{\partial q_k}\dot{q}_i\dot{q}_j - \frac{\partial P}{\partial q_k} = \tau_k \tag{2.35}$$

$$\sum_j m_{kj}(q)\ddot{q}_j + \sum_{i,j}\left\{\frac{\partial m_{kj}}{\partial \dot{q}_i}(q)\dot{q}_i\dot{q}_j - \frac{1}{2}\frac{\partial m_{ij}}{\partial q_k}\dot{q}_i\dot{q}_j\right\} - \frac{\partial P}{\partial q_k} = \tau_k \tag{2.36}$$

By interchanging the order of summation and taking advantage of the symmetry

$$\left\{ \frac{\partial m_{kj}}{\partial \dot{q}_i}(q)\dot{q}_i\dot{q}_j - \frac{1}{2}\frac{\partial m_{ij}}{\partial q_k}\dot{q}_i\dot{q}_j \right\} \tag{2.37}$$

can be written as

$$\frac{1}{2}\left\{ \frac{\partial m_{kj}}{\partial q_i} + \frac{\partial m_{ki}}{\partial q_j} - \frac{\partial m_{ij}}{\partial q_k} \right\} \tag{2.38}$$

which again is the Christoffel symbols which has the abbreviation c_{ijk}. From this point $\frac{\partial P}{\partial q_k}$ is defined as g_k. Now the Euler-Lagrange equations can be written as

$$\sum_{j=1}^{n} m_{kj}(q)\ddot{q}_j + \sum_{i=1}^{n}\sum_{j=1}^{n} c_{ijk}(q)\dot{q}_i\dot{q}_j + g_k(q) = \tau_k, \qquad k = 1, \ldots, n \tag{2.39}$$

By collecting terms this can be written in matrix form as

$$\mathbf{M}(\boldsymbol{q})\ddot{\boldsymbol{q}} + \mathbf{C}(\boldsymbol{q}, \dot{\boldsymbol{q}})\dot{\boldsymbol{q}} + \boldsymbol{g}(\boldsymbol{q}) = \boldsymbol{\tau} \tag{2.40}$$

which is the same as Equation (2.1).

2.5 System Identification

For a robot manipulator system which has a known physical model with a known model structure the so called gray box identification is needed to find the unknown physical parameters. "Model sets with adjustable parameters with physical interpretation may, accordingly, be called *gray boxes*" [9, p. 13].

For such a system one has known quantities placed in the vector $\boldsymbol{\varphi}(t) \in \mathbb{R}^n$, unknown parameters placed in the vector $\boldsymbol{\theta} \in \mathbb{R}^n$ and the measurable quantity placed in the scalar $y(t)$ [13]. From this the model structure can be written as

$$y(t) = \boldsymbol{\varphi}^{\mathsf{T}}(t)\boldsymbol{\theta} \tag{2.41}$$

"The elements of the vector $\boldsymbol{\varphi}(t)$ are often called regression variables or regressors while $y(t)$ is called the regressed variable. We will call $\boldsymbol{\theta}$ the parameter vector. The variable t takes integer values." [13, p. 60]

One simple example for rewriting a differential system to the form shown in Equation (2.41) is a cart pendulum system. The mathematical model describing the physical characteristics of the cart pendulum can be seen in Equation (2.42).

$$\ddot{\theta} + a\sin(\theta) = -bu \tag{2.42}$$

where θ indicate the angle of the pendulum, $a = \frac{mgl}{J}$ and $b = \frac{k_u}{J}$ are unknown compound pendulum parameters, m is the mass of the pendulum system, l is the distance from the center of mass of the pendulum system to the pivot point, J is the moment of inertia of the pendulum system, k_u is a transfer constant of the DC-motor and g is the gravitational acceleration [3].

The regression model for the model presented in Equation (2.42) can be created with filters as shown in Equations (2.43) - (2.45).

$$\xi_1(t) = \frac{\lambda^2}{p^2 + 2\lambda p + \lambda^2}\theta(t) \tag{2.43}$$

$$\xi_2(t) = \frac{\lambda^2}{p^2 + 2\lambda p + \lambda^2}\nu(t) \tag{2.44}$$

$$\xi_3(t) = \frac{\lambda^2}{p^2 + 2\lambda p + \lambda^2}u(t) \tag{2.45}$$

where $p = d/dt$ is the differential operator, $u(t)$ is the control input, $\lambda > 0$ is a positive constant and $\nu(t) = \sin(\theta)$. After this parametrization the model can be rewritten into the form of Equation (2.41) where $y(t) = \ddot{\xi}_1(t)$, $\boldsymbol{\varphi}^\mathsf{T}(t) = [\xi_2(t)\ \xi_3(t)]$ and $\boldsymbol{\theta}^\mathsf{T} = [-a\ \ -b]$.

By using least squares one can estimate $\hat{\boldsymbol{\theta}}$ using measurements for $y(1)$, $\varphi(1)$, $\ldots$, $y(N)$, $\varphi(N)$, where N is the number of measured values. From these measurements a overdetermined system of linear equations is obtained

$$\begin{aligned} y(1) &= \boldsymbol{\varphi}^\mathsf{T}(1)\boldsymbol{\theta} \\ y(2) &= \boldsymbol{\varphi}^\mathsf{T}(2)\boldsymbol{\theta} \\ &\vdots \\ y(N) &= \boldsymbol{\varphi}^\mathsf{T}(N)\boldsymbol{\theta} \end{aligned}$$

Using matrix notation the system of linear equations can be written as

$$\boldsymbol{Y} = \boldsymbol{\Phi}\boldsymbol{\theta} \tag{2.46}$$

where $\boldsymbol{Y}$ and $\boldsymbol{\Phi}$ are

$$\boldsymbol{Y} = \begin{pmatrix} y(1) \\ y(2) \\ \vdots \\ y(N) \end{pmatrix} \tag{2.47}$$

$$\boldsymbol{\Phi} = \begin{pmatrix} \boldsymbol{\varphi}^\mathsf{T}(1) \\ \boldsymbol{\varphi}^\mathsf{T}(2) \\ \vdots \\ \boldsymbol{\varphi}^\mathsf{T}(N) \end{pmatrix} \tag{2.48}$$

From "*System Identification*" [13] by Söderström and Stoica it is given that the least squares estimate of $\boldsymbol{\theta}$ is defined as the vector $\hat{\boldsymbol{\theta}}$ that minimizes the loss function

$$V(\boldsymbol{\theta}) = \frac{1}{2}\sum_{t=1}^{N} \boldsymbol{\varepsilon}^2(t) = \frac{1}{2}\boldsymbol{\varepsilon}^{\mathsf{T}}\boldsymbol{\varepsilon} = \frac{1}{2}\|\boldsymbol{\varepsilon}\|^2 \tag{2.49}$$

where $\varepsilon(t)$ is the equation error

$$\varepsilon(t) = y(t) - \boldsymbol{\varphi}^{\mathsf{T}}(t)\boldsymbol{\theta} \tag{2.50}$$

The equation error stacked in the same manner as for $\boldsymbol{Y}$ and $\boldsymbol{\Phi}$ in Equations (2.47) and (2.48) gives $\boldsymbol{\varepsilon}$

$$\boldsymbol{\varepsilon} = \begin{pmatrix} \varepsilon(1) \\ \vdots \\ \varepsilon(N) \end{pmatrix} \tag{2.51}$$

The solution of the optimization problem is given by Lemma 4.1. in "*System Identification*" [13] by Söderström and Stoica. For the cases where the matrix $\boldsymbol{\Phi}^{\mathsf{T}}\boldsymbol{\Phi}$ is positive definite the unique minimum point for $V(\boldsymbol{\theta})$ is given by

$$\hat{\boldsymbol{\theta}} = (\boldsymbol{\Phi}^{\mathsf{T}}\boldsymbol{\Phi})^{-1}\boldsymbol{\Phi}^{\mathsf{T}}\boldsymbol{Y} \tag{2.52}$$

The proof of this Lemma can be seen in "*System Identification*" [13] by Söderström and Stoica.

2.6 Statistical Properties

It is assumed that the model structure from Equation (2.41) is perturbated by a general disturbance. Equation (2.41) then becomes

$$y(t) = \boldsymbol{\varphi}^{\mathsf{T}}(t)\boldsymbol{\theta} + w_0(t) \tag{2.53}$$

where the statistical properties of the disturbance is assumed to be given by

$$E[w_0(t)] = 0 \tag{2.54}$$
$$E[w_0(t)w_0(s)] = r_{ts} \tag{2.55}$$

Using the matrix form previously presented this becomes

$$\mathbf{Y} = \boldsymbol{\Phi}\boldsymbol{\theta} + \mathbf{W} \tag{2.56}$$

where the statistical properties of the disturbance becomes

$$E[\mathbf{W}] = 0 \tag{2.57}$$
$$E[\mathbf{W}\mathbf{W}^{\mathsf{T}}] = \mathbf{R} \tag{2.58}$$

where

$$\mathbf{R} = \sigma\mathbf{I} \tag{2.59}$$

Here $\mathbf{I}$ is the identity matrix.

By using Lemma II.1 in Appendix II in "*System Identification; Theory for the User*" [9] by Ljung the estimate of the variance can be calculated. This Lemma states that the estimate of the variance σ in Equation (2.59) can be written as

$$\hat{\sigma} = \frac{N}{N-d}V(\hat{\boldsymbol{\theta}}) = \frac{1}{N-d}\sum_{t=1}^{N}[y(t) - \boldsymbol{\varphi}^{\mathsf{T}}(t)\hat{\boldsymbol{\theta}}]^2 \tag{2.60}$$

The proof of this Lemma can be found in Appendix II in "*System Identification; Theory for the User*" [9] by Ljung.

2.7 Persistent Excitation

"A fundamental problem concerning parametrized model sets is whether a parameter value can be uniquely determined based on input-output measurements" [7, p. 3236]. From this problem one property about the input signal called persistence of excitation can be deduced. That is, for the system to have persistent excitation the input signal has to be "general enough" to allow distinction. See Definition 3 in "*Model structure identifiability and persistence of excitation*" [7] by Glad and Ljung for a generalized version of the concept of persistence of excitation.

2.8 Measurement Filtering

To use the system identification method described in Section 2.5, measurements from the system to be identified are needed. Such measurements usually include disturbances caused by the environment. This could make it difficult to achieve consistent results for the unknown parameters to be estimated. These disturbances might also induce bias in the estimated values.

The inertia of the robot manipulator prevents it from having high frequency movements, therefore it is reasonable to assume that the information of interest should be at low frequencies. Noise at high frequencies can therefore be removed using a low pass filter, where the cut off frequency can be decided using a power density spectrum. The power density spectrum of the signal can be found using Fast Fourier Transform (FFT). It is assumed that high power at low frequencies contains the information of interest and therefore should be preserved.

It is difficult to distinguish between disturbances and information of interest if they are present at the same frequencies. The disturbance at this bandwidth might therefore still induce biases and make it difficult to find estimates which are consistent.

2.9 Fast Fourier Transform

Fast Fourier Transform (FFT) is an efficient algorithm for calculation of the Discrete Fourier Transform (DFT) [5]. This is usually done on a digital signal processor [12]. The Fourier transform $X(\omega)$ of a discrete-time signal $x(n)$ has to be done to perform a frequency analysis of the signal. The Fourier transform is an aperiodic finite energy signal and hence has a continuous spectrum. For an aperiodic discrete time signal $x(n)$ the Fourier transform is

$$X(\omega) = \sum_{n=-\infty}^{\infty} x(n)e^{-j\omega n} \tag{2.61}$$

A set of N samples $\{X(k)\}$ of the Fourier transform $X(\omega)$ is used to make the DFT. Where "[t]he sampling of $X(\omega)$ occurs at N equally spaced frequencies $\omega_k = 2\pi k/N$, $k = 0, 1, 2, ..., N-1$" [12, p. 464]

The DFT for an N-point sequence $\{x(n)\}$ is

$$X(k) = \sum_{n=0}^{N-1} x(n)W_N^{kn} \tag{2.62}$$

where

$$W_N = e^{-j2\pi/N} \tag{2.63}$$

There are many different algorithms to calculate the FFT for a discrete-time signal. For this thesis the MATLAB function `fft(x)` was used, where x is the discrete time signal to be taken the FFT of. To read more about different FFT algorithms see Chapter 7 and 8 in "*Digital Signal Processing*" [12] by Proakis and Manolakis.

2.10 Passivity-Based Robust Controller

When the system equations are calculated and the unknown parameters are estimated using system identification methods, it is desirable to create a controller for the system. There are many different approaches for controlling a robot, passivity-based robust controller is one of those approaches. This controller will be introduced in this section. The following theory is found in Chapter 8.4.1 "*Passivity-Based Robust Control*" in "*Robot Modeling and Control*" [10] by Spong .

The Euler-Lagrange equations written in matrix form for a robot manipulator are

$$\mathbf{M}(\boldsymbol{q})\ddot{\boldsymbol{q}} + \mathbf{C}(\boldsymbol{q}, \dot{\boldsymbol{q}})\dot{\boldsymbol{q}} + \boldsymbol{g}(\boldsymbol{q}) = \boldsymbol{u} \tag{2.64}$$

where $\boldsymbol{u}$, the control input, is given as

$$\boldsymbol{u} = \hat{\mathbf{M}}(\boldsymbol{q})\boldsymbol{a} + \hat{\mathbf{C}}(\boldsymbol{q}, \dot{\boldsymbol{q}})\boldsymbol{v} + \hat{\boldsymbol{g}}(\boldsymbol{q}) - \mathbf{K}\boldsymbol{r} \tag{2.65}$$

where the notation $\hat{(\cdot)}$ represent the estimated value of $(\cdot)$ and $\boldsymbol{v}$, $\boldsymbol{a}$ and $\boldsymbol{r}$ are defined as

$$\boldsymbol{v} = \dot{\boldsymbol{q}}^d - \boldsymbol{\Lambda}\tilde{\boldsymbol{q}} \tag{2.66}$$
$$\boldsymbol{a} = \dot{\boldsymbol{v}} = \ddot{\boldsymbol{q}}^d - \boldsymbol{\Lambda}\dot{\tilde{\boldsymbol{q}}} \tag{2.67}$$
$$\boldsymbol{r} = \dot{\boldsymbol{q}} - \boldsymbol{v} = \dot{\tilde{\boldsymbol{q}}} + \boldsymbol{\Lambda}\tilde{\boldsymbol{q}} \tag{2.68}$$

Here $\boldsymbol{q}^d$ is desired joint position, $\boldsymbol{q}$, and $\mathbf{K}$ and $\boldsymbol{\Lambda}$ are diagonal matrices of constant, positive gains. $\tilde{\boldsymbol{q}}$ and $\dot{\tilde{\boldsymbol{q}}}$ are defined as

$$\tilde{\boldsymbol{q}} = \boldsymbol{q} - \boldsymbol{q}^d \tag{2.69}$$
$$\dot{\tilde{\boldsymbol{q}}} = \dot{\boldsymbol{q}} - \dot{\boldsymbol{q}}^d \tag{2.70}$$

The control input can be rewritten as

$$\boldsymbol{u} = \boldsymbol{Y}(\boldsymbol{q}, \dot{\boldsymbol{q}}, \boldsymbol{a}, \boldsymbol{v})\hat{\boldsymbol{\theta}} - \mathbf{K}\boldsymbol{r} \tag{2.71}$$

Inserting Equation (2.71) into Equation (2.64) gives

$$\mathbf{M}(\boldsymbol{q})\ddot{\boldsymbol{q}} + \mathbf{C}(\boldsymbol{q}, \dot{\boldsymbol{q}})\dot{\boldsymbol{q}} + \boldsymbol{g}(\boldsymbol{q}) = \boldsymbol{Y}(\boldsymbol{q}, \dot{\boldsymbol{q}}, \boldsymbol{a}, \boldsymbol{v})\hat{\boldsymbol{\theta}} - \mathbf{K}\boldsymbol{r} \tag{2.72}$$

From this point $\mathbf{M}(\boldsymbol{q})$ is written as $\mathbf{M}$, $\mathbf{C}(\boldsymbol{q}, \dot{\boldsymbol{q}})$ is written as $\mathbf{C}$, $\boldsymbol{g}(\boldsymbol{q})$ is written as $\boldsymbol{g}$, and $\boldsymbol{Y}(\boldsymbol{q}, \dot{\boldsymbol{q}}, \boldsymbol{a}, \boldsymbol{v})$ is written as $\mathbf{Y}$. By subtracting $\mathbf{M}\boldsymbol{a}$ and $\mathbf{C}\boldsymbol{v}$ from both sides of Equation (2.72), this becomes

$$\mathbf{M}(\ddot{\boldsymbol{q}} - \boldsymbol{a}) + \mathbf{C}(\dot{\boldsymbol{q}} - \boldsymbol{v}) + \boldsymbol{g} = \boldsymbol{Y}\hat{\boldsymbol{\theta}} - \mathbf{K}\boldsymbol{r} - \mathbf{M}\boldsymbol{a} - \mathbf{C}\boldsymbol{v} \tag{2.73}$$

$$\mathbf{M}(\ddot{\boldsymbol{q}} - \boldsymbol{a}) + \mathbf{C}(\dot{\boldsymbol{q}} - \boldsymbol{v}) + \mathbf{K}\boldsymbol{r} = \boldsymbol{Y}\hat{\boldsymbol{\theta}} - \mathbf{M}\boldsymbol{a} - \mathbf{C}\boldsymbol{v} - \boldsymbol{g} \tag{2.74}$$

Then let

$$\mathbf{Y}\boldsymbol{\theta} = \mathbf{M}\boldsymbol{a} + \mathbf{C}\boldsymbol{v} + \boldsymbol{g} \tag{2.75}$$

By using Equation (2.75) and the definition of $\boldsymbol{r}$ in Equation (2.68), Equation (2.72) becomes

$$\mathbf{M}\dot{\boldsymbol{r}} + \mathbf{C}\boldsymbol{r} + \mathbf{K}\boldsymbol{r} = \boldsymbol{Y}(\hat{\boldsymbol{\theta}} - \boldsymbol{\theta}) \tag{2.76}$$

The term $\hat{\boldsymbol{\theta}}$ in Equation (2.71) is chosen as

$$\hat{\boldsymbol{\theta}} = \boldsymbol{\theta}_0 + \delta\boldsymbol{\theta} \tag{2.77}$$

It is assumed that $\boldsymbol{\theta}_0$ is a fixed nominal parameter vector and that $\delta\boldsymbol{\theta}$ is an additional control term. Inserting this into Equation (2.76), gives

$$\mathbf{M}\dot{\boldsymbol{r}} + \mathbf{C}\boldsymbol{r} + \mathbf{K}\boldsymbol{r} = \boldsymbol{Y}(\tilde{\boldsymbol{\theta}} + \delta\boldsymbol{\theta}) \tag{2.78}$$

where the parametric uncertainty of the system is given by $\tilde{\boldsymbol{\theta}} = \boldsymbol{\theta}_0 - \boldsymbol{\theta}$.

If there exist a constant $\rho \geq 0$, so that the uncertainty can be bounded like this

$$\|\tilde{\boldsymbol{\theta}}\| = \|\boldsymbol{\theta} - \boldsymbol{\theta}_0\| \leq \rho \tag{2.79}$$

then the additional term $\delta\boldsymbol{\theta}$ can be designed according to

$$\delta\boldsymbol{\theta} = \begin{cases} -\rho \frac{\boldsymbol{Y}^\mathsf{T}\boldsymbol{r}}{\|\boldsymbol{Y}^\mathsf{T}\boldsymbol{r}\|}; & \text{if } \|\boldsymbol{Y}^\mathsf{T}\boldsymbol{r}\| > \epsilon \\ -\frac{\rho}{\epsilon}\boldsymbol{Y}^\mathsf{T}\boldsymbol{r}; & \text{if} \|\boldsymbol{Y}^\mathsf{T}\boldsymbol{r}\| \leq \epsilon \end{cases} \tag{2.80}$$

Then consider the Lyapunov function candidate

$$V = \frac{1}{2}\boldsymbol{r}^\mathsf{T}\mathbf{M}\boldsymbol{r} + \tilde{\boldsymbol{q}}^\mathsf{T}\boldsymbol{\Lambda}\mathbf{K}\tilde{\boldsymbol{q}} \tag{2.81}$$

The calculation of $\dot{V}$ becomes

$$\dot{V} = \dot{\boldsymbol{r}}^\mathsf{T}\mathbf{M}\boldsymbol{r} + \frac{1}{2}\boldsymbol{r}^\mathsf{T}\dot{\mathbf{M}}\boldsymbol{r} + 2\dot{\tilde{\boldsymbol{q}}}^\mathsf{T}\boldsymbol{\Lambda}\mathbf{K}\tilde{\boldsymbol{q}} \tag{2.82}$$

$$= \frac{1}{2}\boldsymbol{r}^\mathsf{T}2\mathbf{C}\boldsymbol{r} - \frac{1}{2}\boldsymbol{r}^\mathsf{T}2\mathbf{C}\boldsymbol{r} + \dot{\boldsymbol{r}}^\mathsf{T}\mathbf{M}\boldsymbol{r} + \frac{1}{2}\boldsymbol{r}^\mathsf{T}\dot{\mathbf{M}}\boldsymbol{r} + 2\dot{\tilde{\boldsymbol{q}}}^\mathsf{T}\boldsymbol{\Lambda}\mathbf{K}\tilde{\boldsymbol{q}} \tag{2.83}$$

$$= \frac{1}{2}\boldsymbol{r}^\mathsf{T}(\dot{\mathbf{M}} - 2\mathbf{C})\boldsymbol{r} + \boldsymbol{r}^\mathsf{T}\mathbf{C}\boldsymbol{r} + \dot{\boldsymbol{r}}^\mathsf{T}\mathbf{M}\boldsymbol{r} + 2\dot{\tilde{\boldsymbol{q}}}^\mathsf{T}\boldsymbol{\Lambda}\mathbf{K}\tilde{\boldsymbol{q}} \tag{2.84}$$

Now $\boldsymbol{r}^\mathsf{T}\mathbf{C}\boldsymbol{r} + \dot{\boldsymbol{r}}^\mathsf{T}\mathbf{M}\boldsymbol{r}$ can be written as

$$\boldsymbol{r}^\mathsf{T}\mathbf{C}\boldsymbol{r} + \dot{\boldsymbol{r}}^\mathsf{T}\mathbf{M}\boldsymbol{r} = \boldsymbol{r}^\mathsf{T}\mathbf{C}\boldsymbol{r} + \boldsymbol{r}^\mathsf{T}\mathbf{M}\dot{\boldsymbol{r}} \tag{2.85}$$

$$= \boldsymbol{r}^\mathsf{T}(\mathbf{M}\dot{\boldsymbol{r}} + \mathbf{C}\boldsymbol{r}) \tag{2.86}$$

$$= \boldsymbol{r}^\mathsf{T}(-\mathbf{K}\boldsymbol{r} + \mathbf{Y}(\tilde{\boldsymbol{\theta}} + \delta\boldsymbol{\theta})) \tag{2.87}$$

Using this gives

$$\dot{V} = \frac{1}{2}\boldsymbol{r}^\mathsf{T}(\dot{\mathbf{M}} - 2\mathbf{C})\boldsymbol{r} - \boldsymbol{r}^\mathsf{T}\mathbf{K}\boldsymbol{r} + \boldsymbol{r}^\mathsf{T}\mathbf{Y}(\tilde{\boldsymbol{\theta}} + \delta\boldsymbol{\theta}) + 2\dot{\tilde{\boldsymbol{q}}}^\mathsf{T}\boldsymbol{\Lambda}\mathbf{K}\tilde{\boldsymbol{q}} \tag{2.88}$$

From the skew symmetry property it is given that $(\dot{\mathbf{M}} - 2\mathbf{C})$ is zero.

Using the definition of $\boldsymbol{r}$, $-\boldsymbol{r}^{\mathsf{T}}\mathbf{K}\boldsymbol{r}$ can be written as

$$-\boldsymbol{r}^{\mathsf{T}}\mathbf{K}\boldsymbol{r} = -(\dot{\tilde{\boldsymbol{q}}} + \boldsymbol{\Lambda}\tilde{\boldsymbol{q}})^{\mathsf{T}}\mathbf{K}(\dot{\tilde{\boldsymbol{q}}} + \boldsymbol{\Lambda}\tilde{\boldsymbol{q}}) \tag{2.89}$$

$$= -\dot{\tilde{\boldsymbol{q}}}^{\mathsf{T}}\mathbf{K}\dot{\tilde{\boldsymbol{q}}} - 2\tilde{\boldsymbol{q}}^{\mathsf{T}}\Lambda\mathbf{K}\tilde{\boldsymbol{q}} - \tilde{\boldsymbol{q}}^{\mathsf{T}}\boldsymbol{\Lambda}\mathbf{K}\boldsymbol{\Lambda}\tilde{\boldsymbol{q}} \tag{2.90}$$

By using Equation (2.90) and the skew symmetry property, Equation (2.88) reduces to

$$\dot{V} = -\dot{\tilde{\boldsymbol{q}}}^{\mathsf{T}}\mathbf{K}\dot{\tilde{\boldsymbol{q}}} - \tilde{\boldsymbol{q}}^{\mathsf{T}}\boldsymbol{\Lambda}\mathbf{K}\boldsymbol{\Lambda}\tilde{\boldsymbol{q}} + \boldsymbol{r}^{\mathsf{T}}\mathbf{Y}(\tilde{\boldsymbol{\theta}} + \delta\boldsymbol{\theta}) \tag{2.91}$$

$$= -\boldsymbol{e}^{\mathsf{T}}\mathbf{Q}\boldsymbol{e} + \boldsymbol{r}^{\mathsf{T}}\mathbf{Y}(\tilde{\boldsymbol{\theta}} - \delta\boldsymbol{\theta}) \tag{2.92}$$

where

$$\mathbf{Q} = \begin{bmatrix} \boldsymbol{\Lambda}^{\mathsf{T}}\mathbf{K}\boldsymbol{\Lambda} & \mathbf{0} \\ \mathbf{0} & \mathbf{K} \end{bmatrix} \tag{2.93}$$

and

$$\boldsymbol{e} = \begin{bmatrix} \tilde{\boldsymbol{q}} \\ \dot{\tilde{\boldsymbol{q}}} \end{bmatrix} \tag{2.94}$$

Uniform ultimate boundedness of the tracking error is established with the control $\delta\boldsymbol{\theta}$ from Equation (2.80), as long as there is a constant bound ρ for the constant vector $\tilde{\boldsymbol{\theta}}$.

Chapter 3

Identification of parameters for the 6th joint of IRB 140

The methods described in Sections 2.2 - 2.4 were used to calculate the matrices $\mathbf{M}$ and $\mathbf{C}$, and the vector $\boldsymbol{g}$ in Equation 2.1. These calculations were computed in Maple. The Maple code used for these calculations was based on a Maple code obtained from Stepan Pchelkin, which calculated the matrices and vector for the first 3 joints of IRB 140. The code used for this thesis can be found using the description in Appendix A. For practical reasons these matrices were not included here.

It was decided to only concentrate on the 6th equation of the system, where the centrifugal and Coriolis forces for the 6th joint are zero. The equations for the 6th joint of IRB 140 were obtained by setting q_1-q_5 to zero. Then the matrix $\mathbf{C}$ only contains the friction force, and for simplicity $\mathbf{C}(6,6)\dot{q}_6$ is written as $\boldsymbol{F}(6,1)$.

In order to verify the identification method, it was first tested on a simulated model with known parameters. Then the same method was applied to the filtered measurements from IRB 140 to estimate the unknown parameters for the 6th joint.

It is assumed that noise is absent for the simulation, and present for the estimations using filtered measurements.

3.1 Equations for System Identification

The matrix form of the Euler-Lagrange equations for the 6th joint of IRB 140 is written as

$$\mathbf{M}(6,6)\ddot{q}_6 + \boldsymbol{G}(1,6) + \boldsymbol{F}(6,1) = \boldsymbol{\tau}(6,1) \tag{3.1}$$

where the friction model is assumed to be Coulomb friction combined with viscous friction.

$$\boldsymbol{F}(6,1) = a\ sign(\dot{q}_6) + b\ \dot{q}_6 \tag{3.2}$$

For more information about friction see Chapter 5 "*Friction*" in "*Modeling and Simulation for Automatic Control*" [4] by Egeland and Gravdahl.

The gravity forces are given by

$$\boldsymbol{G}(1,6) = m_6\ lm_{x6}\ g\ \sin(q_6) + m_6\ lm_{y6}\ g\ \cos(q_6) \tag{3.3}$$

Written out Equation (3.1) is

$$\begin{aligned} &\ddot{q}_6\left[m_6\ lm_{x6}^2 + m_6\ lm_{y6}^2 + I_{6z}\right] + a\ sign(\dot{q}_6) + b\ \dot{q}_6 \\ &\quad + m_6\ lm_{x6}\ g\ \sin(q_6) + m_6\ lm_{y6}\ g\ \cos(q_6) = u \end{aligned} \tag{3.4}$$

This may be written as

$$\begin{aligned} \ddot{q}_6 = &- \frac{a\ sign(\dot{q}_6)}{m_6\ lm_{x6}^2 + m_6\ lm_{y6}^2 + I_{6z}} \\ &- \frac{b\ \dot{q}_6}{m_6\ lm_{x6}^2 + m_6\ lm_{y6}^2 + I_{6z}} \\ &- \frac{m_6\ lm_{x6}\ g\ \sin(q_6)}{m_6\ lm_{x6}^2 + m_6\ lm_{y6}^2 + I_{6z}} \\ &- \frac{m_6\ lm_{y6}\ g\ \cos(q_6)}{m_6\ lm_{x6}^2 + m_6\ lm_{y6}^2 + I_{6z}} \\ &+ \frac{u}{m_6\ lm_{x6}^2 + m_6\ lm_{y6}^2 + I_{6z}} \end{aligned} \tag{3.5}$$

From which the unknown parameters are given as

$$k_1 = \frac{a}{m_6\ lm_{x6}^2 + m_6\ lm_{y6}^2 + I_{6z}} \tag{3.6}$$

$$k_2 = \frac{b}{m_6\ lm_{x6}^2 + m_6\ lm_{y6}^2 + I_{6z}} \tag{3.7}$$

$$k_3 = \frac{m_6\ lm_{x6}}{m_6\ lm_{x6}^2 + m_6\ lm_{y6}^2 + I_{6z}} \tag{3.8}$$

$$k_4 = \frac{m_6\ lmy_6}{m_6\ lmx_6^2 + m_6\ lmy_6^2 + I_{6z}} \tag{3.9}$$

$$k_u = \frac{1}{m_6\ lm_{x6}^2 + m_6\ lm_{y6}^2 + I_{6z}} \tag{3.10}$$

Equation (3.1) can now be written as

$$\ddot{q}_6 = -\ k_1\ sign(\dot{q}_6) - k_2\ \dot{q}_6 - k_3\ g\ \sin(q_6) - k_4\ g\ \cos(q_6) + k_u\ u \tag{3.11}$$

Parametrized to fit into the regression model presented in Equation (2.41) this becomes

$$\xi_1(t) = \frac{\lambda^2}{p^2 + 2\lambda p + \lambda^2} q_6 \tag{3.12}$$

$$\xi_2(t) = -\frac{\lambda^2}{p^2 + 2\lambda p + \lambda^2} sign(\dot{q}_6) \tag{3.13}$$

$$\xi_3(t) = -\frac{\lambda^2}{p^2 + 2\lambda p + \lambda^2} \dot{q}_6 \tag{3.14}$$

$$\xi_4(t) = -\frac{\lambda^2}{p^2 + 2\lambda p + \lambda^2} g \sin(q_6) \tag{3.15}$$

$$\xi_5(t) = \frac{\lambda^2}{p^2 + 2\lambda p + \lambda^2} g \cos(q_6) \tag{3.16}$$

$$\xi_6(t) = \frac{\lambda^2}{p^2 + 2\lambda p + \lambda^2} u(t) \tag{3.17}$$

From this $y(t) = \ddot{\xi}_1$, $\boldsymbol{\varphi}^\mathsf{T} = [\xi_2\ \xi_3\ \xi_4\ \xi_5\ \xi_6]$, $\boldsymbol{\theta}^\mathsf{T} = [k_1\ k_2\ k_3\ k_4\ k_u]$.

The estimate of the unknown parameters can then be found using the LS-method by solving

$$\hat{\boldsymbol{\theta}} = (\boldsymbol{\Phi}^{\mathsf{T}}\boldsymbol{\Phi})^{-1}\boldsymbol{\Phi}^{\mathsf{T}}\boldsymbol{Y} \tag{3.18}$$

where $\boldsymbol{Y}$ and $\boldsymbol{\Phi}$ are created from measurements. Assuming there are some general disturbance perturbating the system, the estimated variance of disturbance is given by

$$\hat{\sigma} = \frac{1}{N-d}\sum_{t=1}^{N}\Big[y(t) - \boldsymbol{\varphi}^{\mathsf{T}}(t)\hat{\boldsymbol{\theta}}\Big]^2 \tag{3.19}$$

The calculations presented here are comprehensive and should preferably be solved using a computer program, e.g. MATLAB.

3.2 Simulation of Least Squares Method

The simulation of the 6th joint of IRB 140 and the estimation of the unknown parameters, k_1, k_2, k_3, k_4 and k_u, are computed in MATLAB. In Appendix A it is explained where to find the MATLAB code for the simulation and estimation. Table 3.1 shows the variable names used in the MATLAB code and in the figures containing plots created with MATLAB. Filtered q_6, $\dot{q}_6$ and $\ddot{q}_6$ from Equations (3.12) - (3.17) are given as ϕ, $\dot{\phi}$ and $\ddot{\phi}$ respectively.

Variable	**Simulation**	**Estimation**	**Verification Simulation**
Position	ϕ	ϕ_{est}	ϕ_{est2}
Velocity	$\dot{\phi}$	$\dot{\phi}_{est}$	$\dot{\phi}_{est2}$
Acceleration	$\ddot{\phi}$	$\ddot{\phi}_{est}$	$\ddot{\phi}_{est2}$
Control input	u	u_{est}	u_{est2}

Table 3.1: Variable names used in MATLAB code and in figures containing plots from MATLAB.

For this simulation of the 6th joint of IRB 140 the unknown parameters in Equations (3.6) - (3.10) are chosen as guesstimated values. These values can be seen in Table 3.2.

With this simulation, estimates for the five unknown parameters are computed. These estimates are presented as $\hat{\boldsymbol{\theta}}_1$. In parallel with the simulated model an estimated model is created, using ϕ and u from the simulation. Using this estimated model an alternative estimate called $\hat{\boldsymbol{\theta}}_2$ is computed. In Tables 3.3 and 3.4 the two different estimates are presented. The simulated and the estimated models used to create $\hat{\boldsymbol{\theta}}_1$ and $\hat{\boldsymbol{\theta}}_2$ are compared in Figures 3.1 - 3.8.

Based on the estimated values the variance of the disturbance is calculated using Equation (3.19). In Tables 3.5 and 3.6 the variance of the disturbances for the two estimates are given.

A new simulation is computed using the estimated values to verify if the estimated values are correct. By using the results from this estimation the discrepancy between this simulation and the verification simulation are obtained and presented in Figures 3.9 - 3.12. At the end the friction and gravity models for the two different estimates are presented in Figures 3.13 and 3.14.

k_1	=	0.0880
k_2	=	1.3376
k_3	=	2.8495
k_4	=	0.0032
k_u	=	0.5884

Table 3.2: $\boldsymbol{\theta}$, parameters used to simulate the robot.

$\hat{k}_1$	=	0.0878
$\hat{k}_2$	=	1.3377
$\hat{k}_3$	=	2.8491
$\hat{k}_4$	=	0.0032
$\hat{k}_u$	=	0.5883

Table 3.3: $\hat{\boldsymbol{\theta}}_1$, estimate of unknown parameters.

$\hat{k}_1$	=	0.0880
$\hat{k}_2$	=	1.3376
$\hat{k}_3$	=	2.8495
$\hat{k}_4$	=	0.0032
$\hat{k}_u$	=	0.5884

Table 3.4: $\hat{\boldsymbol{\theta}}_2$, estimate of unknown parameters.

$\hat{\sigma}_1$	=	$1.0468 \cdot 10^{-4}$

Table 3.5: $\hat{\sigma}_1$, estimated variance of the disturbance for $\hat{\boldsymbol{\theta}}_1$.

$\hat{\sigma}_2$	=	$1.0471 \cdot 10^{-4}$

Table 3.6: $\hat{\sigma}_2$, estimated variance of the disturbance for $\hat{\boldsymbol{\theta}}_2$.

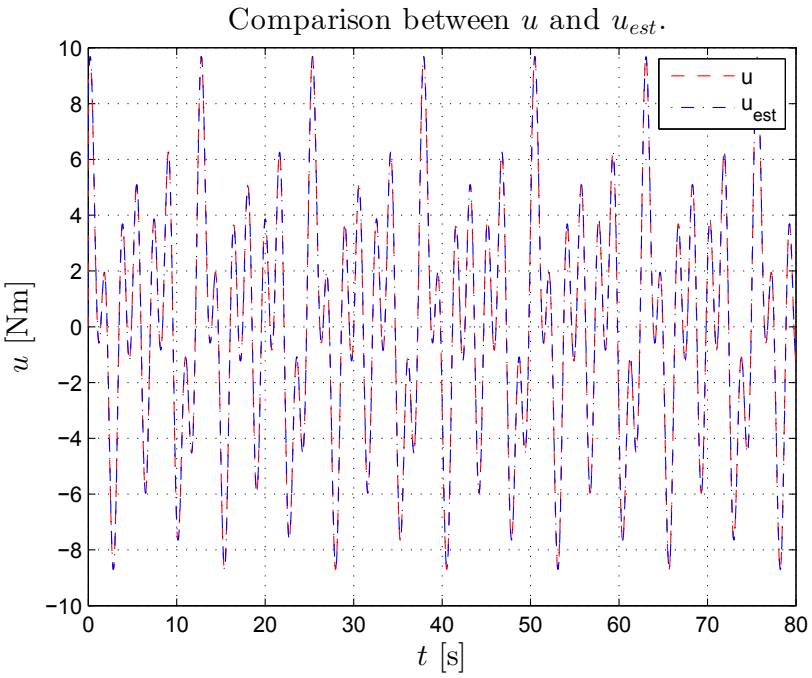

Figure 3.1: MATLAB plot displaying the control input u(t).

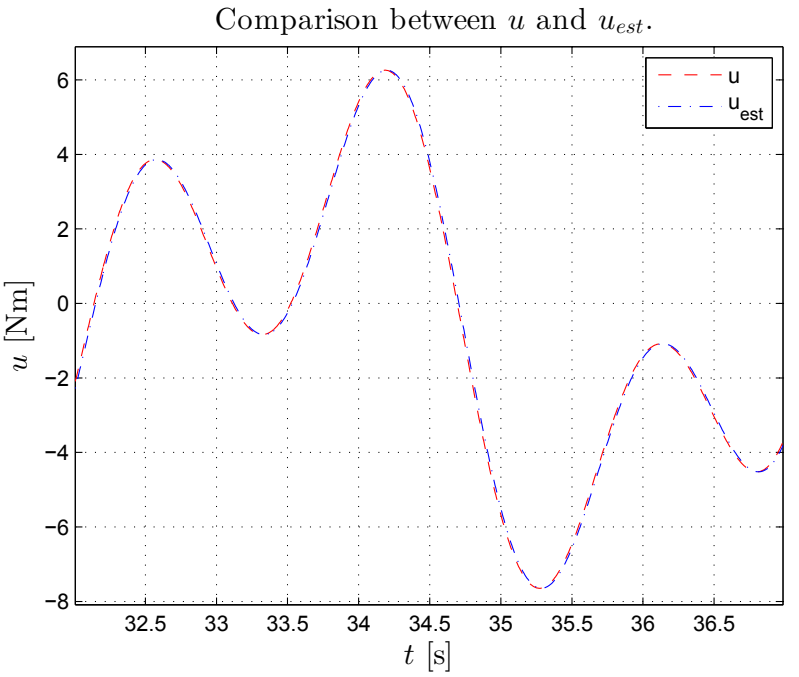

Figure 3.2: Detail from the MATLAB plot displaying the control input u(t).

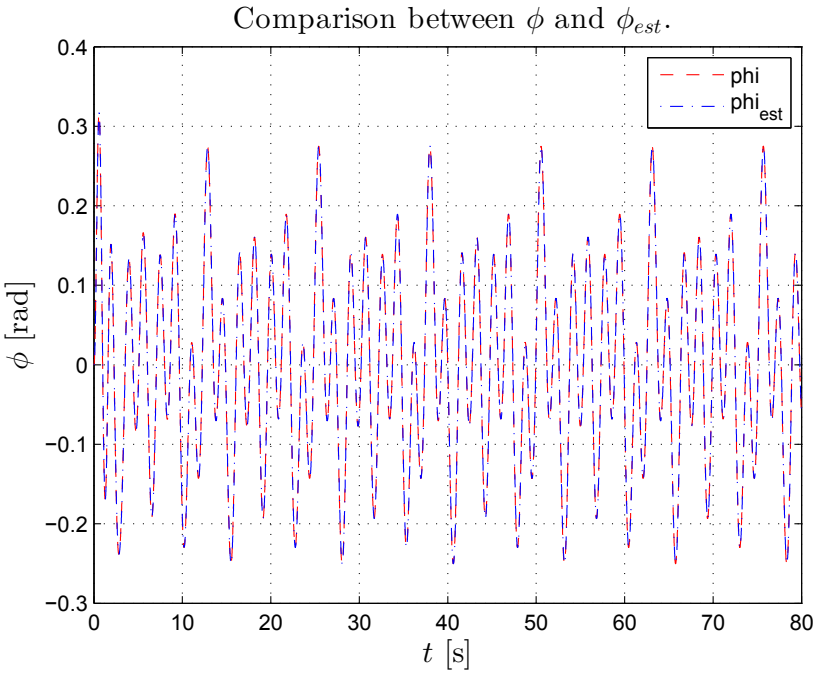

Figure 3.3: MATLAB plot displaying the position ϕ(t).

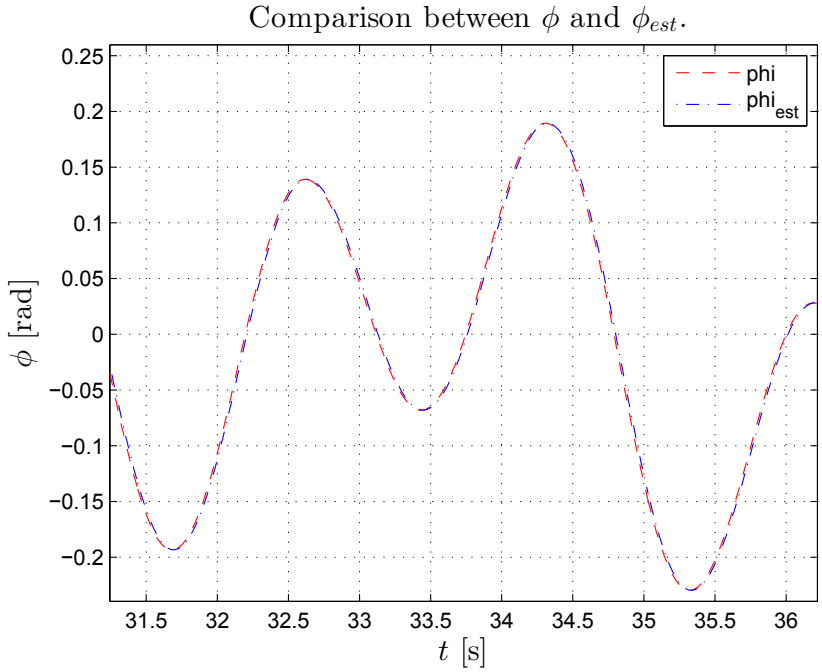

Figure 3.4: Detail from the MATLAB plot displaying the position ϕ(t).

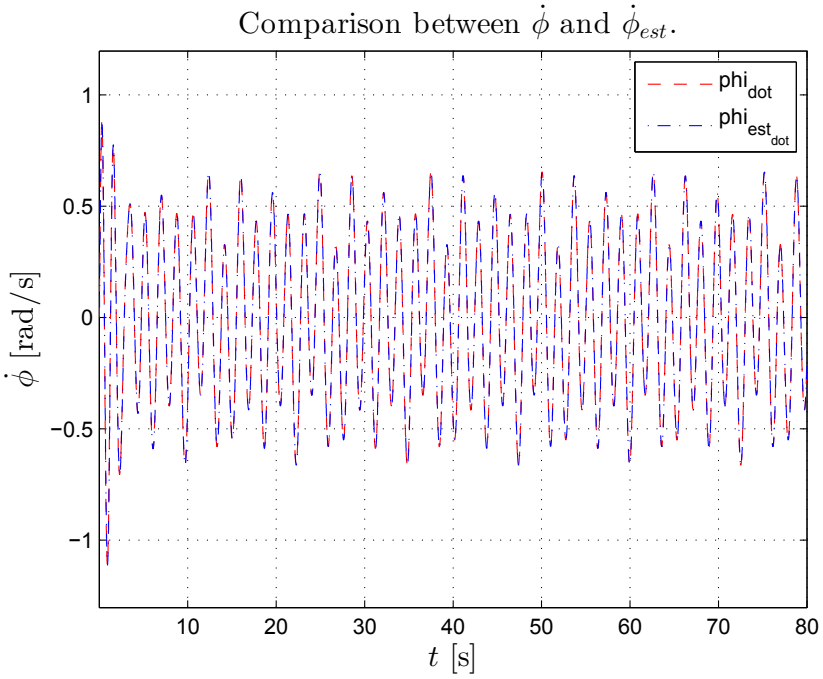

Figure 3.5: MATLAB plot displaying the velocity $\dot{\phi}$(t).

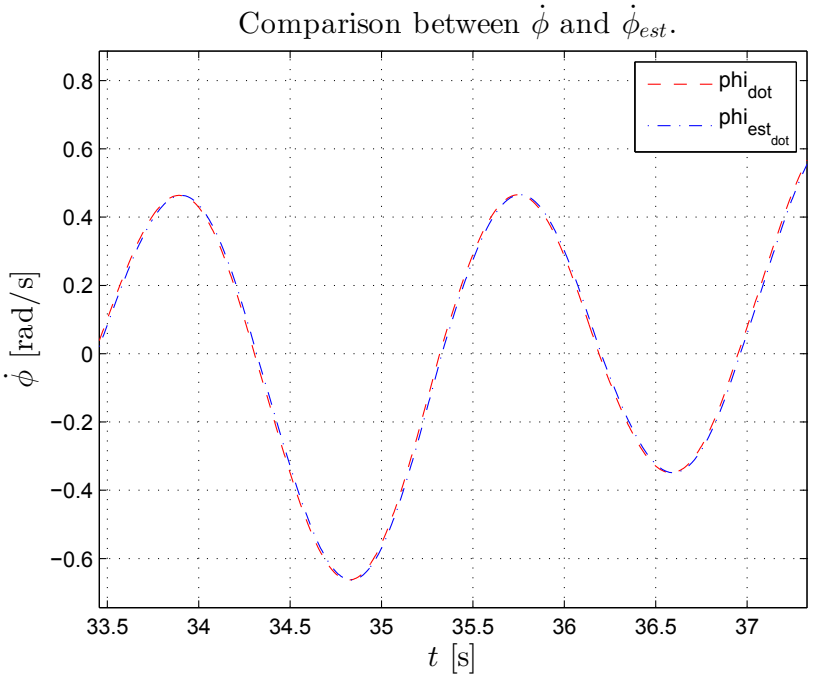

Figure 3.6: Detail from the MATLAB plot displaying the velocity $\dot{\phi}$(t).

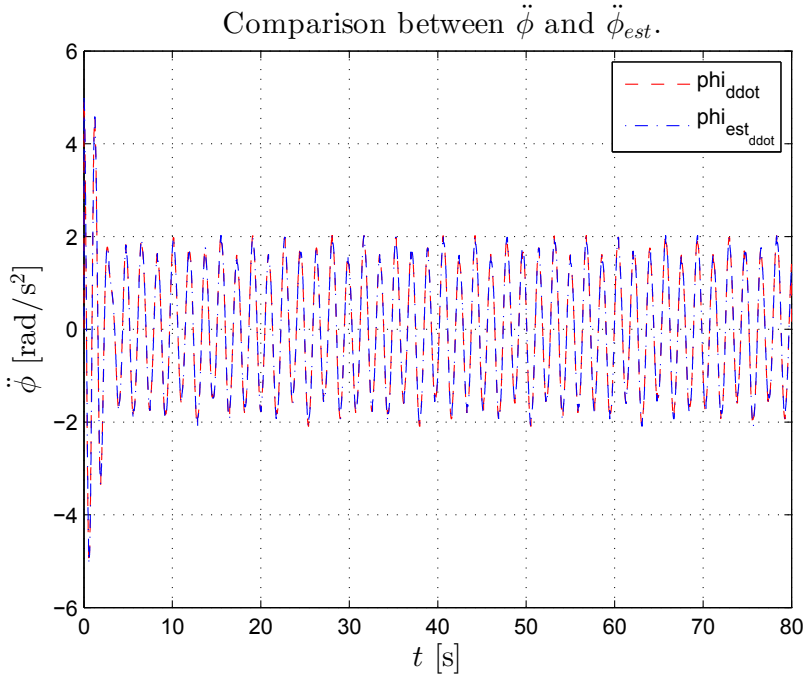

Figure 3.7: MATLAB plot displaying the acceleration $\ddot{\phi}$(t).

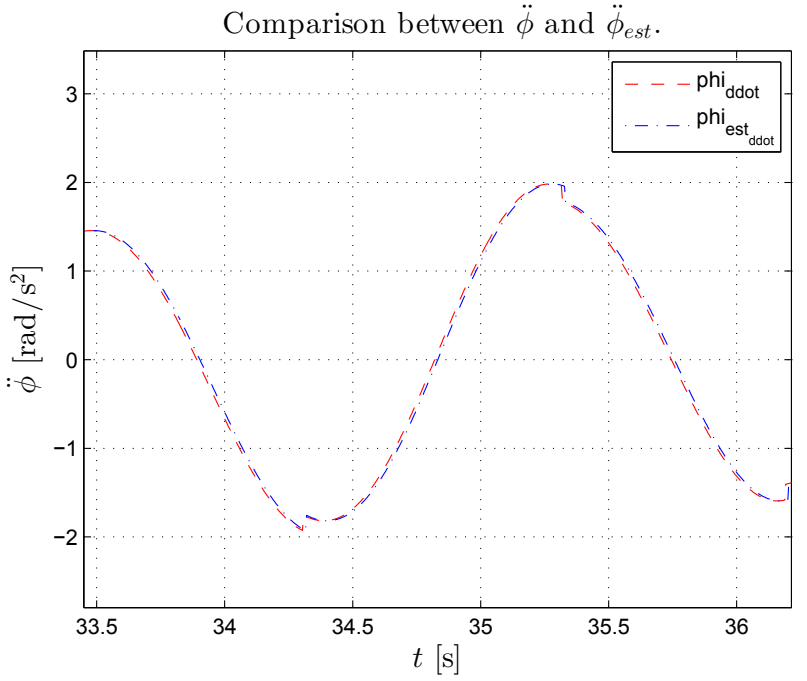

Figure 3.8: Detail from the MATLAB plot displaying the acceleration $\ddot{\phi}$(t).

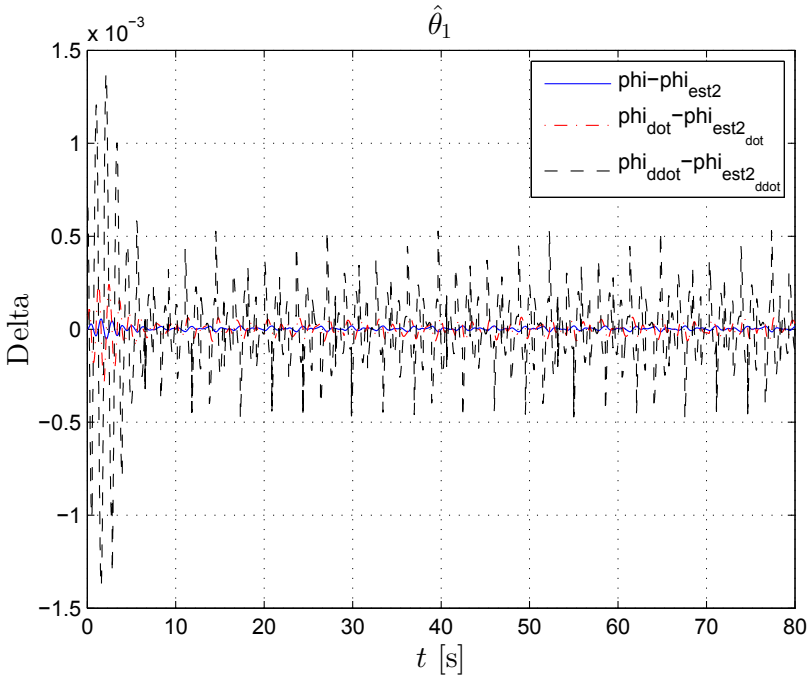

Figure 3.9: MATLAB plot displaying the error between the simulation and the verification simulation for $\hat{\boldsymbol{\theta}}_1$.

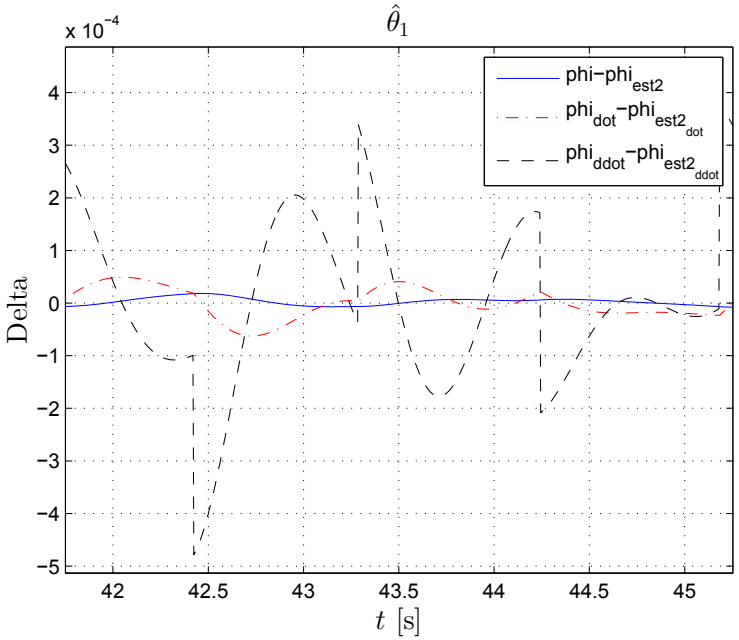

Figure 3.10: Detail from the MATLAB plot displaying the error between the simulation and the verification simulation for $\hat{\boldsymbol{\theta}}_1$.

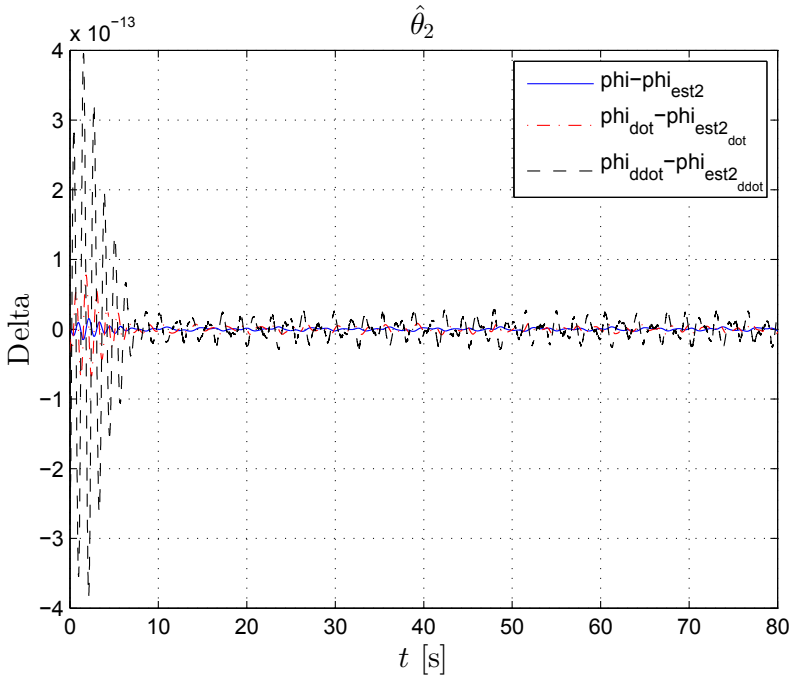

Figure 3.11: MATLAB plot displaying the error between simulation and verification simulation for $\hat{\boldsymbol{\theta}}_2$.

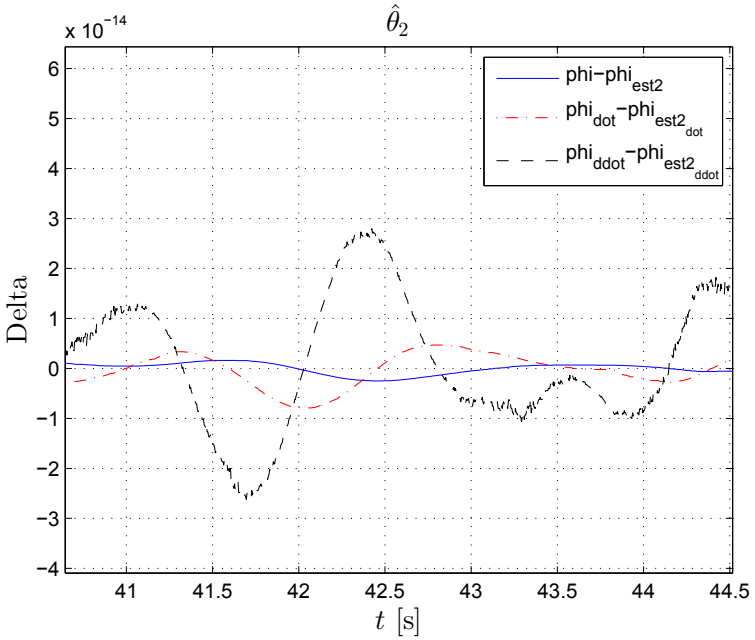

Figure 3.12: Detail from the MATLAB plot displaying the error between simulation and verification simulation for $\hat{\boldsymbol{\theta}}_2$.

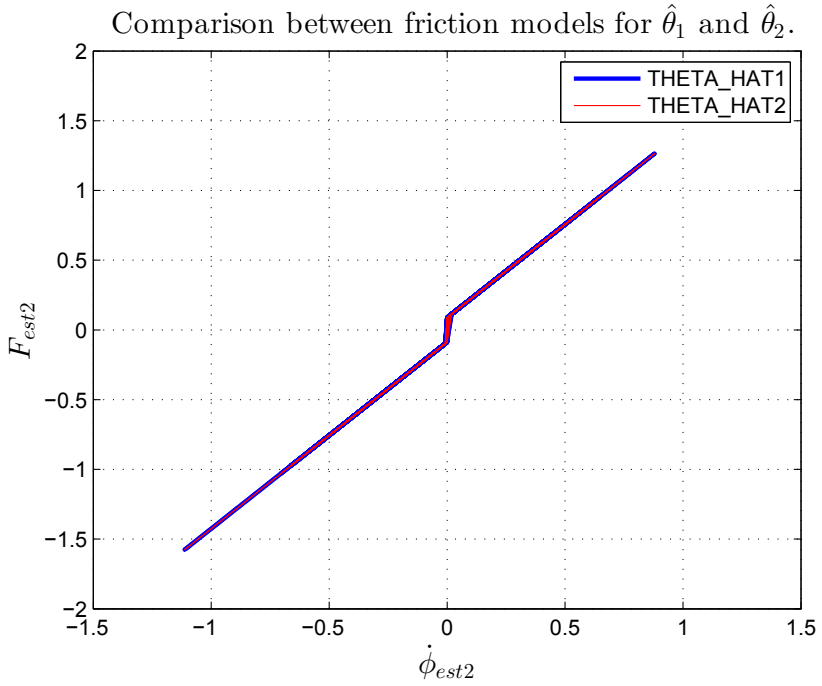

Figure 3.13: MATLAB plot displaying the friction models for $\hat{\boldsymbol{\theta}}_1$ and for $\hat{\boldsymbol{\theta}}_2$.

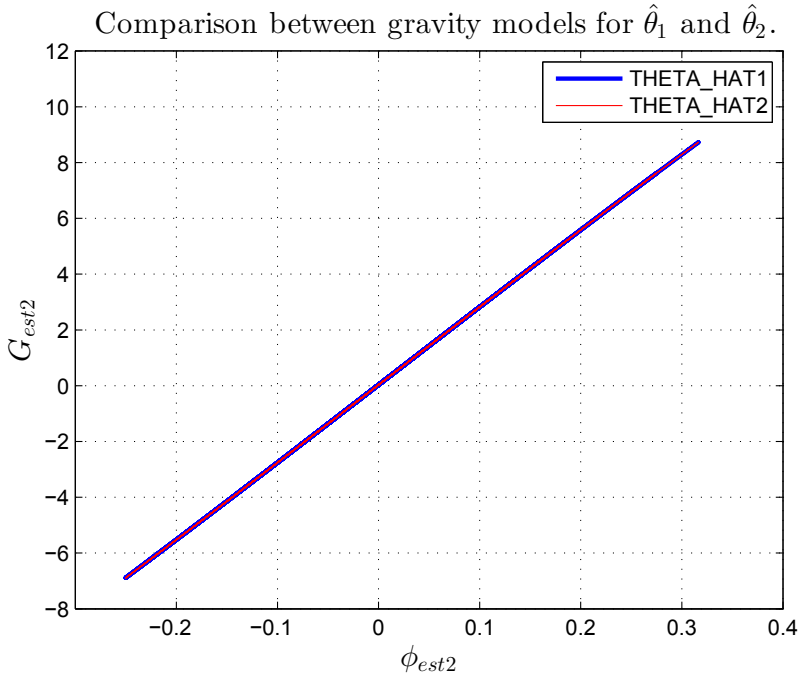

Figure 3.14: MATLAB plot displaying the gravity models for $\hat{\boldsymbol{\theta}}_1$ and for $\hat{\boldsymbol{\theta}}_2$.

When studying Figures 3.1 - 3.8 it can be seen that the simulated and the estimated models are very close to each other. This can be verified by looking at the two different estimates $\hat{\boldsymbol{\theta}}_1$ and $\hat{\boldsymbol{\theta}}_2$ in Tables 3.3 and 3.4, which have almost the same values. By comparing these estimates with the guesstimated values chosen for the model seen in Table 3.2, it can be seen that $\hat{\boldsymbol{\theta}}_2$ results in the same values as the guesstimates, while $\hat{\boldsymbol{\theta}}_1$ deviates only by a small amount (less than 0.25%). This may indicate that the system identification procedure for calculating $\hat{\boldsymbol{\theta}}_2$ achieves better estimates than the procedure for calculating $\hat{\boldsymbol{\theta}}_1$.

Since there are no noise present in the measurement for this estimation, it is not surprising that the variance of disturbance found in Tables 3.5 and 3.6 for the two estimates are very small.

In the error measurements for $\hat{\boldsymbol{\theta}}_1$ in Figures 3.9 and 3.10 it can be observed that $\phi - \phi_{est2}$, $\phi_{dot} - \phi_{est2_{dot}}$ and $\phi_{ddot} - \phi_{est2_{ddot}}$ have a 10 second transient period, after which the error is approximately $\pm 5 \cdot 10^{-4}$. For $\hat{\boldsymbol{\theta}}_2$ the error between the simulation and the verification simulation can be seen in Figures 3.11 and 3.12. Here it can be observed that $\phi - \phi_{est2}$, $\phi_{dot} - \phi_{est2_{dot}}$ and $\phi_{ddot} - \phi_{est2_{ddot}}$ also have a transient period, after which the error is approximately $\pm 3 \cdot 10^{-14}$. The error for $\hat{\boldsymbol{\theta}}_2$ is much smaller than for $\hat{\boldsymbol{\theta}}_1$.

The calculations for this simulation are computed using MATLAB. Hence small deviations between the simulation and the verification simulation can be caused by the numerical calculations in MATLAB. This will theoretically give small deviations between two equal calculations based on MATLAB's numerical accuracy.

In Figure 3.13 the friction models are shown for $\hat{\boldsymbol{\theta}}_1$ and $\hat{\boldsymbol{\theta}}_2$. This figure is created by plotting F_{est2} against $\dot{\phi}_{est2}$ for the whole time sequence for the verification simulation for each of the two estimates. Plotting the whole time sequence makes it easier to see if the friction force diverges. In the figure some irregularities can be seen around zero, this is probably caused by the way the figure is drawn in MATLAB. If the velocity crosses zero between two measurements, MATLAB will draw a diagonal line between these points, which will cause a mismatch between the plot in Figure 3.13 and the friction model in Equation (3.2). The gravity models for $\hat{\boldsymbol{\theta}}_1$ and $\hat{\boldsymbol{\theta}}_2$ are created by plotting G_{est2} against ϕ_{est2} for the whole time sequence for the verification simulation for each of the two estimates. This can be seen in Figure 3.14. It can be noticed that the two friction models and the two gravity models do not differ much from each other, which is reasonable since the difference between the two estimates are quite small.

3.3 System Identification

In the following sections the unknown parameters for the 6th joint of IRB 140, seen in Equations (3.6) - (3.10), are estimated using measurements, filtered with MATLAB. The MATLAB code and the measurements to be filtered can be found using the instructions seen in Appendix A. Table 3.7 shows the variable names used in the MATLAB code and in the figures containing plots created with MATLAB.

Variable	**Filtered Real Measurements**	**Estimation**	**Verification Simulation**
Position	ϕ	ϕ_{est}	ϕ_{est2}
Velocity	$\dot{\phi}$	$\dot{\phi}_{est}$	$\dot{\phi}_{est2}$
Acceleration	$\ddot{\phi}$	$\ddot{\phi}_{est}$	$\ddot{\phi}_{est2}$
Control input	u	u_{est}	u_{est2}

Table 3.7: Variable names used in MATLAB code and in figures containing plots from MATLAB.

The measurements were recorded from three different robot experiments with the 6th joint of IRB 140. For these experiments the reference was given by

$$q_6^d = a_i \sin(\omega_i t), \qquad i = 1, 2, 3 \tag{3.20}$$

By changing the values of a and ω in Equation (3.20) three different experiments were created. The values for these experiments can be found in Table 3.8.

a_1	$=$	$\frac{\pi}{2}$	ω_1	$=$	$\frac{3}{2}\pi$
a_2	$=$	$\frac{\pi}{2}$	ω_2	$=$	π
a_3	$=$	$\frac{\pi}{4}$	ω_3	$=$	π

Table 3.8: The amplitude and the frequency for the three different experiments.

For each of the three different experiments measurements of q_6, $\dot{q}_6$ and u_6 were recorded. q_6 is the measurement of the position of the 6th joint, $\dot{q}_6$ is the measurement of the velocity of the 6th joint, and u_6 is the measurement of the control input. The different measurements were filtered using higher order lowpass filters, to remove high frequency noise in the measurements. From the filtered joint velocity $\dot{q}_6$, the joint acceleration $\ddot{q}_6$ was obtained with a differential filter designed using qualified analysis of the absolute value of the calculated FFT. Filtered q_6, $\dot{q}_6$ and $\ddot{q}_6$ from Equations (3.12) - (3.17) are given as ϕ, $\dot{\phi}$ and $\ddot{\phi}$ respectively.

The cable tube containing all the cables for the gripper, is fastened with brackets outside the robot. This cable tube might induce noise in the measurements used to estimate the unknown parameters.

When moving the 6th joint of the robot this cable tube slides alongside the robot. The movement of this tube is affected by the start position of the gripper, the motion of the gripper and the placement of this cable tube which can be changed manually. The motion of this tube is not repeatable, which means that one can run the same program twice and get different movement of the tube. Since the movement of the tube will be different each time a robot program is run with the robot, this is seen as a source of noise in the measurements.

In Appendix A it is explained where to find the MATLAB code used for the different estimation experiments.

3.3.1 Time Step: 1 - 20 000

The filtered measurements were used as a whole to estimate the unknown parameters. The best estimates for the model were achieved with the second experiment, where the amplitude and frequency for the reference in Equation (3.20) were set to $a = \frac{\pi}{2}$ and $\omega = \pi$. Next the estimated parameters and the variance of disturbance for the second experiment are presented together with the error between the filtered measurements and the verification simulation.

The five unknown parameters were calculated using filtered measurements from the 6th joint of IRB 140. These estimates are collected in the vector $\hat{\boldsymbol{\theta}}_1$, and can be seen in Table 3.9.

An estimated model was created using ϕ and u from the filtered measurements. With this estimated model an alternative estimate called $\hat{\boldsymbol{\theta}}_2$ was computed. In Table 3.10 the estimate $\hat{\boldsymbol{\theta}}_2$ is presented.

Based on the estimated values the variance of the disturbance was calculated using Equation (3.19). In Tables 3.11 and 3.12 the variance of the disturbances for the two estimates are shown.

A new simulation was performed using the estimated values, this was done as a verification of the estimated values. The error between the filtered measurements and this simulation is presented in Figures 3.15 - 3.18.

At the end the friction and gravity models for the two different estimates are presented in Figures 3.19 - 3.21.

$\hat{k}_1$	=	0.0196
$\hat{k}_2$	=	−0.7649
$\hat{k}_3$	=	1.2545
$\hat{k}_4$	=	0.0002
$\hat{k}_u$	=	−0.1624

Table 3.9: $\hat{\boldsymbol{\theta}}_1$, estimate of unknown parameters.

$\hat{k}_1$	=	0.0561
$\hat{k}_2$	=	0.6106
$\hat{k}_3$	=	1.3446
$\hat{k}_4$	=	−0.0031
$\hat{k}_u$	=	0.1980

Table 3.10: $\hat{\boldsymbol{\theta}}_2$, estimate of unknown parameters.

$\hat{\sigma}_1$	=	3.3507

Table 3.11: The variance of the disturbance for $\hat{\boldsymbol{\theta}}_1$.

$\hat{\sigma}_2$	=	4.4794

Table 3.12: The variance of the disturbance for $\hat{\boldsymbol{\theta}}_2$.

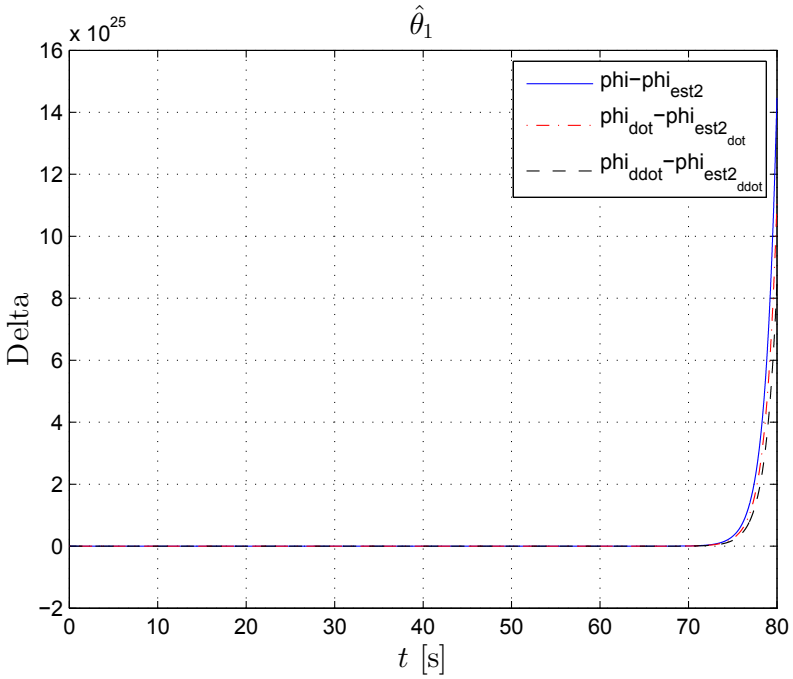

Figure 3.15: MATLAB plot displaying the error between the filtered measurements and the verification simulaton for $\hat{\boldsymbol{\theta}}_1$.

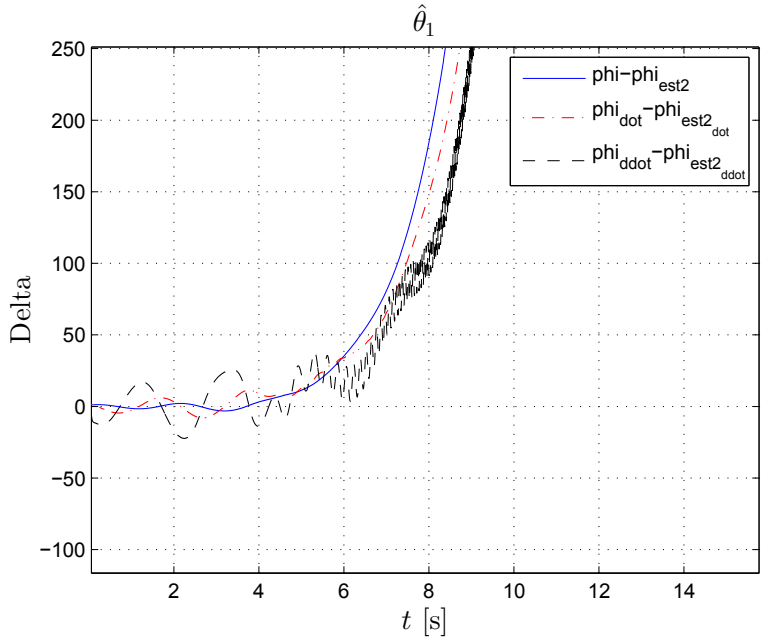

Figure 3.16: Detail from the MATLAB plot displaying the error between the filtered measurements and the verification simulation for $\hat{\boldsymbol{\theta}}_1$.

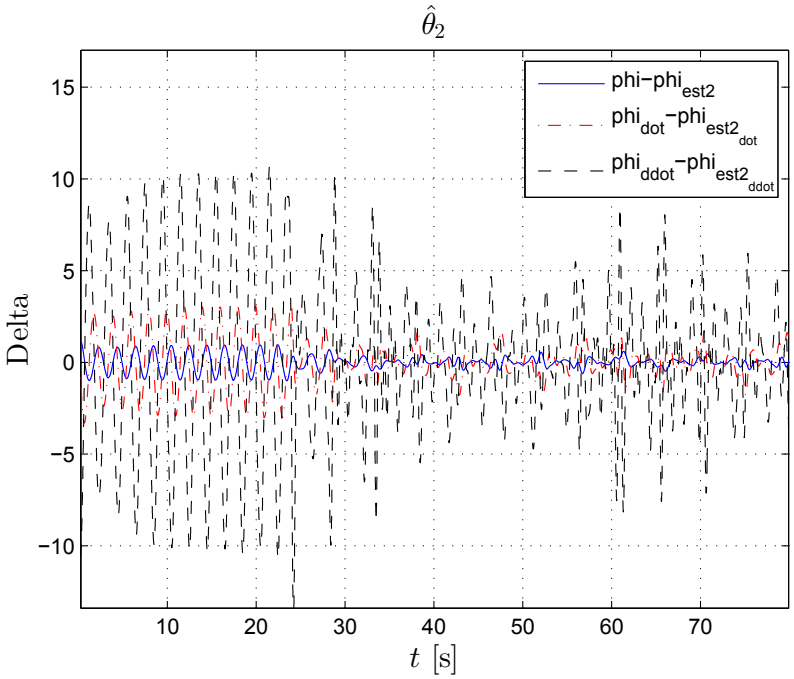

Figure 3.17: MATLAB plot displaying the error between the filtered measurements and simulated verification for $\hat{\boldsymbol{\theta}}_2$.

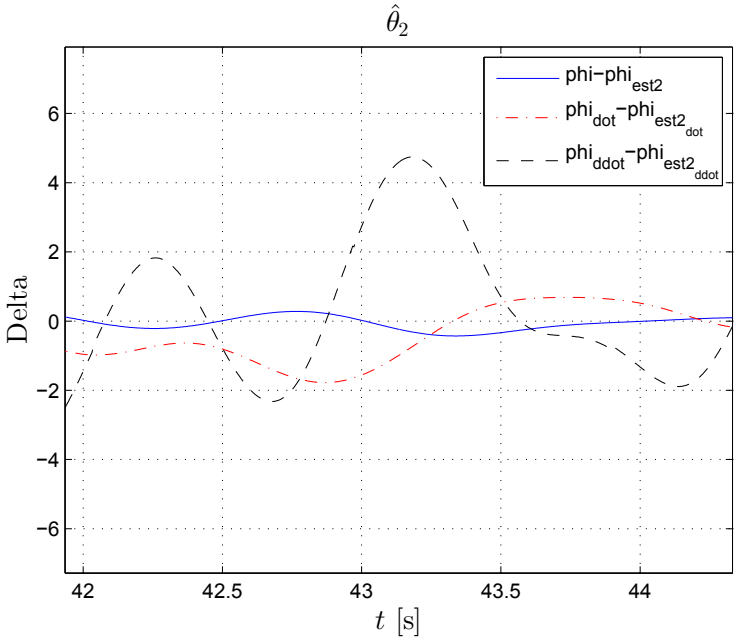

Figure 3.18: Detail from the MATLAB plot displaying the error between the filtered measurements and simulated verification for $\hat{\boldsymbol{\theta}}_2$.

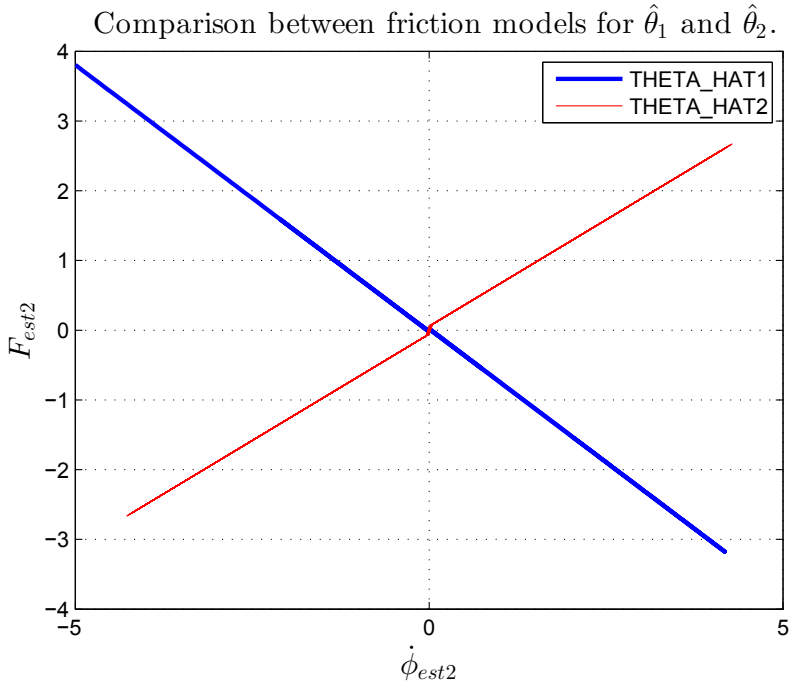

Figure 3.19: MATLAB plot displaying the friction models for $\hat{\boldsymbol{\theta}}_1$ and for $\hat{\boldsymbol{\theta}}_2$.

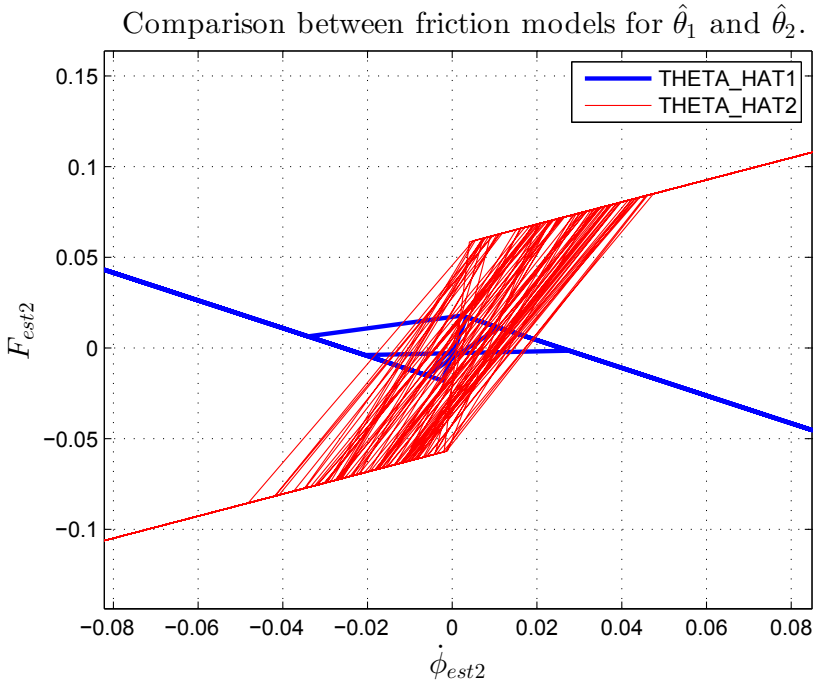

Figure 3.20: Detail from the MATLAB plot displaying the friction models for $\hat{\boldsymbol{\theta}}_1$ and for $\hat{\boldsymbol{\theta}}_2$.

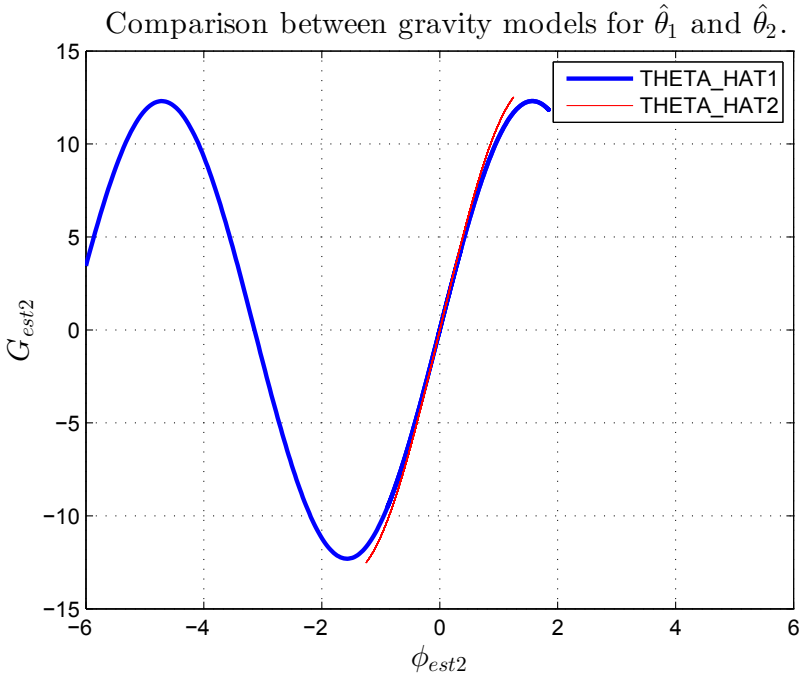

Figure 3.21: MATLAB plot displaying the gravity models for $\hat{\boldsymbol{\theta}}_1$ and for $\hat{\boldsymbol{\theta}}_2$.

When studying the two different estimates $\hat{\boldsymbol{\theta}}_1$ and $\hat{\boldsymbol{\theta}}_2$ in Tables 3.9 and 3.10 it can be seen that they differ from each other. This indicates that the estimated model is not exactly the same as the filtered measurements. If they were the same the two estimates $\hat{\boldsymbol{\theta}}_1$ and $\hat{\boldsymbol{\theta}}_2$ would be identical, which they are not.

In Tables 3.9 and 3.10 it can be seen that $\hat{\boldsymbol{\theta}}_1$ has negative values for $\hat{k}_2$ and $\hat{k}_u$ and that $\hat{\boldsymbol{\theta}}_2$ has a negative value for $\hat{k}_4$. All five parameters are assumed to be positive. When looking at Equation (3.11) it can be seen that the signs of $\hat{k}_2$ and $\hat{k}_u$ are more important than the signs of $\hat{k}_1$, $\hat{k}_3$ and $\hat{k}_4$, since $\hat{k}_1$, $\hat{k}_3$ and $\hat{k}_4$ are limited. If $\hat{k}_2$ is negative instead of positive the viscous friction will work with the motion instead of against, and if $\hat{k}_u$ is negative instead of positive the actuator force will work in the wrong direction.

In the error measurements for $\hat{\boldsymbol{\theta}}_1$ in Figures 3.15 and 3.16, it can be seen that the error between $\phi - \phi_{est2}$, $\dot{\phi} - \dot{\phi}_{est2}$ and $\ddot{\phi} - \ddot{\phi}_{est2}$ increases exponentially. This is probably caused by the negative values for $\hat{k}_2$ and $\hat{k}_u$.

When looking at the error between the filtered measurements and the verification simulation, for $\hat{\boldsymbol{\theta}}_2$ in Figures 3.17 and 3.18, it can be seen that $\phi - \phi_{est2}$ is almost zero, while $\dot{\phi} - \dot{\phi}_{est2}$ and $\ddot{\phi} - \ddot{\phi}_{est2}$ vary around zero. It can be observed that the error is periodical for the first 25 seconds, then the error pattern changes to be nonperiodic. This is probably caused by unmodeled nonlinearities.

In Figure 3.19 the friction models are shown for $\hat{\boldsymbol{\theta}}_1$ and $\hat{\boldsymbol{\theta}}_2$. This figure is created by plotting F_{est2} against $\dot{\phi}_{est2}$ for the whole time sequence for the verification simulation for each of the two estimates. Plotting the whole time sequence makes it easier to see if the friction force diverges. A mismatch between the friction model for $\hat{\boldsymbol{\theta}}_2$ and the friction model in Equation (3.2) can be seen in Figure 3.20. How this is created by MATLAB is explained in Section 3.2. In Figure 3.19 it can be seen that the friction force diverges for $\hat{\boldsymbol{\theta}}_1$. This might be caused by the same reason as for the exponential error already discovered in Figure 3.15. The friction model using $\hat{\boldsymbol{\theta}}_2$ shows a typical Coulomb friction combined with viscous friction, where the irregular behavior around zero velocity probably is caused by MATLAB as mentioned above.

The gravity models for $\hat{\boldsymbol{\theta}}_1$ and $\hat{\boldsymbol{\theta}}_2$ are created by plotting G_{est2} against ϕ_{est2} for the whole time sequence for the verification simulation for each of the two estimates. This can be seen in Figure 3.21. In this figure it can be noticed that both $\hat{\boldsymbol{\theta}}_1$ and $\hat{\boldsymbol{\theta}}_2$ result in a sinusoidal shaped form, but the $\hat{\boldsymbol{\theta}}_1$ case diverges in the leftmost direction. This could be caused by the negative values for $\hat{k}_2$ and $\hat{k}_u$.

Even though the variance of disturbance is lower for $\hat{\boldsymbol{\theta}}_1$ than for $\hat{\boldsymbol{\theta}}_2$, it is quite clear by looking at the figures that the estimated parameters in $\hat{\boldsymbol{\theta}}_2$ is a better match than the estimated parameters in $\hat{\boldsymbol{\theta}}_1$. When deciding what estimate to select, one cannot only look at the variance. It is also important to take into account the error between the measurements and the verification simulation for the different estimates.

The calculations for this estimation are computed using MATLAB. Hence the numerical accuracy explained in Section 3.2 applies here too. It is also possible that the model used with the system identification method is wrong. The friction model is assumed to be Coulomb friction combined with viscous friction, which is a static model. This is one of the simplest models for friction. Since the IRB 140 is a complicated device it is sensible to assume that the actual friction model is more complicated than anticipated.

Since the model used for the system identification is quite simple, it was decided to only use the first 25 seconds of measurements; apparently less influenced by unmodeled nonlinear effects. It is believed that this might give better estimates.

3.3.2 Time Step: 11 - 4 874

Because of the simple nature of the system identification model it was decided to only use the first 25 seconds of the filtered measurements for three new estimation experiments. The first 10 measurements were also omitted from the experiments, just to have another start position than the previous experiments. The selected segment was therefore the one between $N\_start = 11$ and $N\_stop = 4874$.

For each of the three experiments, $\hat{\boldsymbol{\theta}}_1$ and $\hat{\boldsymbol{\theta}}_2$ were tested with a simulation. Then the error between the simulation and the filtered measurements were calculated. These simulations were performed to get an idea of how these estimates behaved for the whole time sequence, since only the first 25 seconds were tested during the estimation experiments.

To give an indication about the noise level, the variance of disturbance was calculated too.

When it is written that the whole time sequence is used, all the measurements between $N\_start = 1$ and $N\_stop = 20000$ are used, and when it is written that the segment of the time sequence is used, the measurements between $N\_start = 11$ and $N\_stop = 4874$ are used. The estimation experiments are computed using the segment of the time sequence while the simulation using the whole time sequence and the figures showing friction and gravity usually uses the whole time sequence. This is done to give an idea of how these estimates will perform if used past the first 25 seconds.

3.3.2.1 Estimation using measurements from the first experiment

For this case the amplitude and frequency for the reference in Equation (3.20) were set to $a = \frac{\pi}{2}$ and $\omega = \frac{3}{2}\pi$.

The five unknown parameters were calculated using filtered measurements from the 6th joint of IRB 140. These estimates are collected in the vector $\hat{\boldsymbol{\theta}}_1$, and can be seen in Table 3.13.

An estimated model was created using ϕ and u from the filtered measurements. With this estimated model an alternative estimate called $\hat{\boldsymbol{\theta}}_2$ was computed. In Table 3.14 the estimate $\hat{\boldsymbol{\theta}}_2$ is presented.

Based on $\hat{\boldsymbol{\theta}}_1$ and $\hat{\boldsymbol{\theta}}_2$ the variance of the disturbances, found in Equation (3.19), were calculated using the filtered measurements. In Tables 3.15 - 3.18 the variance of the disturbances for the two estimates are shown.

A new simulation was performed using the estimated values, this was done as a verification of the estimated values. The error between the filtered measurements and this simulation is presented in Figures 3.22 - 3.25. Then a simulation using the whole time sequence was performed, and the error between the simulation and the filtered measurements is shown in Figures 3.26 - 3.29.

At the end the friction and gravity models for the two different estimates are presented in Figures 3.30 and 3.31.

$\hat{k}_1$	=	0.0513
$\hat{k}_2$	=	13.5641
$\hat{k}_3$	=	1.0338
$\hat{k}_4$	=	−0.0017
$\hat{k}_u$	=	6.0657

Table 3.13: $\hat{\boldsymbol{\theta}}_1$, estimate of unknown parameters.

$\hat{k}_1$	=	−0.0457
$\hat{k}_2$	=	12.9797
$\hat{k}_3$	=	1.3750
$\hat{k}_4$	=	−0.0910
$\hat{k}_u$	=	5.5883

Table 3.14: $\hat{\boldsymbol{\theta}}_2$, estimate of unknown parameters.

$\hat{\sigma}_{1a}$	=	42.2473

Table 3.15: $\hat{\sigma}_{1a}$, estimated variance of the disturbance for $\hat{\boldsymbol{\theta}}_1$ using filtered measurements, time step: 1 - 20 000.

$\hat{\sigma}_{2a}$	=	48.9239

Table 3.16: $\hat{\sigma}_{2a}$, estimated variance of the disturbance for $\hat{\boldsymbol{\theta}}_2$ using filtered measurements, time step: 1 - 20 000.

$\hat{\sigma}_{1b}$	=	0.7305

Table 3.17: $\hat{\sigma}_{1b}$, estimated variance of the disturbance for $\hat{\boldsymbol{\theta}}_1$ using filtered measurements, time step: 11 - 4 874.

$\hat{\sigma}_{2b}$	=	7.5723

Table 3.18: $\hat{\sigma}_{2b}$, estimated variance of the disturbance for $\hat{\boldsymbol{\theta}}_2$ using filtered measurements, time step: 11 - 4 874.

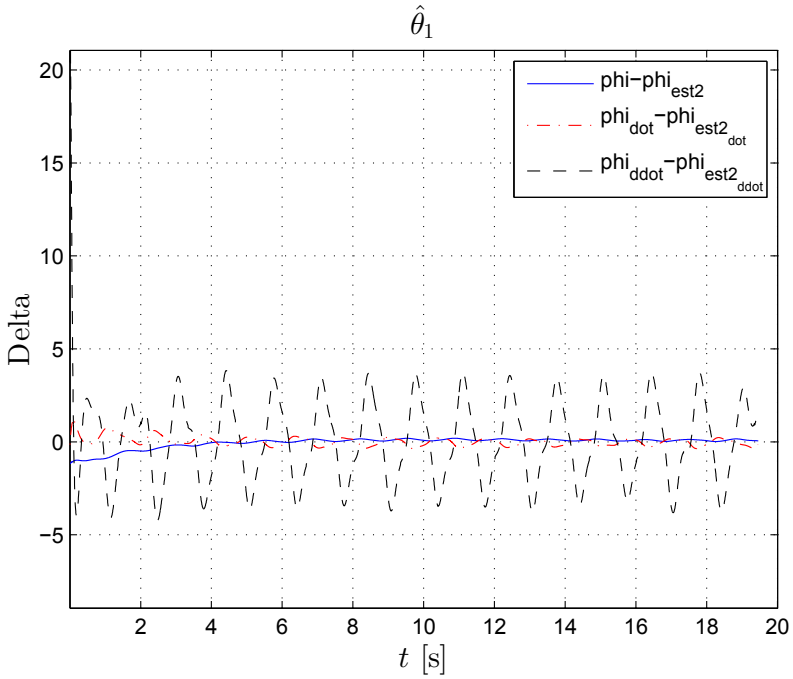

Figure 3.22: MATLAB plot displaying the error between the filtered measurements and the verification simulation for $\hat{\boldsymbol{\theta}}_1$.

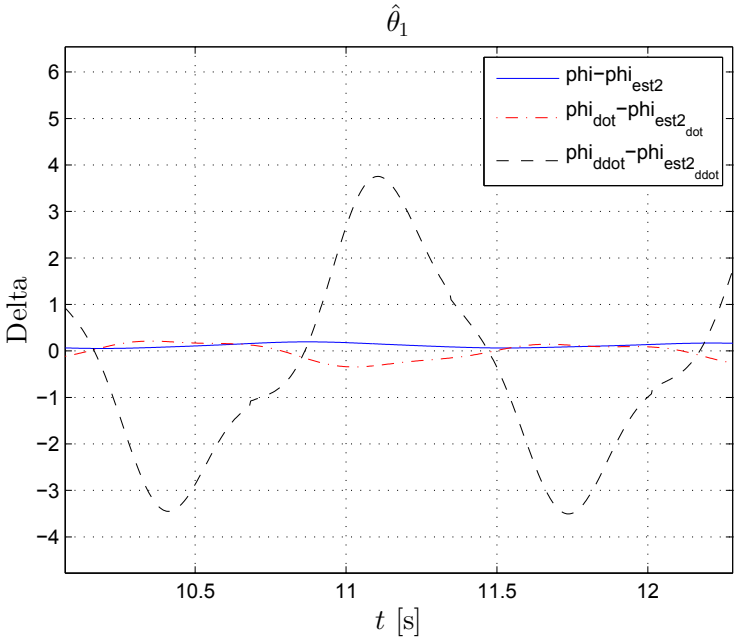

Figure 3.23: Detail from the MATLAB plot displaying the error between the filtered measurements and the verification simulation for $\hat{\boldsymbol{\theta}}_1$.

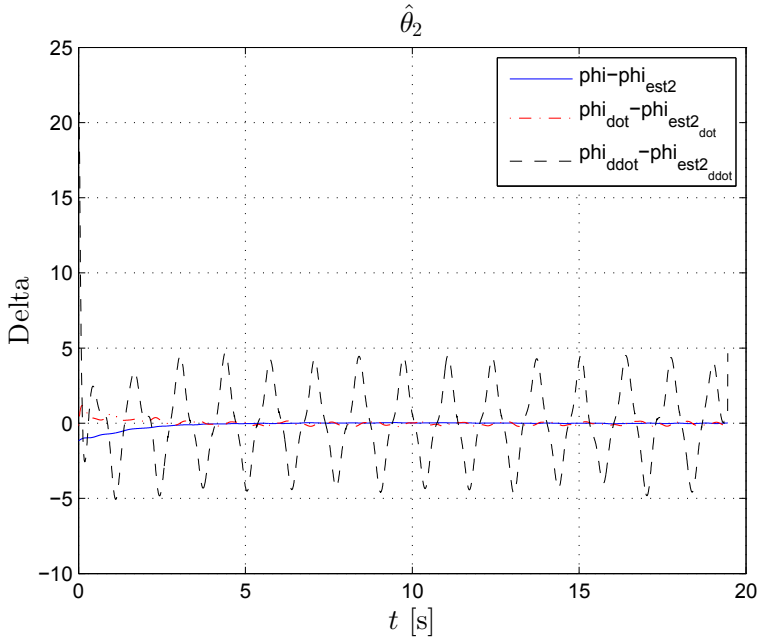

Figure 3.24: MATLAB plot displaying the error between the filtered measurements and the verification simulation for $\hat{\boldsymbol{\theta}}_2$.

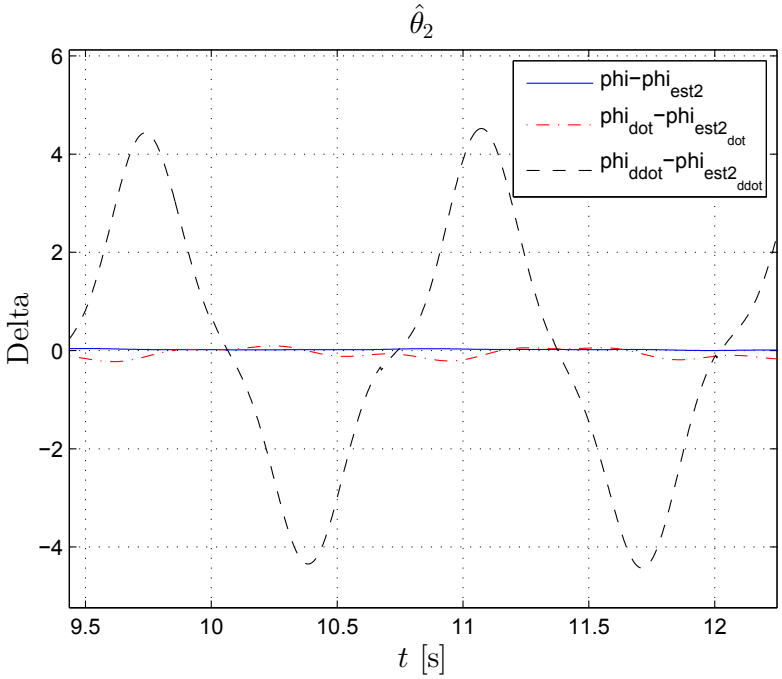

Figure 3.25: Detail from the MATLAB plot displaying the error between the filtered measurements and the verification simulation for $\hat{\boldsymbol{\theta}}_2$.

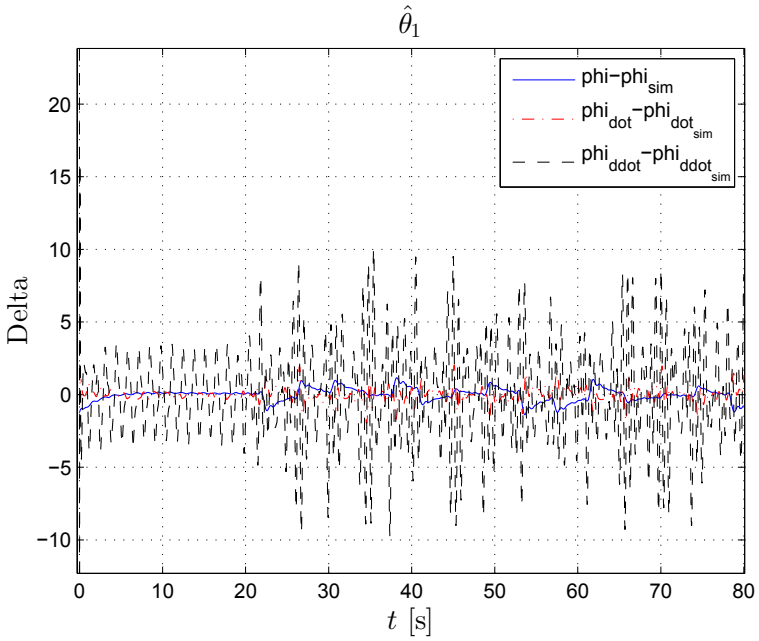

Figure 3.26: MATLAB plot displaying the error between the filtered measurements and the verification simulation for the whole time sequence.

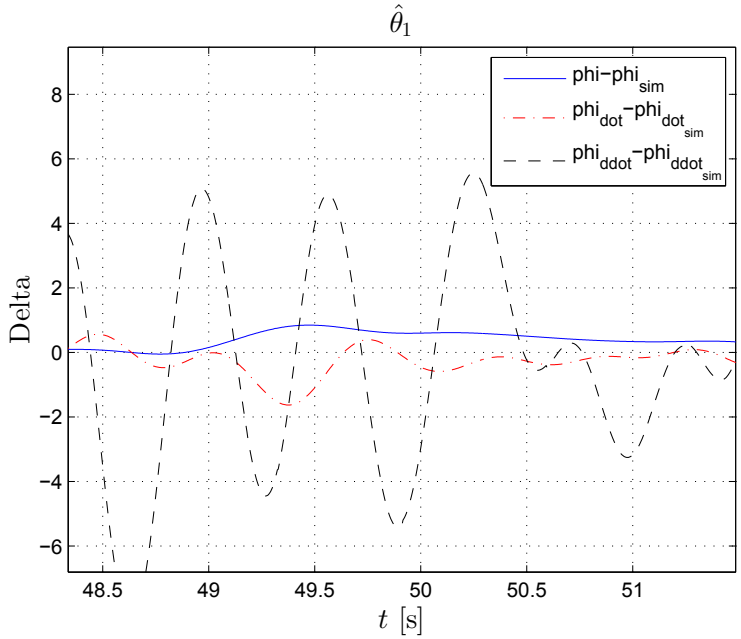

Figure 3.27: Detail from the MATLAB plot displaying the error between the filtered measurements and the verification simulation for the whole time sequence.

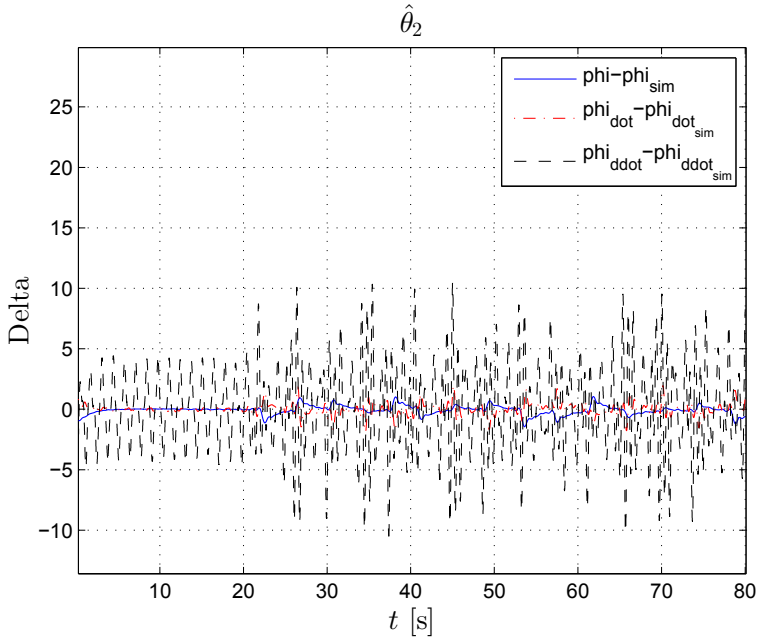

Figure 3.28: MATLAB plot displaying the error between the filtered measurements and the verification simulation for the whole time sequence.

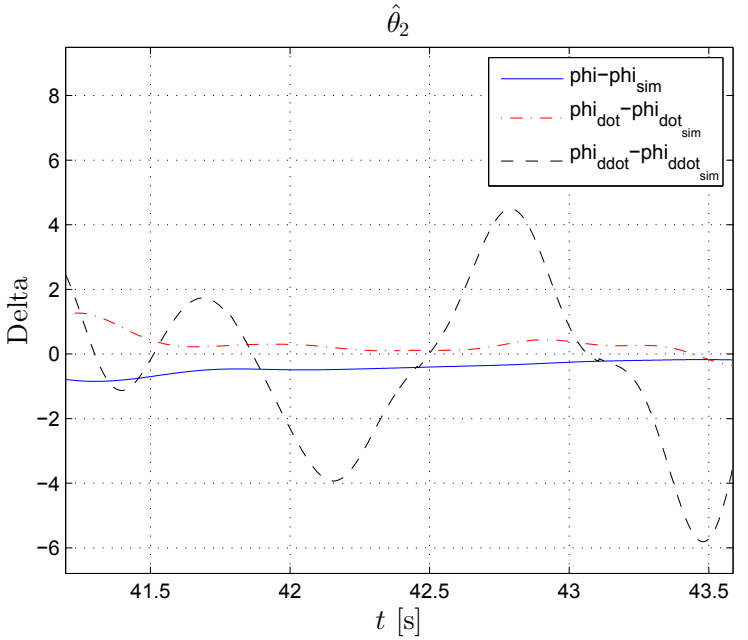

Figure 3.29: Detail from the MATLAB plot displaying the error between the filtered measurements and the verification simulation for the whole time sequence.

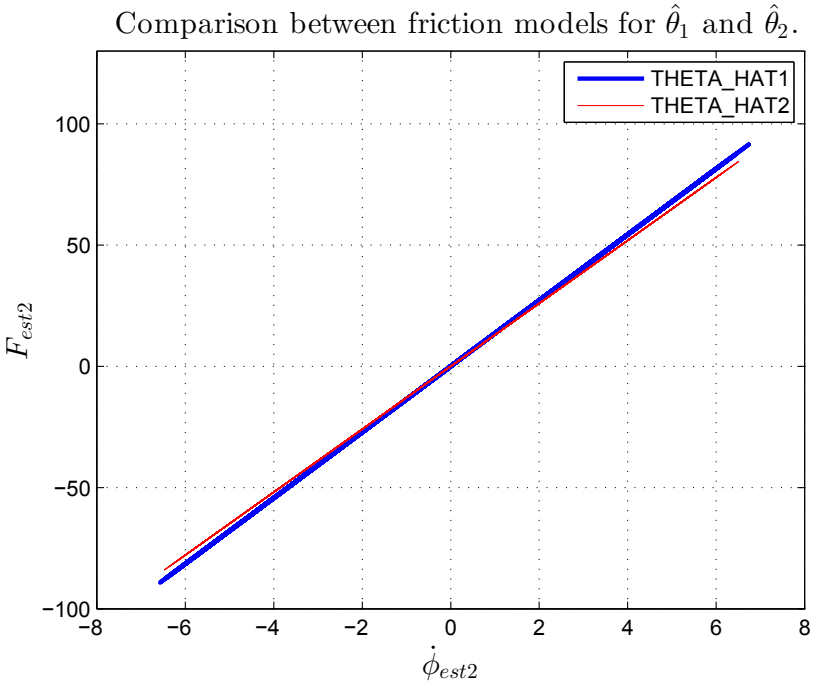

Figure 3.30: MATLAB plot displaying the friction models for $\hat{\boldsymbol{\theta}}_1$ and for $\hat{\boldsymbol{\theta}}_2$.

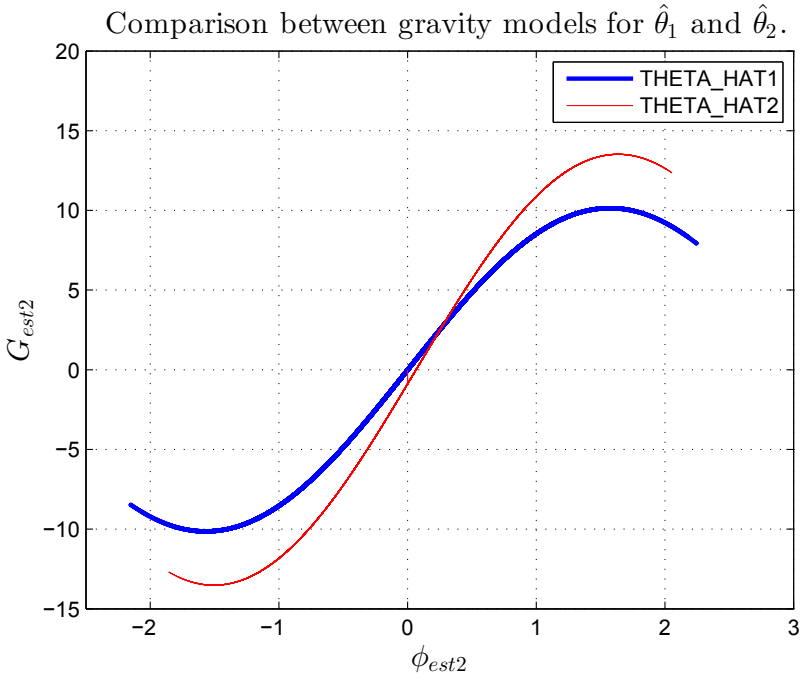

Figure 3.31: MATLAB plot displaying the gravity models for $\hat{\boldsymbol{\theta}}_1$ and for $\hat{\boldsymbol{\theta}}_2$.

When studying the two different estimates $\hat{\boldsymbol{\theta}}_1$ and $\hat{\boldsymbol{\theta}}_2$ in Tables 3.13 and 3.14, it can be seen that they differ from each other. This indicates that the estimated model is not exactly the same as the filtered measurements. If they were the same the two estimates $\hat{\boldsymbol{\theta}}_1$ and $\hat{\boldsymbol{\theta}}_2$ would be identical, which they are not.

In Tables 3.13 and 3.14 it can be seen that $\hat{\boldsymbol{\theta}}_1$ has a negative value for $\hat{k}_4$ and that $\hat{\boldsymbol{\theta}}_2$ has negative values for $\hat{k}_1$ and $\hat{k}_4$. All five parameters are assumed to be positive. When looking at Equation (3.11) it can be seen that the signs of $\hat{k}_2$ and $\hat{k}_u$ are more important than the signs of $\hat{k}_1$, $\hat{k}_3$ and $\hat{k}_4$, since $\hat{k}_1$, $\hat{k}_3$ and $\hat{k}_4$ are limited.

In Figures 3.22 - 3.25 the error between the filtered measurements and the verification simulation can be seen. It is difficult to see the difference between the error created by using $\hat{\boldsymbol{\theta}}_1$ and $\hat{\boldsymbol{\theta}}_2$. By a closer look it can be seen that the error between $\phi - \phi_{est2}$ and $\dot{\phi} - \dot{\phi}_{est2}$ for $\hat{\boldsymbol{\theta}}_2$ is a bit smaller than for $\hat{\boldsymbol{\theta}}_1$, but the error between $\ddot{\phi} - \ddot{\phi}_{est2}$ is a bit smaller for $\hat{\boldsymbol{\theta}}_1$ than $\hat{\boldsymbol{\theta}}_2$. The error for $\phi - \phi_{est2}$ and $\dot{\phi} - \dot{\phi}_{est2}$ converges to zero for both cases, and $\ddot{\phi} - \ddot{\phi}_{est2}$ oscillates around zero with a higher amplitude.

When looking at the estimated variance of disturbance in Tables 3.15 - 3.18 it can be seen that the estimated variance of disturbance for the first 25 seconds is small, and the estimated variance of disturbance for the whole time sequence is 6 to 58 times larger. For both of the time segments, σ_1 gives the smallest values.

For the simulation of the whole time sequence it can be seen that the error after 25 seconds is larger than the error before. This applies for both of the estimates. As mentioned above, the error before 25 seconds converges to zero for $\phi - \phi_{est2}$ and $\dot{\phi} - \dot{\phi}_{est2}$, but after 25 seconds the error is non-periodic with a higher amplitude. For both estimates $\hat{\boldsymbol{\theta}}_1$ and $\hat{\boldsymbol{\theta}}_2$ the error is varying around zero for $\phi - \phi_{sim}$, $\dot{\phi} - \dot{\phi}_{sim}$ and $\ddot{\phi} - \ddot{\phi}_{sim}$.

In Figure 3.30 the friction models are shown for $\hat{\boldsymbol{\theta}}_1$ and $\hat{\boldsymbol{\theta}}_2$. This figure is created by plotting F_{est2} against $\dot{\phi}_{est2}$ for the whole time sequence for the verification simulation for each of the two estimates. Plotting the whole time sequence makes it easier to see if the friction force diverges. It can be seen that the difference between the estimated friction for the two estimates is small. $\hat{k}_1$ is almost zero for both cases and hence the Coulomb friction is almost non-existing. The friction force is therefore dominated by the viscous friction, given by k_2. In the figure some irregularities can be seen around zero. It is explained in Section 3.2 how these are created by MATLAB. Here the Coulomb friction is almost zero, and the zero crossing error does not manifest itself so clearly as for cases where the Coulomb friction is larger.

The gravity models for $\hat{\boldsymbol{\theta}}_1$ and $\hat{\boldsymbol{\theta}}_2$ are created by plotting G_{est2} against ϕ_{est2} for the whole time sequence for the verification simulation for each of the two estimates. This can be seen in Figure 3.31. In this figure it can be noticed that both $\hat{\boldsymbol{\theta}}_1$ and $\hat{\boldsymbol{\theta}}_2$ result in a sinusoidal shaped form.

The calculations for this estimation are computed using MATLAB. Hence the numerical accuracy explained in Section 3.2 applies here too. It is also possible that the model used with the system identification method is wrong. The friction model is assumed to be Coulomb friction combined with viscous friction, which is a static model. This is one of the simplest models for friction. Since the IRB 140 is a complicated device it is sensible to assume that the actual friction model is more complicated than anticipated.

3.3.2.2 Estimation using measurements from the second experiment

For this case the amplitude and frequency for the reference in Equation (3.20) were set to $a = \frac{\pi}{2}$ and $\omega = \pi$.

The five unknown parameters were calculated using filtered measurements from the 6th joint of IRB 140. These estimates are collected in the vector $\hat{\boldsymbol{\theta}}_1$, and can be seen in Table 3.19.

An estimated model was created using ϕ and u from the filtered measurements. With this estimated model an alternative estimate called $\hat{\boldsymbol{\theta}}_2$ was computed. In Table 3.20 the estimate $\hat{\boldsymbol{\theta}}_2$ is presented.

Based on $\hat{\boldsymbol{\theta}}_1$ and $\hat{\boldsymbol{\theta}}_2$ the variance of the disturbances, found in Equation (3.19), were calculated using the filtered measurements. In Tables 3.21 - 3.24 the variance of the disturbances for the two estimates are shown.

A new simulation was performed using the estimated values, this was done as a verification of the estimated values. The error between the filtered measurements and this simulation is presented in Figures 3.32 - 3.35. Then a simulation using the whole time sequence was performed, and the error between this simulation and the filtered measurements is shown in Figures 3.36 - 3.39.

At the end the friction and gravity models for the two different estimates are presented in Figures 3.40 and 3.41.

$\hat{k}_1$	=	0.0115
$\hat{k}_2$	=	3.7190
$\hat{k}_3$	=	1.1298
$\hat{k}_4$	=	0.0048
$\hat{k}_u$	=	1.2382

Table 3.19: $\hat{\boldsymbol{\theta}}_1$, estimate of unknown parameters.

$\hat{k}_1$	=	−0.0221
$\hat{k}_2$	=	2.2875
$\hat{k}_3$	=	1.2034
$\hat{k}_4$	=	0.0166
$\hat{k}_u$	=	0.7075

Table 3.20: $\hat{\boldsymbol{\theta}}_2$, estimate of unknown parameters.

$\hat{\sigma}_{1a}$	=	4.1284

Table 3.21: $\hat{\sigma}_{1a}$, estimated variance of the disturbance for $\hat{\boldsymbol{\theta}}_1$ using filtered measurements, time step: 1 - 20 000.

$\hat{\sigma}_{2a}$	=	4.2640

Table 3.22: $\hat{\sigma}_{2a}$, estimated variance of the disturbance for $\hat{\boldsymbol{\theta}}_2$ using filtered measurements, time step: 1 - 20 000.

$\hat{\sigma}_{1b}$	=	0.3765

Table 3.23: $\hat{\sigma}_{1b}$, estimated variance of the disturbance for $\hat{\boldsymbol{\theta}}_1$ using filtered measurements, time step: 11 - 4 874.

$\hat{\sigma}_{2b}$	=	0.9690

Table 3.24: $\hat{\sigma}_{2b}$, estimated variance of the disturbance for $\hat{\boldsymbol{\theta}}_2$ using filtered measurements, time step: 11 - 4 874.

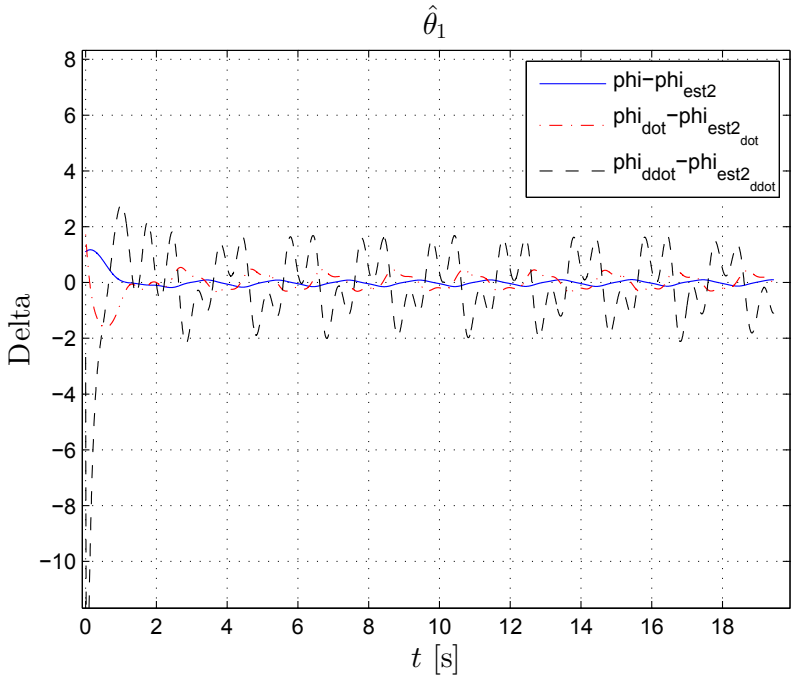

Figure 3.32: MATLAB plot displaying the error between the filtered measurements and the verification simulation for $\hat{\boldsymbol{\theta}}_1$.

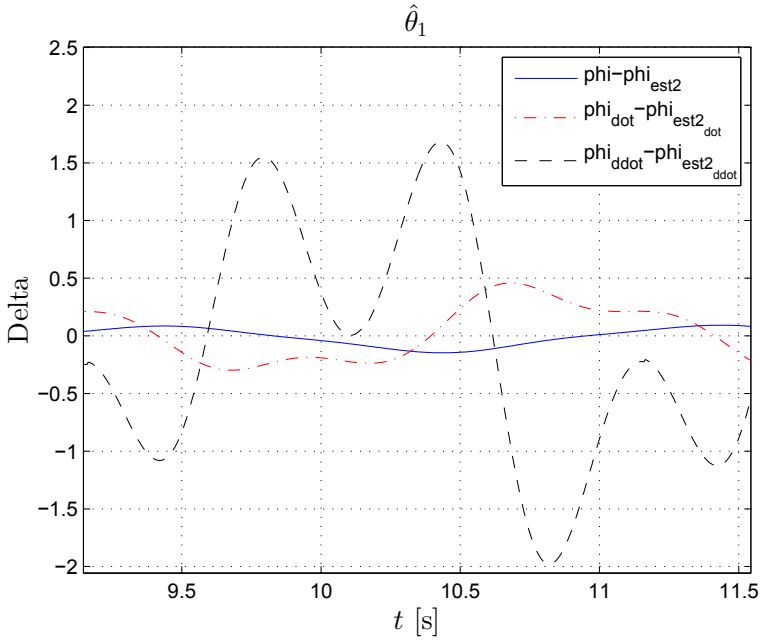

Figure 3.33: Detail from the MATLAB plot displaying the error between the filtered measurements and the verification simulation for $\hat{\boldsymbol{\theta}}_1$.

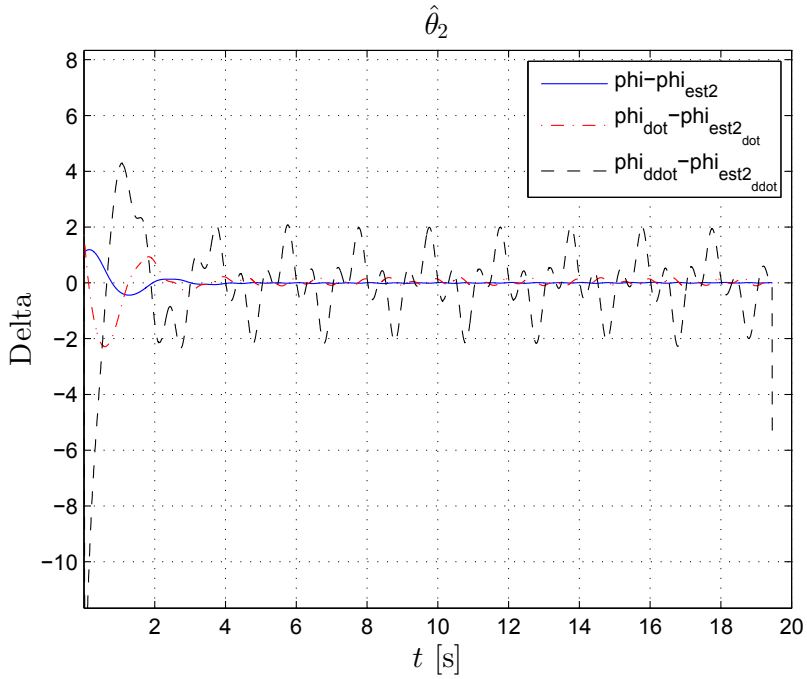

Figure 3.34: MATLAB plot displaying the error between the filtered measurements and the verification simulation for $\hat{\boldsymbol{\theta}}_2$.

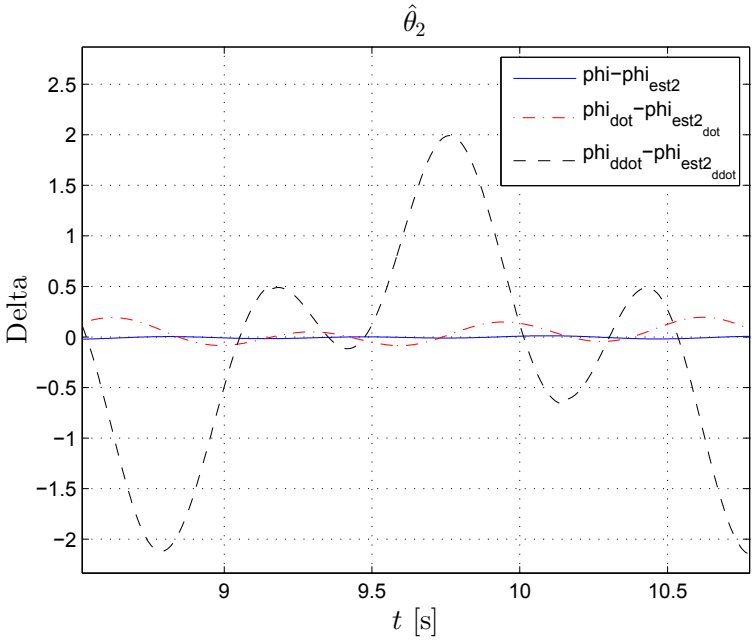

Figure 3.35: Detail from the MATLAB plot displaying the error between the filtered measurements and the verification simulation for $\hat{\boldsymbol{\theta}}_2$.

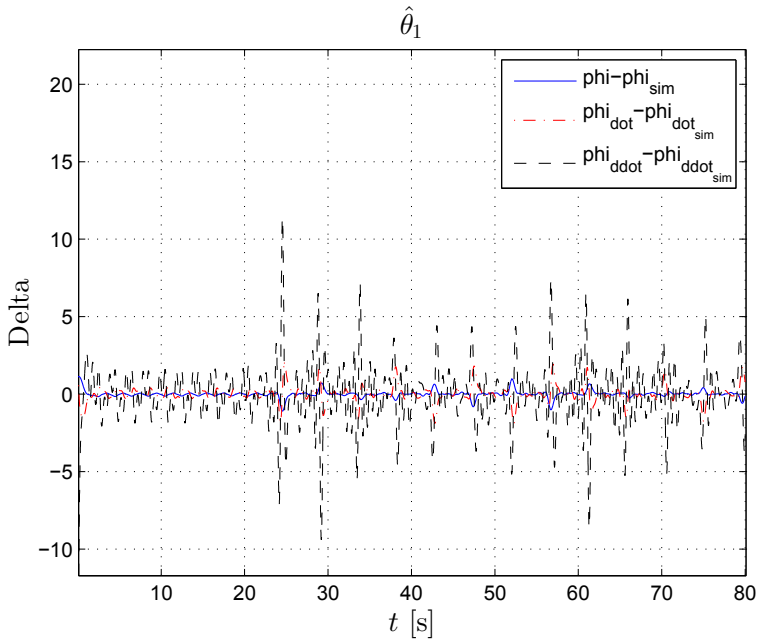

Figure 3.36: MATLAB plot displaying the error between the filtered measurements and the verification simulation for the whole time sequence.

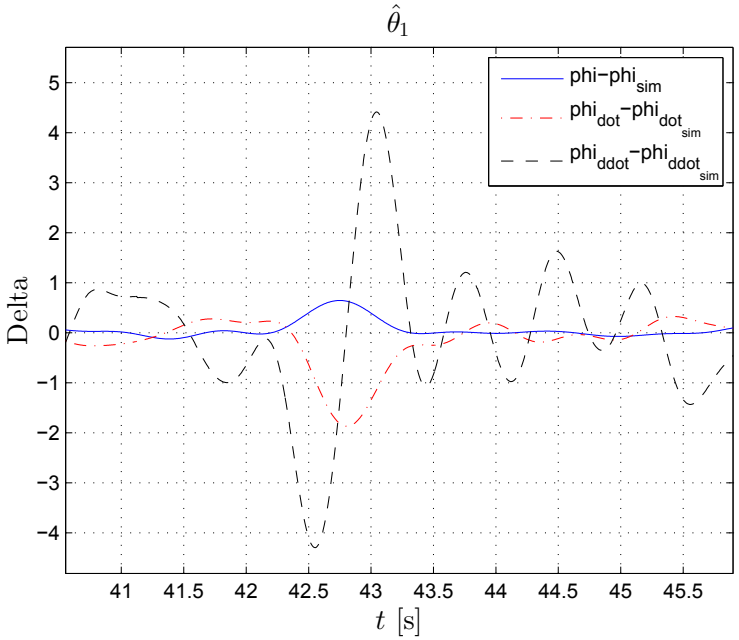

Figure 3.37: Detail from the MATLAB plot displaying the error between the filtered measurements and the verification simulation for the whole time sequence.

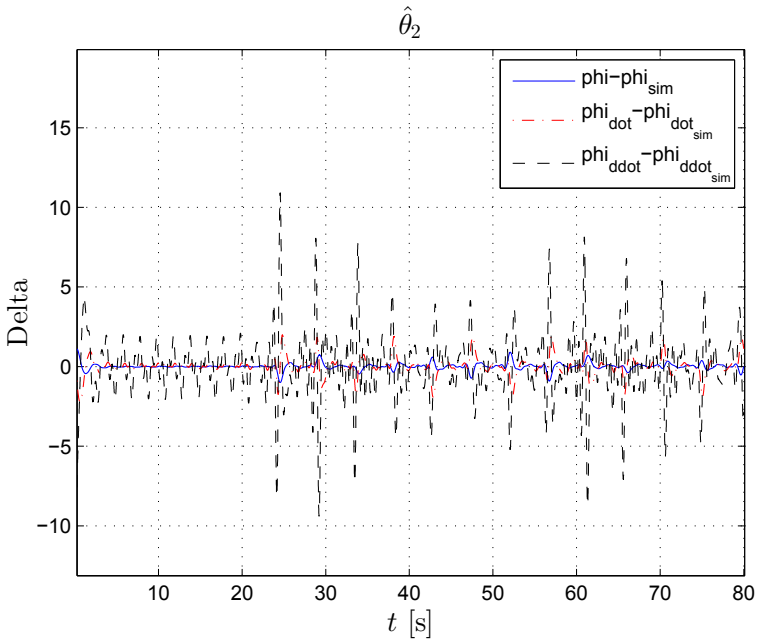

Figure 3.38: MATLAB plot displaying the error between the filtered measurements and the verification simulation for the whole time sequence.

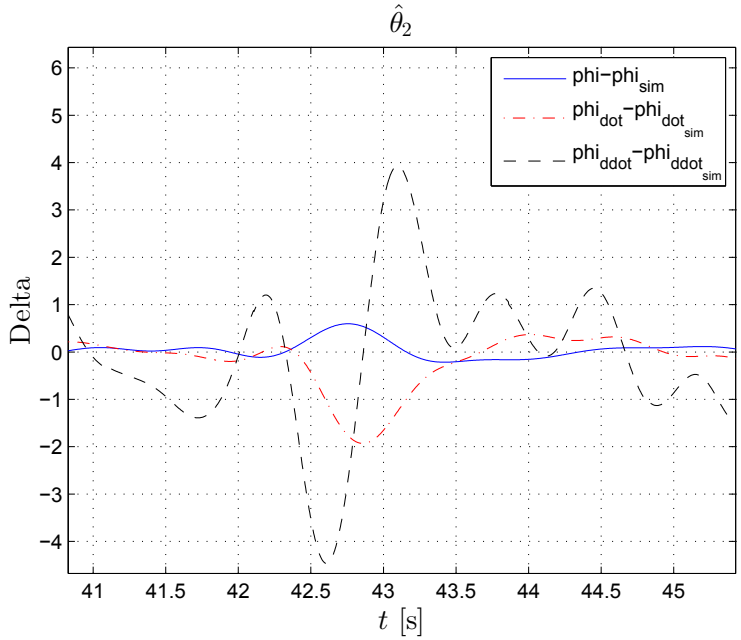

Figure 3.39: Detail from the MATLAB plot displaying the error the between filtered measurements and the verification simulation for the whole time sequence.

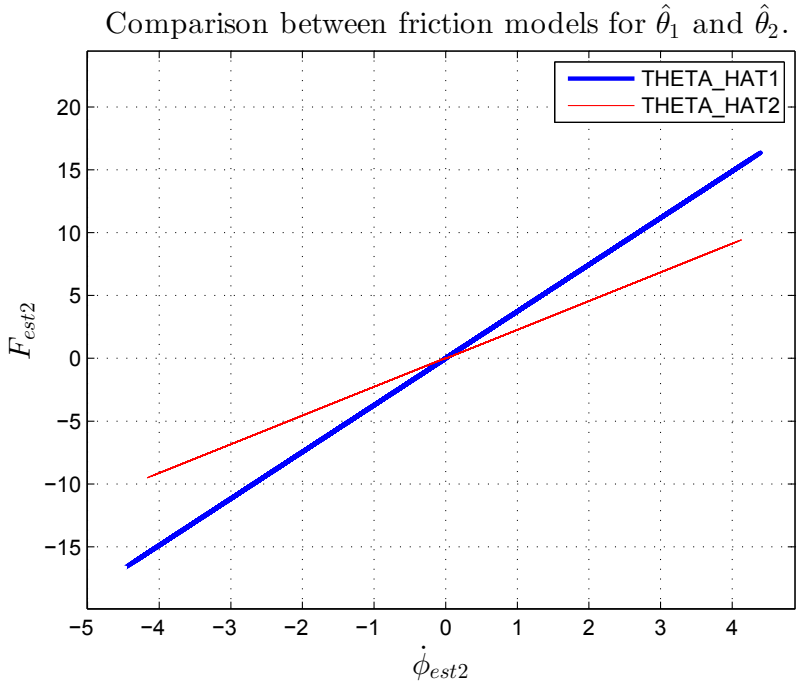

Figure 3.40: MATLAB plot displaying the friction models for $\hat{\boldsymbol{\theta}}_1$ and for $\hat{\boldsymbol{\theta}}_2$.

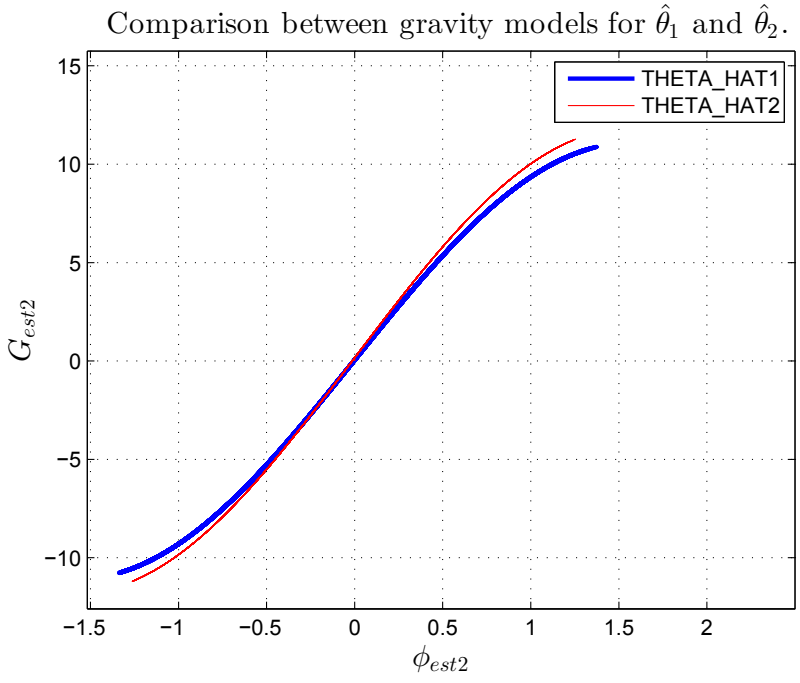

Figure 3.41: MATLAB plot displaying the gravity models for $\hat{\boldsymbol{\theta}}_1$ and for $\hat{\boldsymbol{\theta}}_2$.

When studying the two different estimates $\hat{\boldsymbol{\theta}}_1$ and $\hat{\boldsymbol{\theta}}_2$ in Tables 3.19 and 3.20, it can be seen that they differ from each other. This indicates that the estimated model is not exactly the same as the filtered measurements. If they were the same the two estimates $\hat{\boldsymbol{\theta}}_1$ and $\hat{\boldsymbol{\theta}}_2$ would be identical, which they are not.

In Tables 3.19 and 3.20 it can be seen that $\hat{\boldsymbol{\theta}}_1$ has a negative value for $\hat{k}_1$. All five parameters are assumed to be positive. When looking at Equation (3.11) it can be seen that the signs of $\hat{k}_2$ and $\hat{k}_u$ are more important than the signs of $\hat{k}_1$, $\hat{k}_3$ and $\hat{k}_4$, since $\hat{k}_1$, $\hat{k}_3$ and $\hat{k}_4$ are limited.

In Figures 3.32 - 3.35 the error between the filtered measurements and the verification simulation can be seen. It is difficult to see the difference between the error created by using $\hat{\boldsymbol{\theta}}_1$ and $\hat{\boldsymbol{\theta}}_2$. By a closer look it can be seen that the error between $\phi - \phi_{est2}$ and $\dot{\phi} - \dot{\phi}_{est2}$ for $\hat{\boldsymbol{\theta}}_2$ is a bit smaller than for $\hat{\boldsymbol{\theta}}_1$, but the error between $\ddot{\phi} - \ddot{\phi}_{est2}$ is a bit smaller for $\hat{\boldsymbol{\theta}}_1$ than $\hat{\boldsymbol{\theta}}_2$. The error for $\phi - \phi_{est2}$ converges for $\hat{\boldsymbol{\theta}}_2$, and varies around zero for $\hat{\boldsymbol{\theta}}_1$. All in all the error for $\hat{\boldsymbol{\theta}}_1$ is more varying than the error for $\hat{\boldsymbol{\theta}}_2$.

When looking at the estimated variance of disturbance in Tables 3.21 - 3.24 it can be seen that the estimated variance of disturbance for the first 25 seconds is small and the estimated variance of disturbance for the whole time sequence is 4 to 10 times larger. For both the time segments σ_1 gives the smallest values, but the difference is minimal.

For the simulation of the whole time sequence it can be seen that the error after 25 seconds is larger than the error before. This applies for both of the estimates. The error before 25 seconds is commented on above, for the error after 25 seconds the error is non-periodic with a higher amplitude. For both the estimates the error is varying around zero for $\phi - \phi_{sim}$, $\dot{\phi} - \dot{\phi}_{sim}$ and $\ddot{\phi} - \ddot{\phi}_{sim}$.

In Figure 3.40 the friction models are shown for $\hat{\boldsymbol{\theta}}_1$ and $\hat{\boldsymbol{\theta}}_2$. This figure is created by plotting F_{est2} against $\dot{\phi}_{est2}$ for the whole time sequence for the verification simulation for each of the two estimates. Plotting the whole time sequence makes it easier to see if the friction force diverges. It can be seen that the difference between the estimated friction for the two estimates is small. $\hat{k}_1$ is almost zero for both cases and hence the Coulomb friction is almost non-existing. The friction force is therefore dominated by the viscous friction, given by k_2. In the figure some irregularities can be seen around zero. It is explained in Section 3.2 how these are created by MATLAB. Here the Coulomb friction is almost zero, and the zero crossing error does not manifest itself so clearly as for cases where the Coulomb friction is larger.

The gravity models for $\hat{\boldsymbol{\theta}}_1$ and $\hat{\boldsymbol{\theta}}_2$ are created by plotting G_{est2} against ϕ_{est2} for the whole time sequence for the verification simulation for each of the two estimates. This can be seen in Figure 3.41. In this figure it can be noticed that both $\hat{\boldsymbol{\theta}}_1$ and $\hat{\boldsymbol{\theta}}_2$ result in a sinusoidal shaped form.

The calculations for this estimation are computed using MATLAB. Hence the numerical accuracy explained in Section 3.2 applies here too. It is also possible that the model used with the system identification method is wrong. The friction model is assumed to be Coulomb friction combined with viscous friction, which is a static model. This is one of the simplest models for friction. Since the IRB 140 is a complicated device it is sensible to assume that the actual friction model is more complicated than anticipated.

3.3.2.3 Estimation using measurements from the third experiment

For this case the amplitude and frequency for the reference in Equation (3.20) were set to $a = \frac{\pi}{4}$ and $\omega = \pi$.

The five unknown parameters were calculated using filtered measurements from the 6th joint of IRB 140. These estimates are collected in the vector $\hat{\boldsymbol{\theta}}_1$, and can be seen in Table 3.25.

An estimated model was created using ϕ and u from the filtered measurements. With this estimated model an alternative estimate called $\hat{\boldsymbol{\theta}}_2$ was computed. In Table 3.26 the estimate $\hat{\boldsymbol{\theta}}_2$ is presented.

Based on $\hat{\boldsymbol{\theta}}_1$ and $\hat{\boldsymbol{\theta}}_2$ the variance of the disturbances, found in Equation (3.19), were calculated using the filtered measurements. In Tables 3.27 - 3.30 the variance of the disturbances for the two estimates are shown.

A new simulation was performed using the estimated values, this was done as a verification of the estimated values. The error between the filtered measurements and this simulation is presented in Figures 3.42 - 3.45. Then a simulation using the whole time sequence was performed, and the error between this simulation and the filtered measurements is shown in Figures 3.46 - 3.49.

At the end the friction and gravity models for the two different estimates are presented in Figures 3.50 and 3.51.

$\hat{k}_1$	=	-0.0232
$\hat{k}_2$	=	1.4224
$\hat{k}_3$	=	1.0338
$\hat{k}_4$	=	-0.0094
$\hat{k}_u$	=	0.3167

Table 3.25: $\hat{\boldsymbol{\theta}}_1$, estimate of unknown parameters.

$\hat{k}_1$	=	-0.0296
$\hat{k}_2$	=	-2.5162
$\hat{k}_3$	=	1.0397
$\hat{k}_4$	=	0.0025
$\hat{k}_u$	=	-0.4998

Table 3.26: $\hat{\boldsymbol{\theta}}_2$, estimate of unknown parameters.

$\hat{\sigma}_{1a}$	=	1.4404

Table 3.27: $\hat{\sigma}_{1a}$, estimated variance of the disturbance for $\hat{\boldsymbol{\theta}}_1$ using filtered measurements, time step: 1 - 20 000.

$\hat{\sigma}_{2a}$	=	1.5640

Table 3.28: $\hat{\sigma}_{2a}$, estimated variance of the disturbance for $\hat{\boldsymbol{\theta}}_2$ using filtered measurements, time step: 1 - 20 000.

$\hat{\sigma}_{1b}$	=	0.0124

Table 3.29: $\hat{\sigma}_{1b}$, estimated variance of the disturbance for $\hat{\boldsymbol{\theta}}_1$ using filtered measurements, time step: 11 - 4 874.

$\hat{\sigma}_{2b}$	=	0.1923

Table 3.30: $\hat{\sigma}_{2b}$, estimated variance of the disturbance for $\hat{\boldsymbol{\theta}}_2$ using filtered measurements, time step: 11 - 4 874.

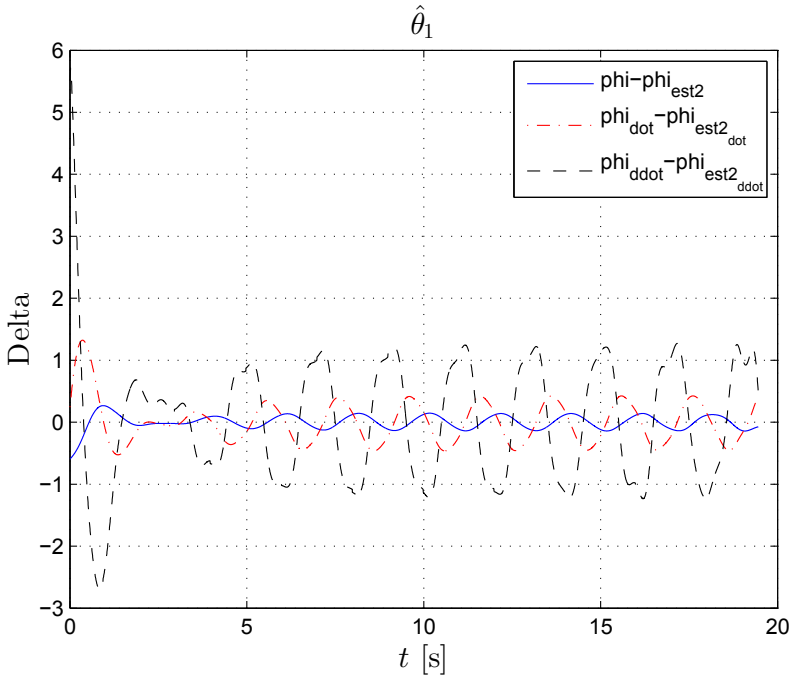

Figure 3.42: MATLAB plot displaying the error between the filtered measurements and the verification simulation for $\hat{\boldsymbol{\theta}}_1$.

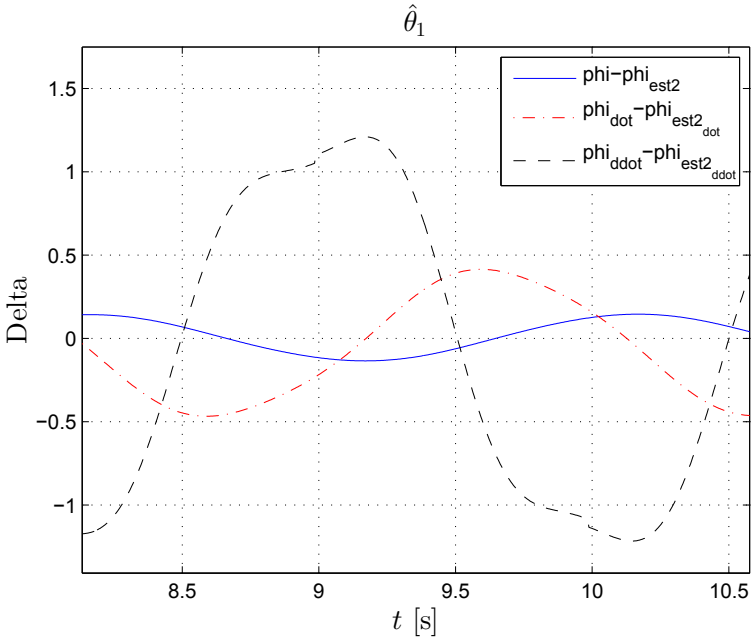

Figure 3.43: Detail from the MATLAB plot displaying the error between the filtered measurements and the verification simulation for $\hat{\boldsymbol{\theta}}_1$.

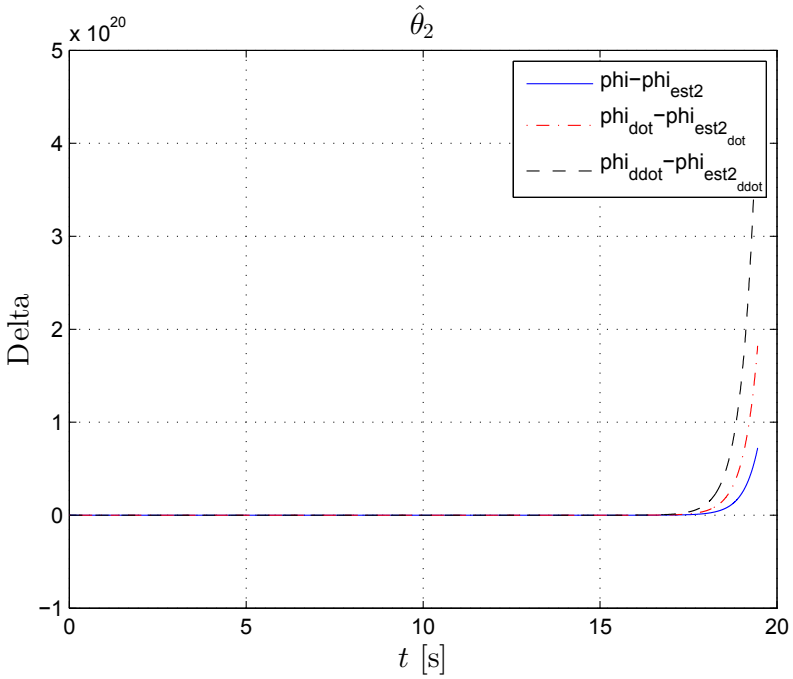

Figure 3.44: MATLAB plot displaying the error between the filtered measurements and the verification simulation for $\hat{\boldsymbol{\theta}}_2$.

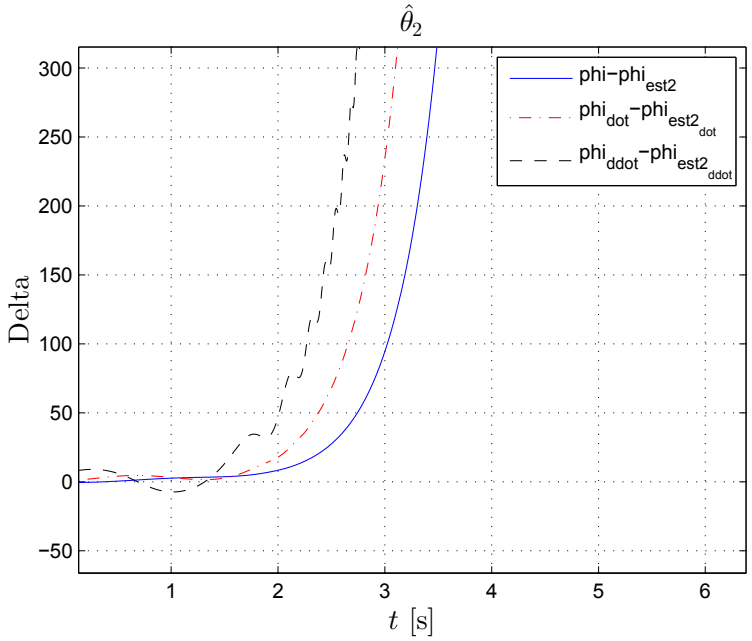

Figure 3.45: Detail from the MATLAB plot displaying the error between the filtered measurements and the verification simulation for $\hat{\boldsymbol{\theta}}_2$.

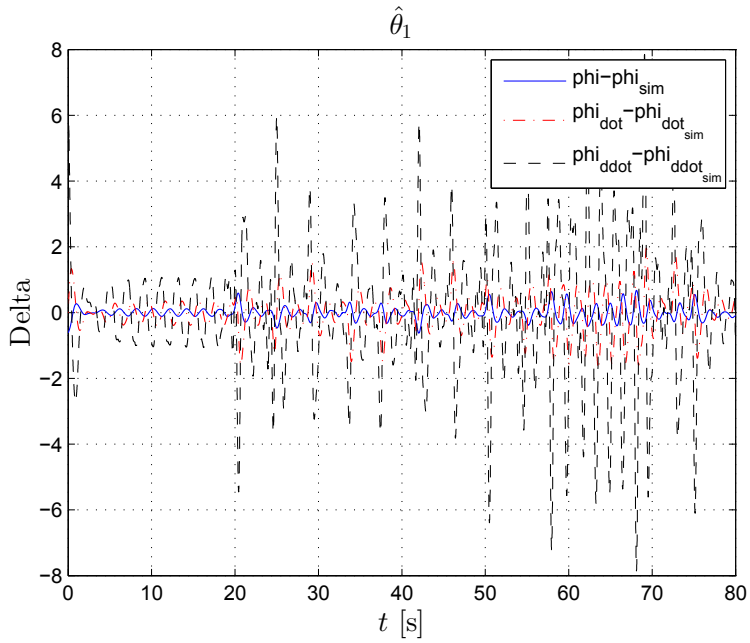

Figure 3.46: MATLAB plot displaying the error between the filtered measurements and the verification simulation for the whole time sequence.

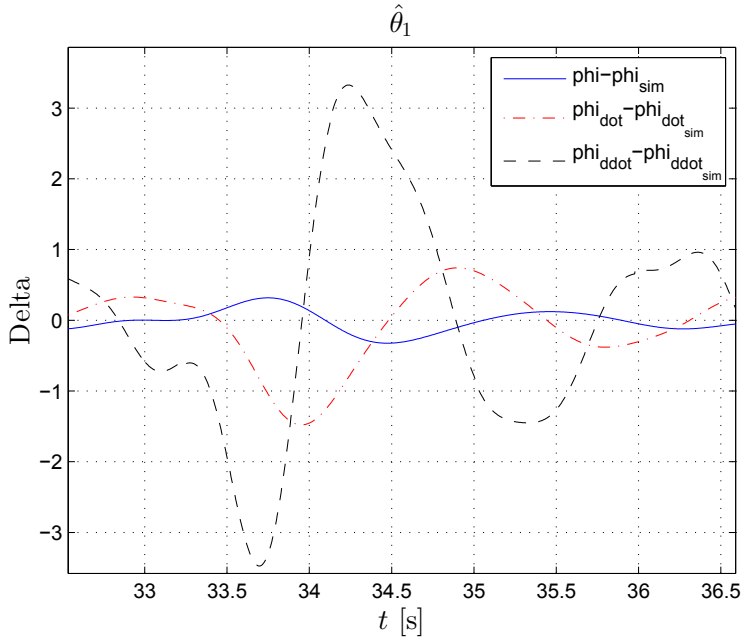

Figure 3.47: Detail from the MATLAB plot displaying the error between the filtered measurements and the verification simulation for the whole time sequence.

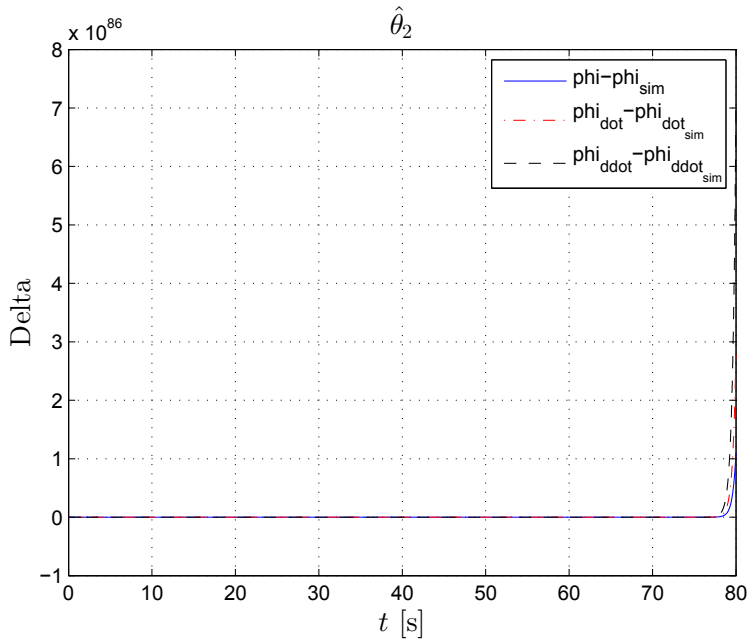

Figure 3.48: MATLAB plot displaying the error between the filtered measurements and the verification simulation for the whole time sequence.

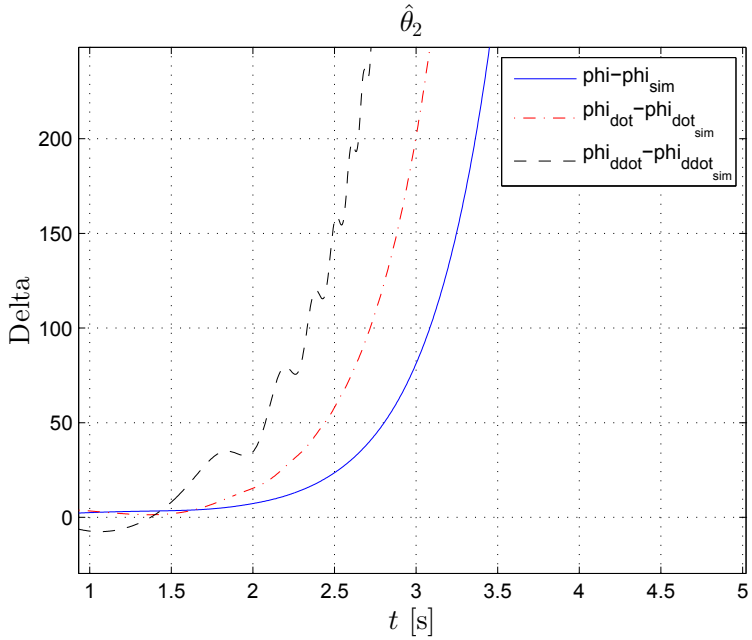

Figure 3.49: Detail from the MATLAB plot displaying the error between the filtered measurements and the verification simulation for the whole time sequence.

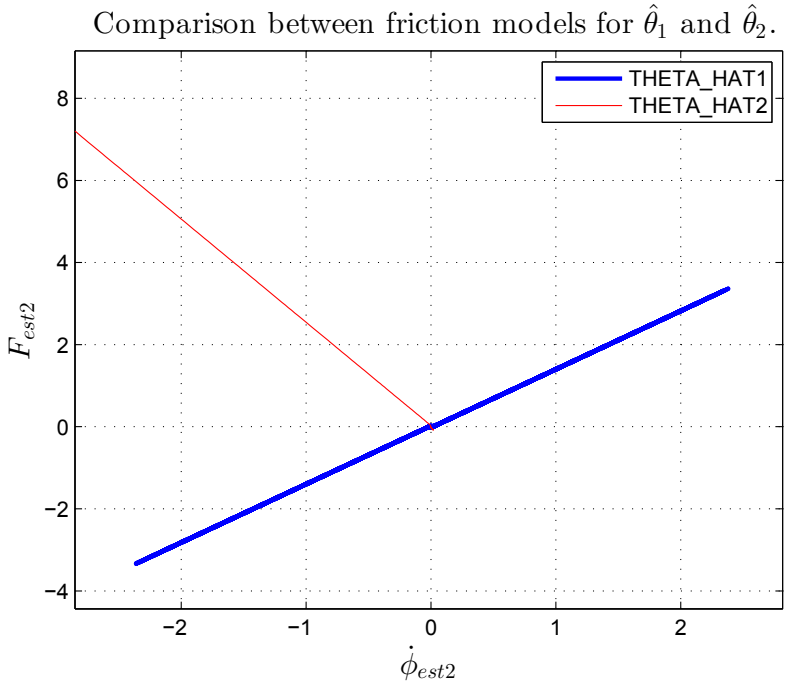

Figure 3.50: MATLAB plot displaying the friction models for $\hat{\boldsymbol{\theta}}_1$ and for $\hat{\boldsymbol{\theta}}_2$.

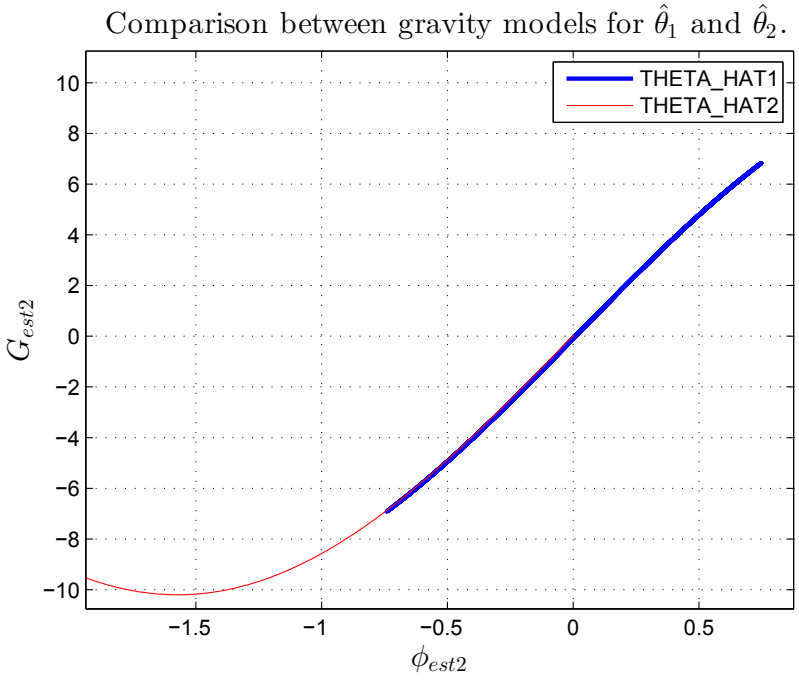

Figure 3.51: MATLAB plot displaying the gravity models for $\hat{\boldsymbol{\theta}}_1$ and for $\hat{\boldsymbol{\theta}}_2$.

When studying the two different estimates $\hat{\boldsymbol{\theta}}_1$ and $\hat{\boldsymbol{\theta}}_2$ in Tables 3.25 and 3.26 it can be seen that they differ from each other. This indicates that the estimated model is not exactly the same as the filtered measurements. If they were the same the two estimates $\hat{\boldsymbol{\theta}}_1$ and $\hat{\boldsymbol{\theta}}_2$ would be identical, which they are not.

In Tables 3.25 and 3.26 it can be seen that $\hat{\boldsymbol{\theta}}_1$ has negative values for $\hat{k}_1$ and $\hat{k}_4$ and that $\hat{\boldsymbol{\theta}}_2$ has negative values for $\hat{k}_1$, $\hat{k}_2$ and $\hat{k}_u$. All five parameters are assumed to be positive. When looking at Equation (3.11) it can be seen that the signs of $\hat{k}_2$ and $\hat{k}_u$ are more important than the signs of $\hat{k}_1$, $\hat{k}_3$ and $\hat{k}_4$, since $\hat{k}_1$, $\hat{k}_3$ and $\hat{k}_4$ are limited. If $\hat{k}_2$ is negative instead of positive the viscous friction will work with the motion instead of against, and if $\hat{k}_u$ is negative instead of positive the actuator force will work in the wrong direction. Based on this it is likely to guess that $\hat{\boldsymbol{\theta}}_1$ is closer to the true values than $\hat{\boldsymbol{\theta}}_2$.

When looking at the error between the filtered measurements and the verification simulation, for $\hat{\boldsymbol{\theta}}_1$ in Figures 3.42 and 3.43, it can be seen that $\phi - \phi_{est2}$, $\dot{\phi} - \dot{\phi}_{est2}$ and $\ddot{\phi} - \ddot{\phi}_{est2}$ oscillates around zero.

In the error measurements for $\hat{\boldsymbol{\theta}}_2$ in Figures 3.44 and 3.45, it can be seen that the error between $\phi - \phi_{est2}$, $\dot{\phi} - \dot{\phi}_{est2}$ and $\ddot{\phi} - \ddot{\phi}_{est2}$ increase exponentially. This is probably caused by the negative values for $\hat{k}_2$ and $\hat{k}_u$.

When looking at the estimated variance of disturbance in Tables 3.27 - 3.30 it can be seen that the estimated variance of disturbance for the first 25 seconds is small and the estimated variance of disturbance for the whole time sequence is 8 to 116 times larger. For both the time segments σ_1 gives the smallest values, but not by much.

For the simulation of the whole time sequence for $\hat{\boldsymbol{\theta}}_1$ it can be seen that the error after 25 seconds is larger than the error before. The error before 25 seconds is commented on above, for the error after 25 seconds the error is non-periodic with a higher amplitude, i.e. the error is varying around zero for $\phi - \phi_{sim}$, $\dot{\phi} - \dot{\phi}_{sim}$ and $\ddot{\phi} - \ddot{\phi}_{sim}$. For $\hat{\boldsymbol{\theta}}_2$ it can be seen that the error between $\phi - \phi_{sim}$, $\dot{\phi} - \dot{\phi}_{sim}$ and $\ddot{\phi} - \ddot{\phi}_{sim}$ increase exponentially.

In Figure 3.50 the friction models are shown for $\hat{\boldsymbol{\theta}}_1$ and $\hat{\boldsymbol{\theta}}_2$. This figure is created by plotting F_{est2} against $\dot{\phi}_{est2}$ for the whole time sequence for the verification simulation for each of the two estimates. Plotting the whole time sequence makes it easier to see if the friction force diverges. It is explained in Section 3.2 how the plots are drawn in MATLAB. In Figure 3.50 it can be seen that the friction force diverges for $\hat{\boldsymbol{\theta}}_2$. This might be caused by the same reason as for the exponential error already discovered in Figure 3.44. The friction model for $\hat{\boldsymbol{\theta}}_1$ shows a typical viscous friction.

The gravity models for $\hat{\boldsymbol{\theta}}_1$ and $\hat{\boldsymbol{\theta}}_2$ is created by plotting G_{est2} against ϕ_{est2} for the whole time sequence for the verification simulation for each of the two estimates. This can be seen in Figure 3.51. In this figure it can be noticed that both $\hat{\boldsymbol{\theta}}_1$ and $\hat{\boldsymbol{\theta}}_2$ result in a sinusoidal shaped form. It is observed that the sinusoid shape created from $\hat{\boldsymbol{\theta}}_2$ diverges in the leftmost direction. This could be caused by the negative values for $\hat{k}_2$ and $\hat{k}_u$.

Even though the variance of disturbance is small for both $\hat{\boldsymbol{\theta}}_1$ and $\hat{\boldsymbol{\theta}}_2$, it is quite clear by looking at the figures that the estimated parameters in $\hat{\boldsymbol{\theta}}_2$ is not a valid choice. When deciding what estimate to select, one cannot only look at the variance. It is also important to take into account the error between the measurements and the verification simulation for the different estimates.

The calculations for this estimation are computed using MATLAB. Hence the numerical accuracy explained in Section 3.2 applies here too. It is also possible that the model used with the system identification method is wrong. The friction model is assumed to be Coulomb friction combined with viscous friction, which is a static model. This is one of the simplest models for friction. Since the IRB 140 is a complicated device it is sensible to assume that the actual friction model is more complicated than assumed here.

3.4 Discussion and Conclusion

It was assumed that the five unknown parameters could be estimated despite the presence of disturbance. With three different experiments six different estimates were created. To get better estimates segments of the measurements were used as basis for system identification.

When studying these segmented experiments it was discovered that the first experiment had larger variance of disturbance than the second and third experiments. For the third experiment it was discovered that the errors between $\phi - \phi_{sim}$, $\dot{\phi} - \dot{\phi}_{sim}$ and $\ddot{\phi} - \ddot{\phi}_{sim}$ were much larger than for the first and second experiments. For the second experiment it was discovered that both the variance of disturbance and the errors between $\phi - \phi_{sim}$, $\dot{\phi} - \dot{\phi}_{sim}$ and $\ddot{\phi} - \ddot{\phi}_{sim}$ were quite small.

From these discoveries it was concluded that the second experiment gave the best estimate. Then $\hat{\boldsymbol{\theta}}_1$ and $\hat{\boldsymbol{\theta}}_2$ had to be examined to find the best estimate for the IRB 140.

It was discovered that the largest difference between $\hat{\boldsymbol{\theta}}_1$ and $\hat{\boldsymbol{\theta}}_2$ was that $\hat{\boldsymbol{\theta}}_2$ converges to zero for $\phi - \phi_{est2}$, while $\hat{\boldsymbol{\theta}}_1$ do not have this quality. From this it was deduced that $\hat{\boldsymbol{\theta}}_2$ was a better choice than $\hat{\boldsymbol{\theta}}_1$.

The values for $\hat{\boldsymbol{\theta}}_2$ using the second experiment is

$\hat{k}_1$	=	-0.0221
$\hat{k}_2$	=	2.2875
$\hat{k}_3$	=	1.2034
$\hat{k}_4$	=	0.0166
$\hat{k}_u$	=	0.7075

Table 3.31: Estimation results of unknown parameters.

These estimated parameters will be used with a controller in Chapter 4. Notice that $\hat{k}_1$ and $\hat{k}_4$ are close to zero. When used with the passivity-based robust controller, the friction compensation will almost be linear.

Chapter 4

Controller for the 6th joint of IRB 140

A passivity-based robust controller for the 6th joint of IRB 140 was created using the method described in Section 2.10. The estimated parameters which were concluded to be the best in Chapter 3 were used with this controller. When using these parameters the Coulomb friction is small, and the friction compensation is therefore almost proportional to the velocity, $\dot{q}_6$.

The controller was implemented and tested using Simulink, before it was added to the robot software used to control IRB 140 at the Robotics Lab. Anton Pyrkin and Stepan Pchelkin implemented the designed controller with the robot software and run the different experiments at the lab. Using the instructions in Appendix A the Simulink code for the controller can be found.

The controller was tested with four different scenarios, and with four different experiment for each of the scenarios. The different scenarios are presented in Table 4.1 together with their abbreviation used in the figures. For each of the experiments measurements for q_6, q_6^d, u and $q_{6_{error}}$ were recorded. For these experiments the reference is given by

$$q_6^d = a\sin(\omega_i t), \qquad i = 1, 2, 3, 4 \tag{4.1}$$

By changing the values of ω in Equation (4.1) the different experiments were created. The values for these experiments can be found in Table 4.2.

Experiment	**Abbreviation**
Empty gripper	e
Loaded gripper, holding a stick in its center point	m
Loaded gripper, holding a stick, the longest end pointing up	t
Loaded gripper, holding a broom, with the brush end down	b

Table 4.1: The four different scenarios and their abbreviations.

a	$=$	$\frac{\pi}{2}$	ω_1	$=$	0.1
a	$=$	$\frac{\pi}{2}$	ω_2	$=$	0.5
a	$=$	$\frac{\pi}{2}$	ω_3	$=$	1.5
a	$=$	$\frac{\pi}{2}$	ω_4	$=$	2.3

Table 4.2: The amplitude and the frequency for the four different experiments.

4.1 The Passivity-Based Robust Controller

Remember Equation (3.11) from Chapter 3, where the system to be controlled was assumed to be

$$\ddot{q}_6 = -k_1\ sign(\dot{q}_6) - k_2\ \dot{q}_6 - k_3\ g\ \sin(q_6) - k_4\ g\ \cos(q_6) + k_u\ u \tag{4.2}$$

The designed controller is

$$u = \frac{a}{\hat{k}_u} + \frac{\hat{k}_1}{\hat{k}_u} sign(v) + \frac{\hat{k}_2}{\hat{k}_u} v + \frac{\hat{k}_3}{\hat{k}_u} g \sin(q_6) + \frac{\hat{k}_4}{\hat{k}_u} g \cos(q_6) - \frac{K\ r}{\hat{k}_u} \tag{4.3}$$

where

$$v = \dot{q}_6^d - \lambda_1 \tilde{q}_6 \tag{4.4}$$
$$a = \dot{v} = \ddot{q}_6^d - \lambda_2 \dot{\tilde{q}}_6 \tag{4.5}$$
$$r = \dot{q}_6 - v = \dot{\tilde{q}}_6 + \lambda_1 \tilde{q}_6 \tag{4.6}$$

Here q_6^d is desired joint position, q_6, and λ_1, λ_2 and K are positive scalar constants, and $\tilde{q}_6$ and $\dot{\tilde{q}}_6$ are defined as

$$\tilde{q}_6 = q_6 - q_6^d \tag{4.7}$$
$$\dot{\tilde{q}}_6 = \dot{q}_6 - \dot{q}_6^d \tag{4.8}$$

For the scenarios the positive scalar constants were chosen as $\lambda_1 = 2$, $\lambda_2 = 1$ and $K = 2$.

4.2 Experimental Results

The frequency $\omega_1 = 0.1$ was chosen for the four different scenarios. In Figure 4.1 a comparison between the measured position and the measured reference position for the experiment with empty gripper can be seen. The figures containing the comparison between the measured position and the measured reference position for the three other scenarios are almost the same as for the first scenario and are not included here.

To be able to see the accuracy of the controller the error of all the different scenarios are presented together in Figure 4.2. The controller should theoretically have smaller error for the empty gripper than for the other scenarios, since this is the same case as used to identify the parameters for the model.

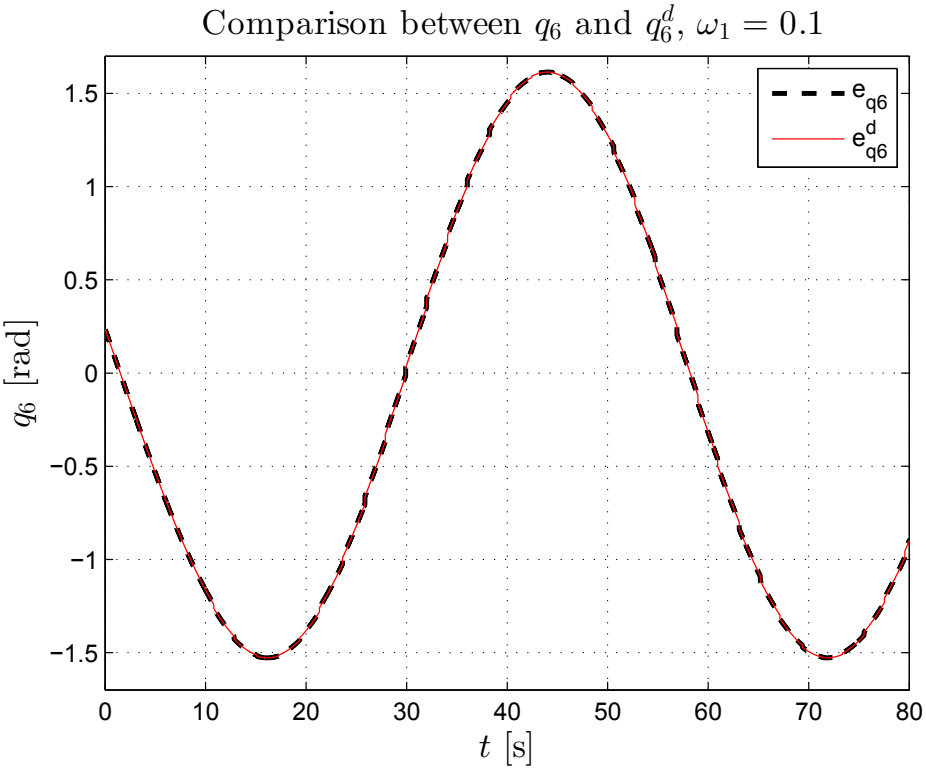

Figure 4.1: MATLAB plot displaying the position q_6(t), for experiment with empty gripper.

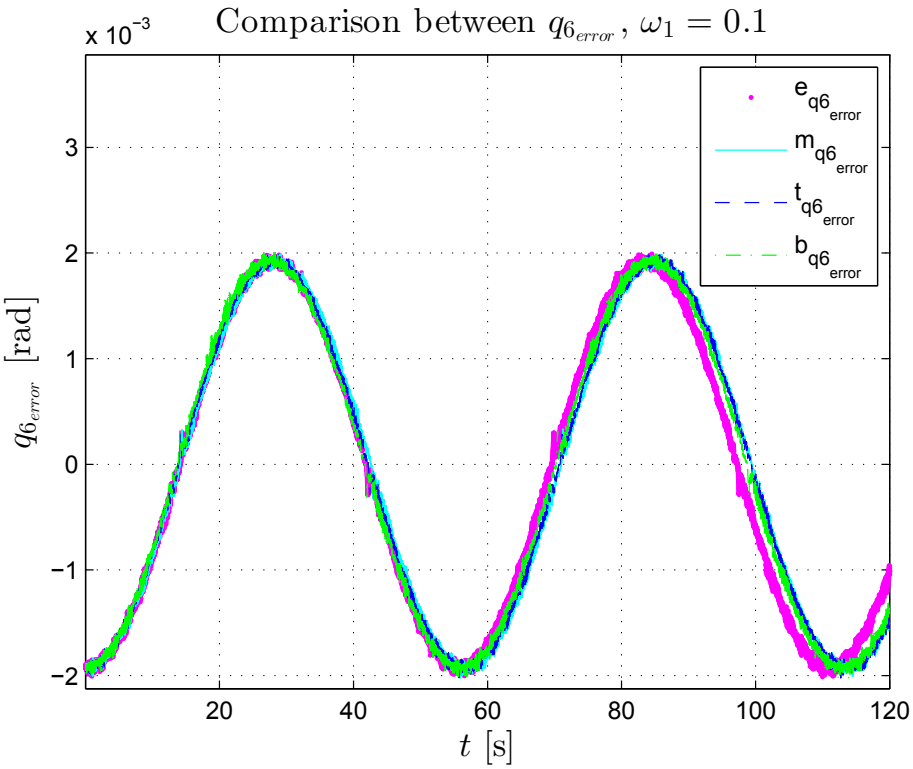

Figure 4.2: MATLAB plot displaying the error between the measured position and the measured reference position.

When looking at Figure 4.2 it can be seen that the error is approximately the same for the four different scenarios. The differences in frequencies, which is easier to see at the end of the figure than in the start, indicate that there are some unmodelled nonlinearities which affect the system. This is reasonable since the robot joint might be affected by nonlinear friction forces, which is controlled using an almost linear friction compensation.

Two additional scenarios were designed to investigate if it was possible to achieve smaller error for the empty gripper. First the friction coefficients $\hat{k}_1$ and $\hat{k}_2$ was set to 0; in the figures this is indicated by $eNFC$. Then λ_1 and K was set to 5; in the figures this is indicated by $el5k5$. The error measurements from these two supplementary experiments can be seen in Figure 4.3.

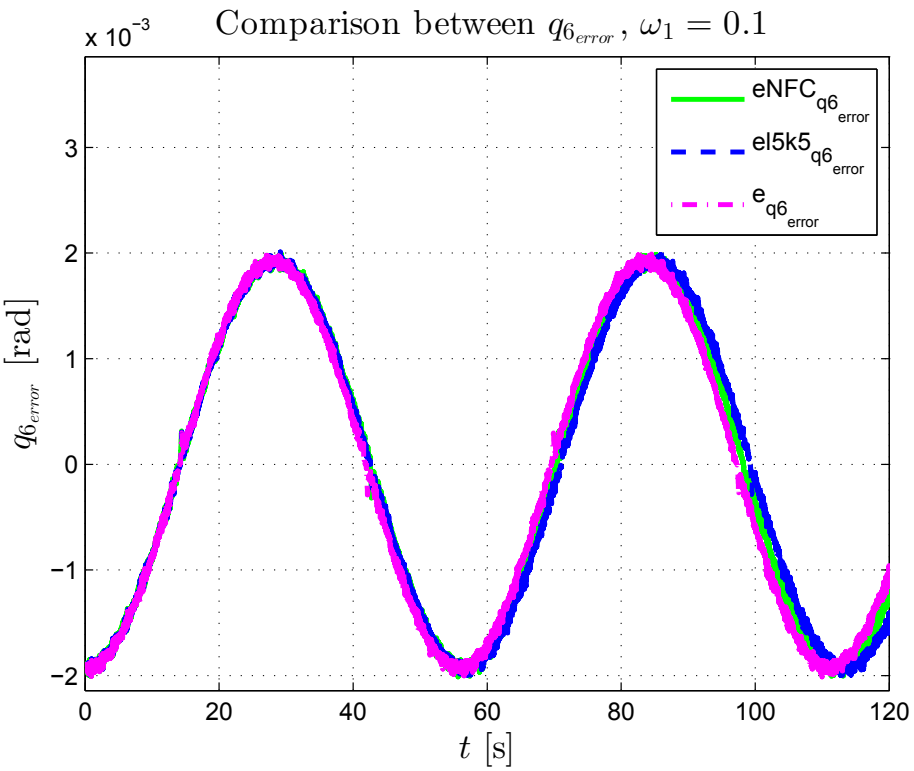

Figure 4.3: MATLAB plot displaying the error between the measured position and the measured reference position.

When looking at Figure 4.3 it is easy to see that the removal of the friction compensation and the change of parameters for λ_1 and K have minimal effect on the accuracy of the passivity-based robust controller. This gives an indication that the estimated parameters for the friction model might be

wrong, since it is of no consequence to remove the friction compensation from the controller. It is even a possibility that the chosen friction model is wrong.

To validate if this was the case for other frequencies, ω was set to 0.5 for the four different scenarios. The error of the scenarios are presented together in Figure 4.4, and the two additional scenarios are presented in Figure 4.5.

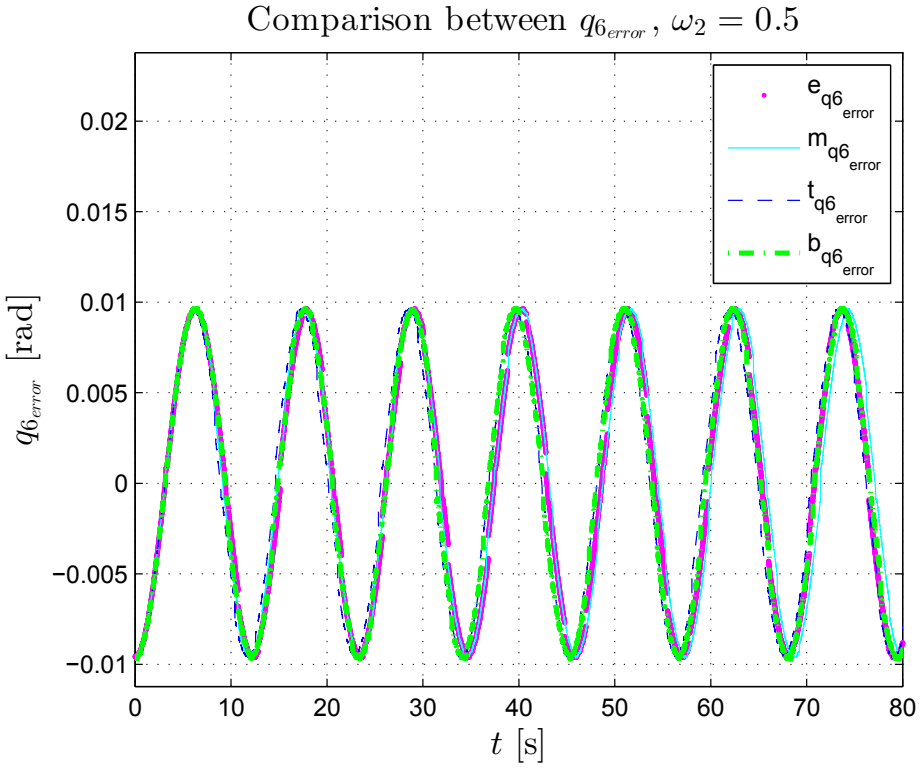

Figure 4.4: MATLAB plot displaying the error between the measured position and the measured reference position.

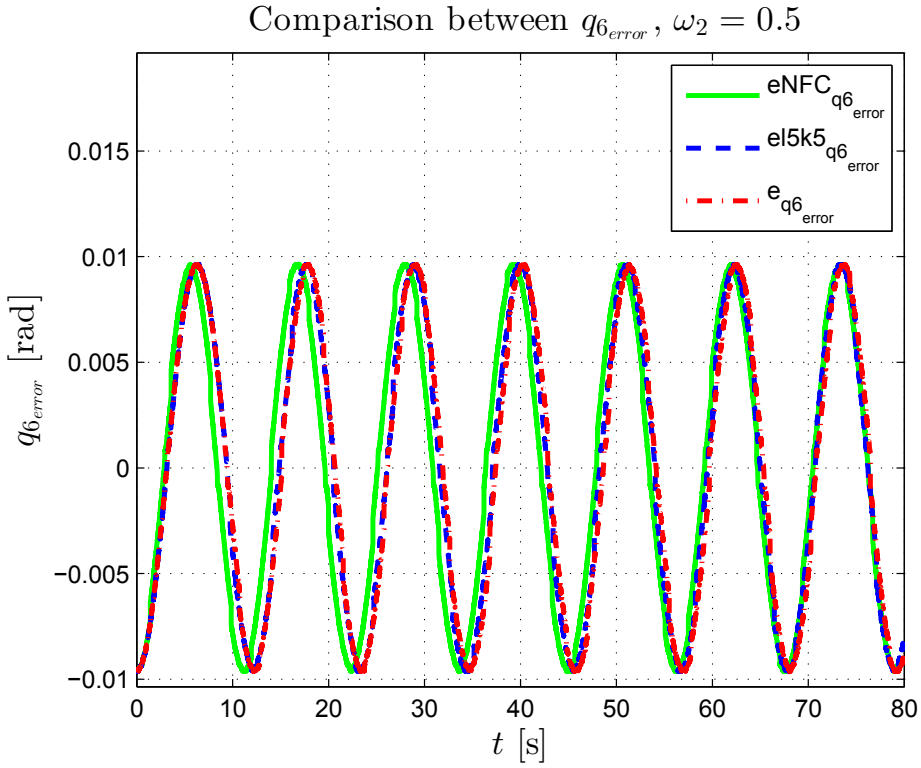

Figure 4.5: MATLAB plot displaying the error between the measured position and the measured reference position.

When looking at Figures 4.4 and 4.5, the amplitude of the error is the same for all of the original scenarios and the additional scenarios. This acknowledges the suspicion from the experiment with $\omega_1 = 0.1$. The estimates for the friction parameters or the friction model are probably wrong. This means that the friction compensation probably is wrong too. It can also be noticed that the change in frequency affect the amplitude of the error between q_6 and q_6^d. Higher frequency gives higher error amplitude.

For the fourth scenario the friction in the gripper was not large enough to hold the broom for frequency $\omega = 0.8$. When running the robot with this frequency the gripper lost hold of the broom after 44 s. This can be seen in Figures 4.6 and 4.7. When inspecting the broom after the experiments, it was discovered to have visible marks in the wood where it had been held by the gripper.

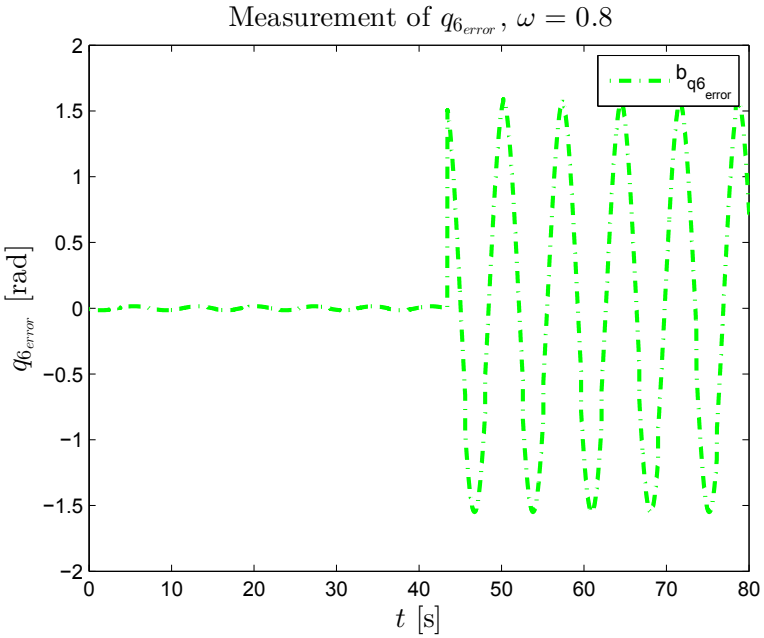

Figure 4.6: MATLAB plot displaying the error between the measured position and the measured reference position.

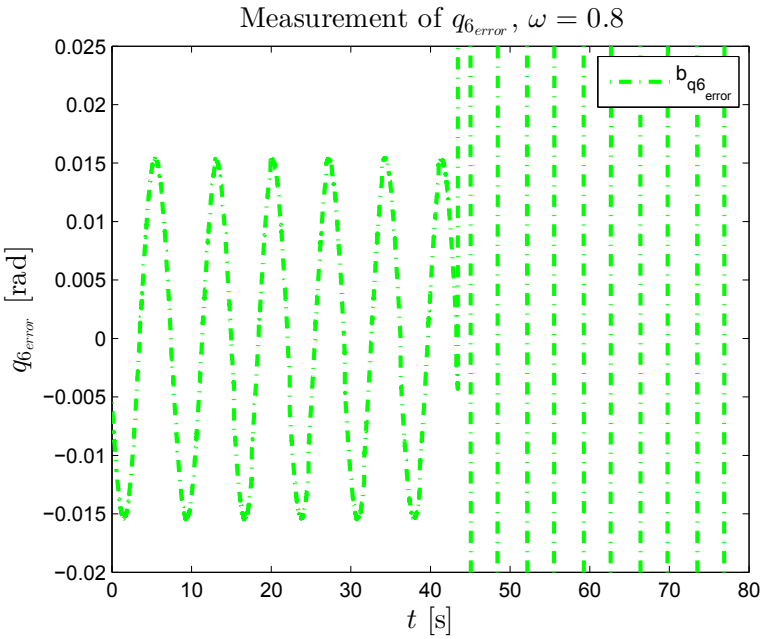

Figure 4.7: Detail from the MATLAB plot displaying the error between the measured position and the measured reference position.

For the three other scenarios where the gripper was able to hold the load for higher frequencies than $\omega = 0.8$, the frequencies $\omega_3 = 1.5$ and $\omega_4 = 2.3$ were tested. The error between the position measurements and the position reference measurements can be seen in Figures 4.8 - 4.11.

In Figures 4.8 - 4.11 it can be seen that the error between the measured position and the measured reference position is almost the same for the three different experiments, for both values of ω. The error has a bit higher amplitude for $\omega_4 = 2.3$ than for $\omega_3 = 1.5$.

When studying the details in Figures 4.9 and 4.11 some jumps in the error can be seen. These jumps can be caused by different reasons. One reason might be the communication between the sensor in the robot and the computer recording the measurements. Another reason can be that the reference changed in such a way that the positon of the robot suddenly was closer to or farther from the reference.

The estimated values for the parameters used with the controller were incorrect, therefore it was proposed to use the new measurements for the empty gripper and see if it was possible to achieve new estimates which could give a more correct model of the robot and hence achieve better accuracy for the controller. The estimates obtained from the new measurements from the passivity-based robust controller for system identification was worse than the estimates already presented in Chapter 3. The estimated values for the five parameters were all negative or close to zero. The variance of disturbance was high, and the error between the filtered measurements and the verification simulation was large.

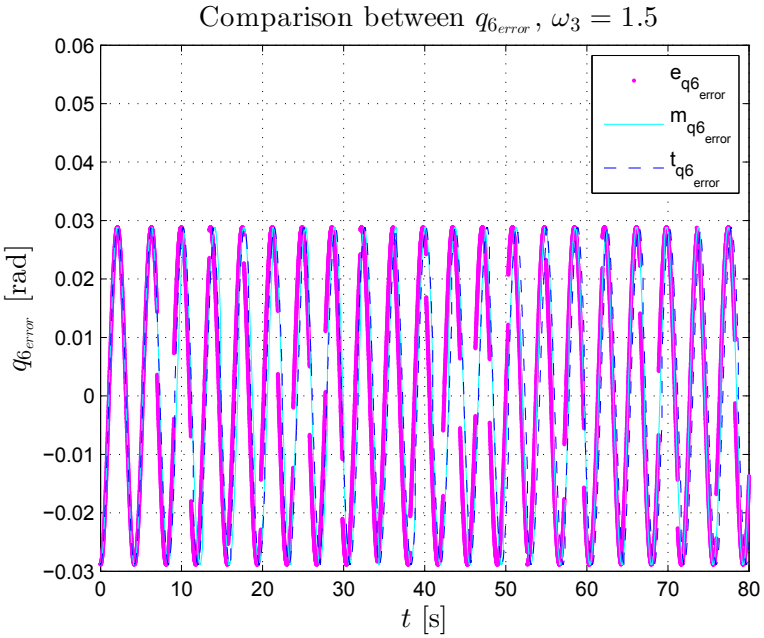

Figure 4.8: MATLAB plot displaying the error between the measured position and the measured reference position.

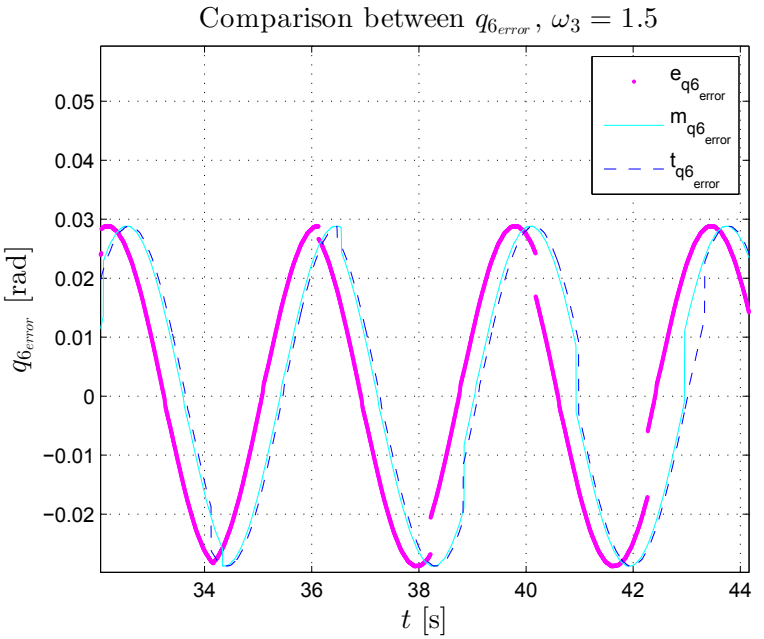

Figure 4.9: Detail from the MATLAB plot displaying the error between the measured position and the measured reference position.

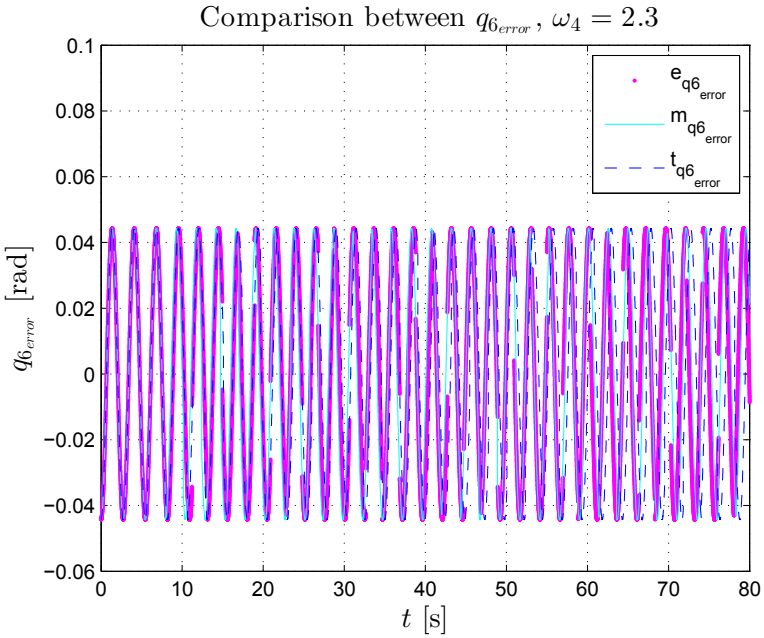

Figure 4.10: MATLAB plot displaying the error between the measured position and the measured reference position.

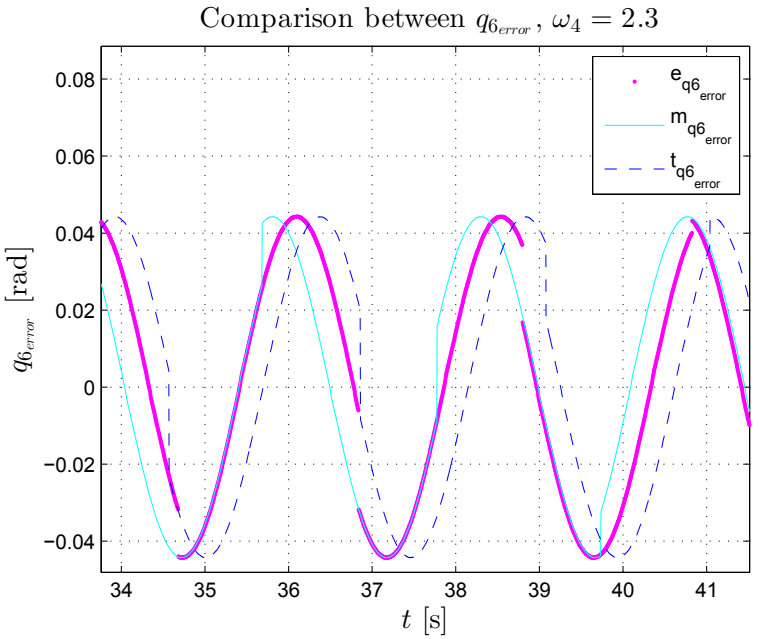

Figure 4.11: Detail from the MATLAB plot displaying the error between the measured position and the measured reference position.

4.3 Discussion

From the experiments at the Robotics Lab with the passivity-based robust controller for the 6th joint of IRB 140, it was discovered that the estimated parameters were not the same as the unknown parameters. When the unknown parameters were estimated, measurements from the empty gripper was used. The error should thus be smaller for the scenario with the empty gripper than for the other scenarios. Since this was not the case it was assumed that the estimated parameters for the 6th joint of IRB 140 were incorrect.

To create a more correct estimate of the parameters the new measurements of the empty gripper were filtered and used to create new estimates of the unknown parameters. The estimates achieved from using the new measurements from the passivity-based robust controller for system identification was worse than the estimates already presented in Chapter 3. The estimated values for the five parameters were all negative or close to zero. The variance of disturbance was high, and the error between the filtered measurements and the verification simulation was large.

For the lowest frequency tested it can be seen that the error between the reference and the position was oscillating with an amplitude at ± 0.002 rad. Hence it was discovered that the passivity-based robust controller is less accurate than the ABB RobotStudio controller. The poor accuracy for the passivity-based robust controller is clearly linked to the estimated parameters for the 6th joint of IRB 140. It is assumed that better estimated parameters would have given better accuracy for the passivity-based robust controller for the 6th joint of IRB 140.

All experiments in Chapter 3 and in Chapter 4 used a simple sinusoidal signal as reference. A reference signal containing a simple sinusoidal signal is not general enough for a system with five unknown parameters to be identified. It is likely that the reference used for the estimation experiments, when the 6th joint was to be identified, was not general enough for the signal to be PE for this system.

For the experiment with the broom it was discovered that the friction in the gripper was too low to actually manage to hold onto the broom for higher frequencies. The broom itself also had marks from where the gripper had been holding it. To avoid a casted component to be thrown through the room or to be crushed with the gripper, limitations of the velocity and force control of the gripper have to be evaluated. When this is controlled, pick-and-place and processing operations of different complexities can be performed with and on a casted component.

In Chapter 3 it was discovered that the system identification model was too simple to interpret the nonlinearities in the measurements. With a more complicated friction model the problem with nonlinearities could have been removed and the estimated parameters would probably have been more correct. A combination of a more complicated friction model and a more general reference signal used to excite the 6th joint of IRB 140 would probably achieved better accuracy for the passivity-based robust controller for the 6th joint of IRB 140.

When creating the reference for the passivity-based robust controller it was discovered that the reference created was the same as the reference used with the controller. In "*Using ABB MultiMove Functionality for Cooperative Manipulation Tasks*" [6] by Fikkan it was seen that the reference created offline was not the same reference used by the robot when running the program online. With the poor accuracy for the passivity-based robust controller there is a trade-off between which controller to use. The passivity-based robust controller is not very accurate, but it is easy to create the correct reference. For the ABB RobotStudio controller the accuracy is sufficient, but it is difficult to program the robot so that the reference is the same offline and online for the robot.

The best solution would probably be to create new measurements to be used with an updated system identification model. Then create new consistent estimates for an updated passivity-based robust controller. When an accurate enough controller for the 6th joint of IRB 140 is created, and the force/velocity limitations of the gripper is taken care of, it is possible to begin investigating pick-and-place and processing operations with and on casted components.

Chapter 5

Conclusions and Further Work

5.1 Conclusions

In Chapter 3 the LS method was tested on a simulated model for the 6th joint of IRB 140. Then the same method was used to estimate the unknown parameters, using three different filtered measurements from the IRB 140. The results achieved were not consistent. After comparing the results against each other, it were decided to use the estimated parameters from the second experiment. More precise $\hat{\boldsymbol{\theta}}_2$, found using a segment of the filtered measurements for the second experiment.

Then in Chapter 4 a passivity-based robust controller was created for the 6th joint of IRB 140, using the estimated parameters from Chapter 3. When studying the experimental results for the controller, it was discovered that the error was approximately the same for the case used to estimate the parameters and the cases where the gripper was holding additional load. This indicated that the estimated parameters were incorrect.

From the experimental results it was discovered that it did not matter if the friction compensation of the controller was turned on or off. This can be caused by three different reasons, or a combination of them. One of them is that the single sinusoidal reference signal used to identify the unknown parameters is too simple for the signal to have PE. Another reason is that the lowpass filter used to filter the measurements did not remove enough of the noise and that the cut off frequency has to be tuned one more time. The third reason is that the friction model chosen was too simple compared to the real friction forces of IRB 140.

The measurements from the new experiments with the scenarios for the empty gripper was filtered and used for system identification with the LS method presented in Chapter 3. The idea was that this might give better estimates than the filtered measurements obtained from Stepan Pchelkin. When comparing the results from these new estimates it was easy to see that the original estimates achieved using the measurements from Stepan Pchelkin was better than the new estimates.

When the robot was holding a broom in the gripper it was discovered that the friction in the gripper did not manage to hold onto the broomstick at frequency $\omega = 0.8$. The broom had marks from the gripper which indicate that the gripper was holding tight, but the gripper still lost hold of the broomstick. Based on this it was decided that it is essential to consider force/velocity limitations for the gripper to not crush the casted component while grasping it and to not lose hold of casted components while moving.

5.2 Further Work

To use IRB 140, IRB 1600 and IRB 4600 for pick-and-place and processing operations of different complexities, the estimation of parameters for IRB 140 has to be completed, and a controller has to be created using the correct estimates. In the Discussion in Chapter 4 it was proposed to create new measurements, which should be based on a more general reference signal than a simple sinusoidal signal to be used with an updated system identification model including a more advanced friction model, for creating new consistent estimates.

Because of the noise it could be interesting to investigate if the errors-in-variables models could be used instead of the LS method for identifying the unknown parameters. When consistent results have been achieved these parameters could be used to update the passivity-based robust controller including the updated friction model. When satisfied with the accuracy after testing it at the Robotics Lab with IRB 140, the force/velocity limitations of the gripper should be taken care of. The system identification should be computed for all of the joints of IRB 140, so that a controller could be designed to control the whole robot.

When the controller for IRB 140 is designed and tested to be accurate enough, the parameters for IRB 1600 and IRB 4600 should be identified and implemented with controllers where the speed and force limitations are taken care of. Then pick-and-place and processing operation scenarios could be developed for the three robots.

Appendices

Appendix A

Attached Files

Together with this thesis a compressed archive with relevant measurements and source code is delivered. The directories contained in the archive are

- **Maple** This directory contains the Maple code used to calculate the dynamic model for IRB 140 including the matrices $\mathbf{M}$ and $\mathbf{C}$, and the vector $\boldsymbol{g}$ for the identification of parameters of the 6th link of IRB 140 in Chapter 3.
- **MATLAB** This directory is divided into Chapter 3 and 4. Chapter 3 contains the MATLAB code and the measurements used for identification the five unknown parameters for the 6th link of IRB 140. Chapter 4 contains the measurements from the lab experiments with the controller and the code used to plot the measurements.
- **Simulink** This directory contains the Simulink model for the controller which is exported to MATLAB 2010b, to be used to control the 6th joint of IRB 140 at the Robotics Lab.

Bibliography

[1] ABB. *Product specification, Articulated robot IRB140*.

[2] ABB. *Product specification, Articulated robot IRB1600*.

[3] Alexey A. Bobtsov, Anton A. Pyrkin, and S.A. Kolyubin. Adaptive stabilization of a reaction wheel pendulum on moving lego platform. In *Control Applications, (CCA) Intelligent Control, (ISIC), 2009 IEEE*, pages 1218–1223, 2009.

[4] Olav Egeland and Jan Tommy Gravdahl. *Modeling and Simulation for Automatic Control*. Marine Cybernetics, Trondheim, Norway, 2003.

[5] James Ernst, Claudio Zizzo, and Shawn Thimas Collins. Determining fan parameters through pressure monitoring, 2011.

[6] Randi Anette Fikkan. Using abb multimove functionality for cooperative manipulation tasks. Randi Anette Fikkans specialization project in Engineering Cybernetics at the Norwegian University of Science and Technology written during the autumn of 2012.

[7] S.T. Glad and L. Ljung. Model structure identifiability and persistence of excitation. In *Decision and Control, 1990., Proceedings of the 29th IEEE Conference on*, pages 3236–3240 vol.6, 1990.

[8] P.A. Ioannou and J. Sun. *Robust Adaptive Control*. Prentice Hall, Inc, 1996. Out of print 2003.

[9] Lennart Ljung. *System Identification; Theory for the User*. Prentice Hall PTR, second edition, 1999.

[10] M. Vidyasagar Mark W. Spong, Seth Hutchinson. *Robot Modeling and Control*. John Wiley & Sons, Inc., 2006.

[11] Stig Moberg. *Modeling and Control of Flexible Manipulators*. PhD thesis, Linköping University, 2010.

[12] John G. Proakis and Dimitris Manolakis. *Digital Signal Processing.* Pearson Prentice hall, Upper Saddle River, New Jersey 07458, fourth edition, 1996.

[13] T. Söderström and P. Stoica. *System Identification.* Prentice-Hall Int., London, Great Britain, 1989.